44
4-26-96 JS ②

UNIVERSITY OF WISCONSIN

CENTER FOR PLASMA THEORY AND COMPUTATION

REPORT

Computational Modeling of Neoclassical and Resistive MHD Tearing Modes in Tokamaks

T.A. Gianakon

Department of Nuclear Engineering & Engineering Physics
University of Wisconsin-Madison
Madison, Wisconsin 53706-1687

February 1996

UW-CPTC 96-1

MASTER

DISTRIBUTION OF THIS DOCUMENT IS UNLIMITED 85

MADISON, WISCONSIN 53706-1687

DISCLAIMER

Portions of this document may be illegible in electronic image products. Images are produced from the best available original document.

COMPUTATIONAL MODELING OF NEOCLASSICAL AND RESISTIVE MHD TEARING MODES IN TOKAMAKS

by

THOMAS A. GIANAKON

A dissertation submitted in partial fulfillment of the
requirements for the degree of

Doctor of Philosophy
(Nuclear Engineering and Engineering Physics)

at the
UNIVERSITY OF WISCONSIN—MADISON
1996

Abstract

Numerical studies of the linear and nonlinear evolution of magnetic tearing type modes in three-dimensional toroidal geometry are presented. In addition to traditional resistive MHD effects, where the parameter Δ' determines the stability properties, neoclassical effects have been included for the first time in such models. The inclusion of neoclassical physics introduces an additional free-energy source for the nonlinear formation of magnetic islands through the effects of a bootstrap current in Ohm's law. The neoclassical tearing mode is demonstrated to be destabilized in plasmas which are otherwise Δ' stable, albeit once an island width threshold is exceeded.

The simulations are based on a set of neoclassical reduced magnetohydrodynamic (MHD) equations in three-dimensional toroidal geometry derived from the two-fluid equations in the limit of small inverse aspect ratio ϵ and low plasma pressure β with neoclassical closures for the viscous force $\nabla \cdot \vec{\vec{\pi}}$. The poloidal magnetic flux ψ, the toroidal vorticity w^{ζ}, and the plasma pressure p are time advanced using the parallel projection of Ohm's law, the toroidal projection of the curl of the momentum equation, and a pressure evolution equation with anisotropic pressure transport parallel to and across magnetic field lines. The equations are implemented in an initial value code which Fourier decomposes equilibrium and perturbation quantities in the poloidal and toroidal directions, and finite differences them radially based on a equilibrium straight magnetic field line representation. An implicit algorithm is used to advance the linear terms; the nonlinear terms are advanced explicitly.

The simulations are benchmarked linearly and nonlinearly against single and multiple helicity Δ' tearing modes in toroidal geometry in the absence of neoclassical effects. The plasma pressure dynamics and neoclassical tearing growth is shown to be very sensitive to the choice of the ratio of the perpendicular to parallel diffusivity $(\chi_{\perp}/\chi_{\|})$. The study is completed with a demonstration of the threshold for single helicity neoclassical MHD tearing modes, which is described based on parameter scans of plasma pressure β_0, the ratio of perpendicular to parallel pressure diffusivities $\chi_{\perp}/\chi_{\|}$, and the magnitude of an initial seed magnetic perturbation. The threshold is shown to qualitatively agree with theoretical predictions.

Contents

Chapter 1

Introduction

The performance gains of the last several years in tokamak fusion plasmas has generated a resurgence in the observation of low helicity magnetic oscillations [1, 2]. Often, the onset of such oscillations either cause the plasma to disrupt violently [3, 4] or they significantly degrade the plasma confinement [5]. One of the primary candidates for such oscillations, based primarily on the measurement of island rotation/locking by Mirnov coils and the observation of pressure flattening about individual resonant rational surfaces by electron cyclotron emission [5], appear to be instabilities referred to as magnetic tearing modes.

Furth, Killeen, and Rosenbluth provided an early description of the tearing mode in the sheared slab geometry [6], but Wesson [7] succinctly describes the tearing mode in a tokamak as "driven by the radial gradient of the equilibrium current density. The name derives from the tearing and reconnection of magnetic field lines which occur during the instability as a consequence of finite resistivity." The puncture plot of Figure 1.1 illustrates the island structure of a magnetic field by tracing individual field lines as they wrap around the plasma and pass through a poloidal cross-section of a tokamak plasma. An island separatrix exists when distinct field lines converge to a single point and it separates the topologically toroidal nested surfaces outside the island separatrix from the flux tubes which are centered about the island O-point. Tearing and reconnection occur at the island X-point.

In a single fluid resistive magnetohydrodynamic (MHD) model, since the growth of the instability is slow, inertial effects are in general negligible. This implies that the plasma is described by a low pressure version of ideal MHD, so that $\nabla \times (\vec{J} \times \vec{B}) = 0$, or in a large aspect ratio limit that $\vec{B} \cdot \nabla J_{||} = 0$. The linearized form of this equation, when combined with Ampere's law, generates a balance between the stabilizing effect of magnetic field line bending and the

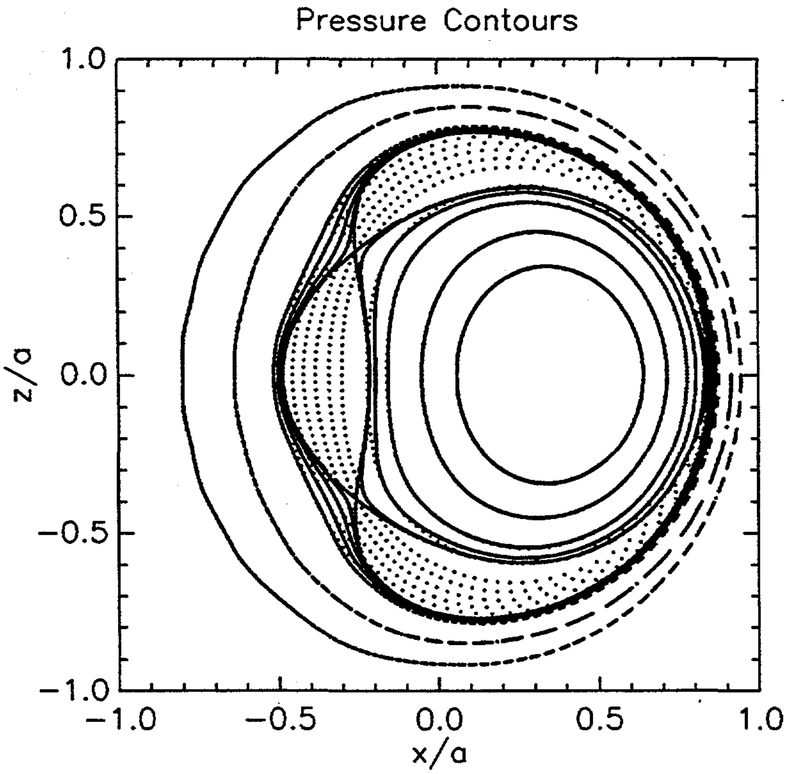

Figure 1.1: Puncture plot and pressure contours of a tearing mode in a tokamak plasma. The solid lines are the puncture plot, and the dashed lines are the pressure contours.

destabilizing influence of the radial equilibrium current gradient. However in a narrow layer of width δ_R about a mode rational surface on which exists a magnetic perturbation of the same helicity as the mode rational surface, the field line term vanishes and ideal MHD is no longer valid. In this narrow boundary layer, resistivity dominates the mode growth and the mode solution is determined by a combination of Ohm's law, Faraday's law, and Ampere's law. The matching of solutions between the resistive inner and ideal outer regions leads to a parameter which determines the stability of the tearing mode. This tearing mode matching parameter is given by

$$\Delta' = \lim_{\epsilon_l \to 0} \frac{1}{\psi_s} \left(\frac{d\psi}{dr} \right)_{r_s - \epsilon_l}^{r_s + \epsilon_l}, \tag{1.1}$$

where ψ is a solution to the ideal equations outside the layer, ϵ_l is a measure of the layer width δ_R, and r_s is the radius of the mode rational surface. The parameter Δ' is a measure of the free energy available for the resistive reconnection of magnetic field lines. In addition to the magnetic island structure, a vortex flow (inertia) is also created which moves plasma in a direction from outside the island separatrix, toward the X-point, then toward the island O-point, and also out across the island separatrix. This flow inertia can also be important for the layer dynamics.

Since the sign of Δ' completely determines the stability of the tearing mode (positive implies instability), only the outer solution need be computed to determine mode stability. An additional complication associated with the linear theory is that the resistive layer width is often on the order of an ion gyroradius, which implies that resistive MHD is no longer strictly valid. Other complications to linear tearing theory are that, in toroidal geometry, the effect of poloidal mode coupling complicates the solution. An analytical extension of this Δ' approach for toroidal geometry known as E-matrix theory has been developed [8, 37], which is based on a perturbative scheme in the aspect ratio and the poloidal β. Also, a numerical extension is in progress via Glasser's DCON code [13].

While linear theory provides a simple understanding of early growth dynamics, the modes observed experimentally are larger than the resistive layer and have grown beyond the linear stage. In the nonlinear phase, it is more appropriate to use a Rutherford [14] analysis of the tearing mode. In the Rutherford growth regime, the island width is given by

$$\frac{dW}{dt} = \frac{4\pi\eta}{c^2}\Delta', \tag{1.2}$$

where η is the plasma resistivity and W is the island width. Henceforth, the time will be normalized to the resistive skin diffusion time $a^2 4\pi/c^2\eta$ and lengths to a plasma minor radius a. Thus, the dimensional coefficient $4\pi\eta/c^2$ will disappear from the equation. In the Rutherford regime, the nonlinear portion of $\vec{B}\cdot\nabla J_{||}$ generates eddy currents which produce a force that opposes the vortex flow and as the mode grows replaces the effect of inertia. This causes the growth rate to slow from exponential to linear in time.

Finally, the Δ' tearing mode saturates because the mode nonlinearly generates currents that are sufficient to flatten the local equilibrium current gradient, $(\Delta'(W) \to 0)$. The island width in this case is governed by [15]

$$\frac{dW}{dt} = \Delta'(0)\left(1 - \frac{W_{sat}}{W}\right), \tag{1.3}$$

where W_{sat} is the saturated magnetic island width.

However, the dynamics of the experimentally observed modes in the advanced tokamak operational regimes (but not necessarily in reverse shear discharges) do not agree with this conventional picture of a Δ' tearing mode. One theoretical explanation for such modes is destabilization from the perturbed bootstrap current. Neoclassical effects arise from the viscous damping of the poloidal electron flow. The portion of the flow produced from the poloidal projection of the diamagnetic current when balanced against electron-ion friction yields a parallel current proportional to the cross-field pressure gradient, the bootstrap current. In the presence of a magnetic island, the pressure flattens within the island separatrix when parallel transport is fast relative to perpendicular transport. The pressure flattening eliminates the diamagnetic and hence the neoclassical bootstrap current within the magnetic island. However, the cross-field pressure gradient remains outside the island separatrix. Since the pressure contours deform due to the island formation, a perturbed bootstrap current develops. For an equilibrium with $dp/dq < 0$, where p is the equilibrium pressure and q is the inverse rotational transform, this perturbation produces a destabilizing effect.

Qu and Callen [16] and also Carrera et al. [17] developed analytic theories for the nonlinear evolution of the island width W, which can be summarized as

$$\frac{dW}{dt} = \alpha \left(\Delta' + \frac{W_c}{W} \right), \tag{1.4}$$

where α is a numerical coefficient of $O(1)$ and W_c is a coefficient which describes the bootstrap current. For this class of modes Δ' is typically stabilizing, though it need not be, and can be well approximated in the limit of large m by $-2m/r_s$, where m is the poloidal mode number and r_s is the normalized radius of the mode rational surface.

However, when the magnetic island is "small," the helical perturbation of the pressure profile about the island may be insufficient to destabilize the island and a threshold for mode destabilization occurs. Fitzpatrick [8] has developed an analytical model for the island dynamics which incorporates many of these features. In this particular model, the magnetic island width, W, is given by

$$I_1 \frac{dW}{dt} = \Delta' + 9.26\epsilon_s^{0.5} \frac{\beta_s'}{s_s} \frac{W}{W^2 + W_d^2}, \tag{1.5}$$

where $I_1 \simeq 0.8227$, $\Delta' \simeq -2m/\rho_s$, $W_d \simeq 1.8W_c$,

$$W_c = 2.83 \left(\frac{\chi_\perp}{\chi_\|} \right)^{0.25} \left(\frac{1}{\epsilon_s s_s n} \right)^{0.5}, \tag{1.6}$$

$$\epsilon_s = \epsilon \rho_s, \tag{1.7}$$

$$s_s = \frac{\rho_s q'}{q}, \tag{1.8}$$

$$\beta_s' = -\beta_0 \left(\frac{q_s}{\epsilon_s}\right)^2 p_s'. \tag{1.9}$$

Here, $\chi_\perp$ and $\chi_\parallel$ are the perpendicular and parallel pressure diffusivities respectively, the mode is resonant at $\rho \equiv r/a = \rho_s \equiv r_s/a$ where $q = m/n$, β_0 is the pressure on axis, and p_s' is the pressure gradient evaluated at the resonant surface.

This model is essentially the same as the Qu and Callen model in the limit $\chi_\parallel/\chi_\perp \to \infty$, i.e., where the pressure completely equilibrates on each flux surface. The dynamics of the island evolution model can be illustrated in the simple phase space diagram of Figure 1.2. At small island width the perpendicular pressure transport dominates over the parallel transport and the pressure profile is unaffected by the island structure, which then produces no perturbed bootstrap current, and no island growth. As the island width is increased, the island eventually perturbs the pressure profile and the perturbed bootstrap current is then able to destabilize the island. An increase in the overall plasma pressure shifts the entire phase space curve upward. This then reduces the threshold for the mode and also increases the saturated island width. Alternatively, an increase in the parallel pressure diffusivity primarily shifts the instability threshold to smaller amplitude, but leaves the saturated state at nearly the same value. The two possible critical points, at which the growth rate is zero, are given by

$$W = \frac{-\alpha_0}{2} \pm \frac{1}{2}\left(\alpha_0^2 - 4W_d^2\right)^{0.5}, \tag{1.10}$$

where

$$\alpha_0 = \frac{9.26\epsilon_s^{0.5}\beta_s'}{\Delta' s_s}. \tag{1.11}$$

The smaller of these fixed points is unstable and the larger is stable.

As illustrated in Figure 1.3, recent work by Chang demonstrates excellent dynamical agreement between the neoclassical MHD model and experimental observations on TFTR [1, 2]. As shown in Figure 1.4, the analytical estimates of the saturated island width also show remarkable agreement with the neoclassical MHD estimates.

The difficulty with the TFTR data is that it is difficult to ascertain the existence of an instability threshold for the mode, because small amplitude oscillations are near the threshold of detectability with the Mirnov coils. However,

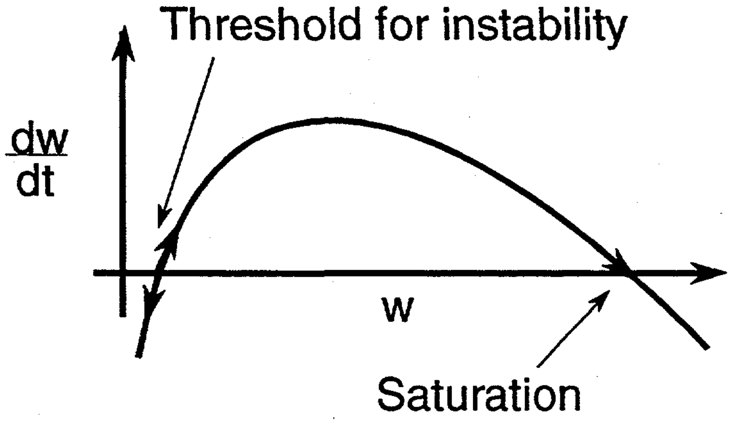

Figure 1.2: Phase diagram of the neoclassical MHD tearing mode.

experimental observations on DIII-D of finite β versus the maximum field error for stability, as illustrated in Figure 1.5, indicate a threshold for destabilization of tearing modes [18]. But, these modes have not as yet been experimentally identified as neoclassical tearing modes.

To explore the dynamics of the neoclassical MHD tearing mode in a realistic toroidal geometry, numerical simulations based on neoclassical reduced MHD equations have been conducted. In Chapter 2, the model equations for neoclassical reduced MHD are derived and their implementation in the FARGO code is presented. In Chapter 3, simulation results based on this neoclassical MHD model are presented, beginning from a single helicity standard Δ' unstable tearing mode in Section 3.1, moving on to multiple helicity modes in Section 3.2, and finally to a single helicity neoclassical MHD tearing mode in Section 3.3. The results are summarized in Chapter 4.

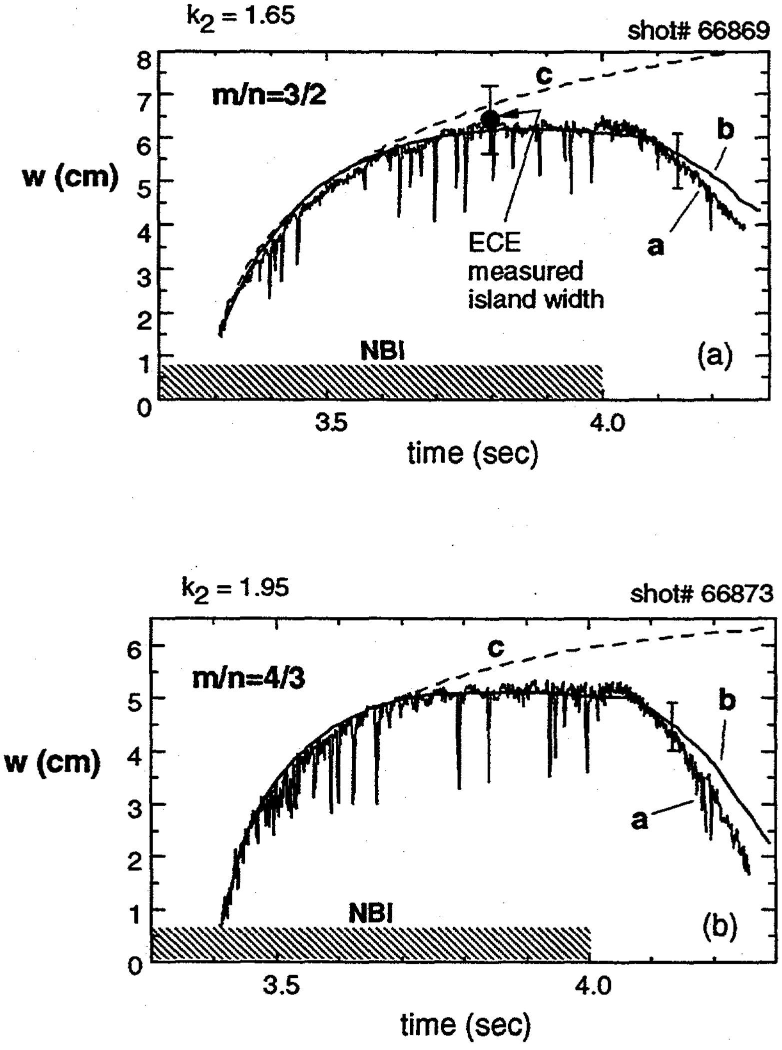

Figure 1.3: Dynamic evolution of the analytical model (b) agrees with experimental observations (a) on TFTR [1,2]. The island width is computed from the signals from the Mirnov coils and is in agreement with the island width deduced from the electron cyclotron emission diagnostic. Neutral beams are on during the hashed region of the time line. A single free parameter (k_2) multiplying the neoclassical MHD term is used to fit the model to the data.

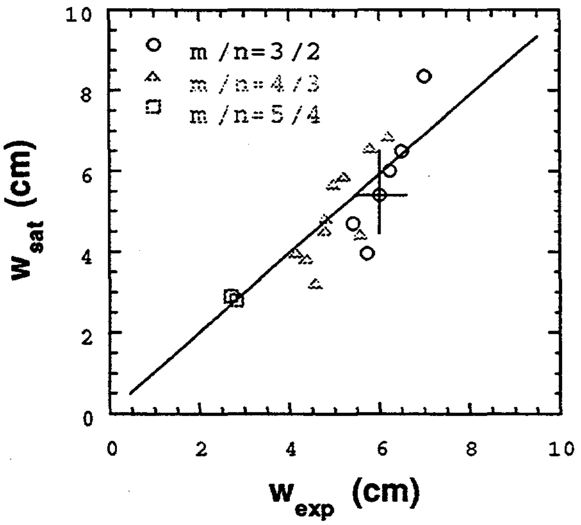

Figure 1.4: Experimental measurements on TFTR of the static magnetic island width agree with neoclassical MHD predictions.

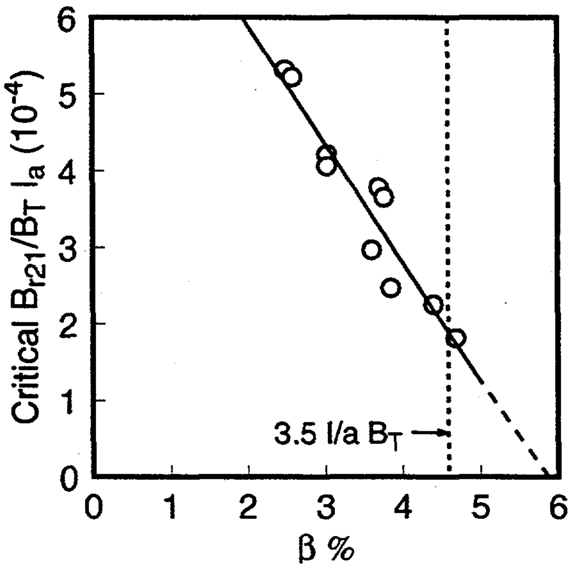

Figure 1.5: Experimental measurements on DIII-D of the critical field width required for the onset of a tearing instability decreases with increasing plasma pressure, i.e., $\beta = 2\mu_0 p/B^2$.

Chapter 2

Model Equations

In this chapter, a set of equations for the numerical simulation of resistive instabilities in a tokamak are developed which include neoclassical viscous stress effects. The starting point is a set of two fluid equations in the limit of zero electron inertia ($m_e \to 0$). An ideal MHD equilibria in an axisymmetric toroidal geometry is next assumed and formulated in terms of a Grad-Shafranov equation. This equilibrium is solved numerically with the fixed boundary equilibrium Grad-Shafranov code RSTEQ [19, 20, 21]. The equilibrium is then used to define a nonorthogonal "straight-field-line" coordinate system, which will be used to formulate the model equations by decomposing the derived evolution equations into equilibrium (subscript 0) and fluctuation components (subscript 1). The full set of two fluid equations are not solved; instead, a set of neoclassical reduced MHD evolution equations for the poloidal flux, the toroidal vorticity and the plasma pressure are derived based principally on an expansion in two small parameters, the inverse aspect ratio ($\epsilon \ll 1$) and the plasma pressure ($\beta \ll 1$), which will be formally defined later. The equations are implemented and solved numerically based on the initial value code FARGO [22]. Throughout the following sections, all operators are fully expanded to reflect their eventual numerical implementation.

2.1 Two fluid equations

The two fluid equations in the limit of zero electron inertia ($m_e \to 0$) are current continuity or quasineutrality

$$\nabla \cdot \vec{J} = 0, \tag{2.1}$$

where $\vec{J}$ is the plasma current; ion continuity or mass conservation

$$\frac{\partial \rho_D}{\partial t} + \nabla \cdot (\vec{v}\rho_D) = 0, \tag{2.2}$$

where ρ_D is the plasma mass density and $\vec{v}$ is the plasma flow velocity; electron momentum balance or Ohm's law

$$\vec{E} + \vec{E}^A + \vec{v} \times \vec{B} = \eta \vec{J} - \frac{m_i}{\rho_D e} \nabla \cdot \vec{\vec{\pi}}_e, \tag{2.3}$$

where $\vec{E}$ is the internal electric field, $\vec{E}^A$ is the externally applied inductive electric field, $\vec{B}$ is the magnetic field, η is the plasma resistivity due to collisions between electrons and ions, m_i is the ion mass, e is the electron charge, and $\vec{\vec{\pi}}_e$ is the electron stress tensor; ion momentum balance

$$\rho_D \frac{\partial \vec{v}}{\partial t} + \rho_D \vec{v} \cdot \nabla \vec{v} = \vec{J} \times \vec{B} - \nabla p - \nabla \cdot \vec{\vec{\pi}}_i - \nabla \cdot \vec{\vec{\pi}}_e, \tag{2.4}$$

where $\vec{\vec{\pi}}_e$ is the electron stress-tensor and $\vec{\vec{\pi}}_i$ is the ion stress tensor; and lastly the pressure or heat balance equation

$$\frac{\partial p}{\partial t} + \vec{v} \cdot \nabla p = Q - \nabla \cdot \vec{q}, \tag{2.5}$$

where the electron and ion pressures have been combined into a total pressure p, Q is the plasma heating source term, and $\vec{q}$ is the heat flux which is given by

$$\vec{q} = -\chi_\perp \nabla p - (\chi_\parallel - \chi_\perp) \vec{B} \frac{\vec{B} \cdot \nabla p}{B^2}, \tag{2.6}$$

where $\chi_\perp$ is the perpendicular pressure diffusivity and $\chi_\parallel$ is the parallel pressure diffusivity. In addition to the fluid equations, the Maxwell equations are required, which are: no magnetic monopole's,

$$\nabla \cdot \vec{B} = 0, \tag{2.7}$$

Ampere's law,

$$\vec{\nabla} \times \vec{B} = \frac{4\pi}{c} \vec{J}, \tag{2.8}$$

and Faraday's law,

$$-\frac{\partial \vec{B}}{\partial t} = \vec{\nabla} \times \vec{E}. \tag{2.9}$$

The fluid equations above are incomplete because of the introduction of the stress tensor term—a term which must be evaluated either via a kinetic or higher-order fluid moment approach. This model will use a stress tensor based on a neoclassical closure [26, 27, 28] appropriate for the limit of long collisional mean free path length (or low collision frequency), which accounts for the viscosity between trapped and untrapped particles. The stress tensor, $\overleftrightarrow{\pi}$, is represented in a Chew—Goldberger—Low form as

$$\overleftrightarrow{\pi}_\alpha \simeq \overleftrightarrow{\pi}_{\|\alpha} = \left(\frac{\vec{B}\vec{B}}{B^2} - \frac{\overleftrightarrow{I}}{3}\right)(p_\| - p_\perp)_\alpha, \tag{2.10}$$

where

$$(p_\| - p_\perp)_\alpha = -2m_\alpha n_\alpha \mu_\alpha \frac{\langle B^2\rangle}{\left\langle\left[\frac{\vec{B}\cdot\nabla B^2}{B^2}\right]^2\right\rangle}\frac{\vec{v}_\alpha\cdot\nabla B^2}{B^2}; \tag{2.11}$$

the subscript alpha indicates electron's or ions. The $\langle\Phi\rangle$ is a flux surface average of the quantity Φ. The viscous damping frequencies are approximated by [26, 28]

$$\mu_e \simeq \frac{2.3\epsilon_r^{1/2}\nu_e}{(1+1.07\nu_{*e}^{1/2}+1.02\nu_{*e})(1+1.07\nu_{*e}\epsilon_r^{3/2})}, \tag{2.12}$$

$$\mu_i \simeq \frac{0.66\epsilon_r^{1/2}\nu_i}{(1+1.03\nu_{*i}^{1/2}+0.31\nu_{*i})(1+0.66\nu_{*i}\epsilon_r^{3/2})}, \tag{2.13}$$

where

$$\nu_{*\alpha} = \nu_\alpha \epsilon_r^{-3/2} R_0 q V_{T_\alpha}^{-1}, \tag{2.14}$$

in which ν_α is the collision frequency of plasma species α and V_{T_α} is the thermal velocity of species α. Here, $\epsilon_r \equiv \rho/R$ is the ratio of the local plasma minor radius to the plasma major radius. The species velocities which appear are given by

$$\vec{v}_e = \vec{v} - \frac{m_i}{e\rho_D}\vec{J}, \tag{2.15}$$

and in the case of ions

$$\vec{v}_i = \vec{v}. \tag{2.16}$$

In both Ohm's law and the momentum balance the relevant expression for the viscous force will be

$$\nabla\cdot\overleftrightarrow{\pi} = \vec{B}\vec{B}\cdot\nabla\left(\frac{f}{B^2}\right) + \frac{f}{B^2}\nabla\left(\frac{B^2}{2}\right) - \frac{f}{B^2}\vec{B}\times\nabla\times\vec{B} - \frac{1}{3}\nabla f, \tag{2.17}$$

where $f = p_\| - p_\perp$.

2.2 Equilibrium

The equilibrium is assumed to be describable by an axisymmetric, toroidal, ideal MHD model. The equilibrium forms the geometric foundation on which the initial value equations are time advanced and is designed to minimize the numerical errors associated with the parallel operator $\vec{B} \cdot \nabla$ that appears in the evolution equations. The most convenient geometry for this operator will be a straight magnetic field line representation, which will have the advantage of simplifying this operator to algebra when fluctuation quantities are Fourier decomposed. However, the straight-field-line representation is a nonorthogonal coordinate system; thus covariant and contravariant basis vectors, with associated metric elements, will have to be introduced to define vector operations. In Figure 2.1, the configuration space geometry is presented.

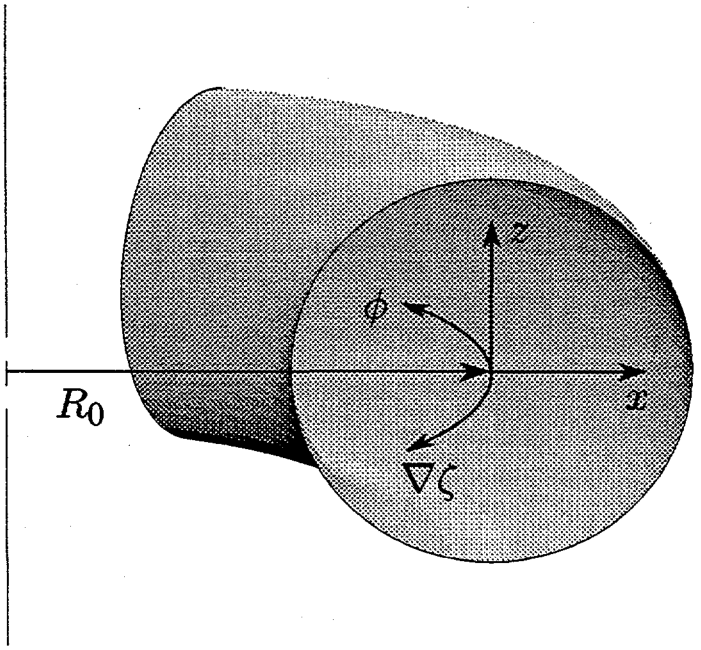

Figure 2.1: An axisymmetric toroidal geometry is assumed with an outer conducting wall as a boundary condition. The Shafranov-shifted magnetic axis is at a radius R_0. The x and z are rectangular coordinates in the poloidal cross-section.

The ideal MHD equilibrium is described by three equations, Eq. 2.7, Ampere's law, and the ideal MHD equilibrium force balance

$$\frac{1}{c}\vec{J} \times \vec{B} = \nabla p. \tag{2.18}$$

Equation 2.7 indicates the magnetic field may be expressed in terms of two magnetic potentials ψ and χ as

$$\vec{B} = \nabla\chi \times \nabla\theta + \nabla\zeta \times \nabla\psi. \tag{2.19}$$

The angle $\zeta = -\phi$ is the toroidal angle, where ϕ is the standard cylindrical geometry angle. (The minus sign enters for historical reasons based on the left handed coordinate system originally used in the FARGO formulation [22].) The angle θ is a poloidal angle and is arbitrary for purposes of the equilibrium solver, until the conversion is made from the solver's geometry to the straight-field-line geometry. The third coordinate will be a flux coordinate ρ which will have the property that $\vec{B} \cdot \nabla\rho = 0$; that is, the magnetic field lines lie in surfaces of constant ρ. The transformation between this coordinate system (ρ, θ, ζ) and the configuration space (x, z, ϕ) will be dealt with later in this section.

In an axisymmetric torus, Eq. 2.19 reduces to

$$\vec{B} = \frac{\partial\chi}{\partial\rho}\nabla\rho \times \nabla\theta + \frac{\partial\psi}{\partial\rho}\nabla\rho \times \nabla\zeta, \tag{2.20}$$

where $\psi = \psi(\rho)$. (Often $\rho \equiv \psi$, but not here.) Also from the force balance, since $\vec{B} \cdot \nabla p = 0$, the pressure is a flux function $p = p(\rho)$. In a straight-field-line representation, the field line path depends by definition only on the flux surface label, where the equation of the field line is given by the components of $d\vec{l} \times \vec{B} = 0$ which here yield

$$\frac{d\theta}{\vec{B} \cdot \nabla\theta} = \frac{d\zeta}{\vec{B} \cdot \nabla\zeta}. \tag{2.21}$$

Subsequently, the inverse rotational transform, defined as

$$q = \frac{\vec{B} \cdot \nabla\zeta}{\vec{B} \cdot \nabla\theta} = \frac{B^{\zeta}}{B^{\theta}}, \tag{2.22}$$

must be a flux function. Finally, the flux coordinate ρ will eventually be normalized to have a value of 0 at the magnetic axis and a value of 1 at the plasma edge.

In axisymmetric systems the equilibrium magnetic field is expressed not in terms of these potentials but equivalently as

$$\vec{B} = I\nabla\zeta + \nabla\zeta \times \nabla\psi, \tag{2.23}$$

where I can be shown to be a flux function from axisymmetry. This form is introduced because it is the basis of the equilibrium solver. The relationship between the two systems is derived by taking the toroidal projection of Eq. 2.23 and Eq. 2.19. The result is

$$B^{\zeta} = \frac{I}{R^2} = \frac{d\chi}{d\rho}\nabla\rho \cdot \nabla\theta \times \nabla\zeta, \tag{2.24}$$

where $\chi = \chi(\rho)$ is a flux function.

When, the radial projection of the ideal MHD equilibrium force balance is combined with Ampere's law, the result is the Grad-Shafranov equation [23], which is expressed as

$$R^2\nabla \cdot \left(\frac{1}{R^2}\nabla\psi\right) = -\frac{\beta_0}{2\epsilon^2}R^2\frac{dp}{d\psi} - \frac{1}{\epsilon^2}I\frac{dI}{d\psi}, \tag{2.25}$$

where the following normalizations have made [20]. First, length scales have been normalized by the plasma minor radius $a = \epsilon R_0$, where R_0 is the Shafranov-shifted major axis and ϵ is the inverse aspect ratio defined as

$$\epsilon^2 = \frac{1}{2\pi}\int_V d^3V \frac{1}{R^2}, \tag{2.26}$$

but with the exception that the cylindrical coordinate R has been normalized by R_0. The magnetic field has been normalized by the value (in units of Gauss)

$$B^* = I_{wall}R_0^{-1}, \tag{2.27}$$

where $I/I_{wall} = 1$ at the plasma edge. The flux ψ has been normalized by

$$\psi^* = -\epsilon^2 R_0 I_{wall}. \tag{2.28}$$

The pressure is normalized to p_0, the pressure on axis, which leads to a definition of β_0 of

$$\beta_0 = \frac{8\pi p_0 R_0^2}{I_{wall}^2}. \tag{2.29}$$

The equilibrium solver generates the solution $\psi(R, Z)$ based on the two free input flux functions $q(\psi)$ and $p(\psi)$.

2.2.1 Metric elements

As previously mentioned, a transformation to define the vector operators [23] must now be made between between the solvers (R, ϕ, Z) coordinate system and the straight-field-line representation (ρ, θ, ζ) [20]. First, a slight transformation will be made by converting R to $X = R - 1$ as is done in the numerical implementation. The coordinates (x,z,ϕ) may be formally expressed in terms of the flux coordinates (ρ,θ,ζ) in terms of the general curvilinear coordinate system transformations:

$$\begin{aligned} x &= f(\rho, \theta), \\ z &= g(\rho, \theta), \\ \phi &= -\zeta. \end{aligned} \tag{2.30}$$

The procedure is straightforward to generate the contravariant flux coordinate directions in terms of the original toroidal basis. Namely, the gradients of the above equations are taken and the resultant matrix inverted to generate the nonorthogonal basis:

$$\begin{aligned} \nabla\rho &= -\frac{R}{\mathcal{J}}\left\{\frac{\partial g}{\partial\theta}\nabla x - \frac{\partial f}{\partial\theta}\nabla z\right\}, \\ \nabla\theta &= -\frac{R}{\mathcal{J}}\left\{-\frac{\partial g}{\partial\rho}\nabla x + \frac{\partial f}{\partial\rho}\nabla z\right\}, \\ \nabla\zeta &= -\frac{\hat{\phi}}{R}, \end{aligned} \tag{2.31}$$

where $\mathcal{J}$ is the Jacobian

$$\mathcal{J} = -R\left\{\frac{\partial f}{\partial\rho}\frac{\partial g}{\partial\theta} - \frac{\partial f}{\partial\theta}\frac{\partial g}{\partial\rho}\right\}. \tag{2.32}$$

Note that

$$\mathcal{J}^{-1} = \nabla\rho\cdot(\nabla\theta\times\nabla\zeta). \tag{2.33}$$

As of yet, the ρ and θ coordinate system is still arbitrary until the connection is made with the straight-field-line representation requirement of Eq. (2.22). A convenient choice for $\mathcal{J}$, which leads to a representation that can readily be reduced to cylindrical coordinates, is

$$\mathcal{J}^{-1} = \nabla\rho\cdot(\nabla\theta\times\nabla\zeta) = -\frac{1}{\rho R^2}. \tag{2.34}$$

The metric elements are represented as [20]

$$\begin{aligned} g^{\rho\rho} &= \nabla\rho\cdot\nabla\rho = \frac{1}{\rho^2R^2}\left\{\left(\frac{\partial g}{\partial\theta}\right)^2+\left(\frac{\partial f}{\partial\theta}\right)^2\right\}, && (2.35)\\ g^{\rho\theta} &= \nabla\rho\cdot\nabla\theta = \frac{-1}{\rho^2R^2}\left\{\frac{\partial g}{\partial\theta}\frac{\partial g}{\partial\rho}+\frac{\partial f}{\partial\theta}\frac{\partial f}{\partial\rho}\right\}, && (2.36)\\ g^{\theta\theta} &= \nabla\theta\cdot\nabla\theta = \frac{1}{\rho^2R^2}\left\{\left(\frac{\partial g}{\partial\rho}\right)^2+\left(\frac{\partial f}{\partial\rho}\right)^2\right\}, && (2.37)\\ g^{\zeta\zeta} &= \nabla\zeta\cdot\nabla\zeta = \frac{1}{R^2}. && (2.38) \end{aligned}$$

In order to eliminate singular behavior near the magnetic axis, which becomes a problem when spline fits of the metric elements are generated, a series of hatted metric elements are defined as

$$\begin{aligned} g^{\rho\rho} &= R_0^{-1}\hat{g}^{\rho\rho}, && (2.39)\\ g^{\rho\theta} &= R_0^{-1}\frac{\hat{g}^{\rho\theta}}{\rho}, && (2.40)\\ g^{\theta\theta} &= R_0^{-1}\frac{\hat{g}^{\theta\theta}}{\rho^2}, && (2.41) \end{aligned}$$

where f and g have been normalized to ϵR_0 and ρ to $\epsilon R_0^{1/2}$. The hatted terms represent the dimensionless metric elements that are available as output from the equilibrium code. Additionally, the following metric elements, which are derived from the above relations, are required:

$$\begin{aligned} g_{\rho\rho} &= \rho^2R^2g^{\theta\theta}, && (2.42)\\ g_{\rho\theta} &= -\rho^2R^2g^{\rho\theta}, && (2.43)\\ g_{\theta\theta} &= \rho^2R^2g^{\rho\rho}, && (2.44)\\ g_{\zeta\zeta} &= R_0^2R^2. && (2.45) \end{aligned}$$

2.2.2 Equilibrium magnetic field

From Eq. (2.23), the contravariant components of the equilibrium magnetic field may be expressed as

$$\begin{aligned} B^\rho \equiv \vec{B}\cdot\nabla\rho &= 0,\\ B^\theta \equiv \vec{B}\cdot\nabla\theta &= \frac{I_{wall}}{R_0^2}\frac{I}{qR^2}, && (2.46)\\ B^\zeta \equiv \vec{B}\cdot\nabla\zeta &= \frac{I_{wall}}{R_0^2}\frac{I}{R^2}, \end{aligned}$$

where

$$\frac{d\psi}{d\rho} = -\frac{\rho I}{q}, \tag{2.47}$$

and $I(\rho = 1) = 1$ at the plasma edge. The covariant components of the magnetic field are then

$$\begin{aligned} B_\rho \equiv g_{\rho\rho}B^\rho + g_{\rho\theta}B^\theta &= -I_{wall}\epsilon R_0^{-1/2}\frac{I\rho}{q}\hat{g}^{\rho\theta}, \\ B_\theta \equiv g_{\rho\theta}B^\rho + g_{\theta\theta}B^\theta &= I_{wall}\epsilon^2\frac{I\rho^2}{q}\hat{g}^{\rho\rho}, \\ B_\zeta \equiv g_{\zeta\zeta}B^\zeta &= I_{wall}I. \end{aligned} \tag{2.48}$$

2.2.3 Equilibrium currents

The equilibrium currents can now be deduced from Ampere's law,

$$\frac{4\pi}{c}\vec{J} = \nabla \times \vec{B}, \tag{2.49}$$

and represented by the contravariant components of the current as

$$\begin{aligned} \frac{4\pi}{c}J^\rho &= 0, \\ \frac{4\pi}{c}J^\theta &= \frac{I_{wall}}{R_0^3\epsilon^2}\frac{1}{\rho R^2}\frac{dI}{d\rho}, \\ \frac{4\pi}{c}J^\zeta &= \frac{-I_{wall}}{R_0^3}\left\{\frac{1}{\rho R^2}\frac{\partial}{\partial\rho}\left(\frac{I\rho^2}{q}\hat{g}^{\rho\rho}\right) + \frac{1}{\rho R^2}\frac{I\rho}{q}\frac{\partial}{\partial\theta}\hat{g}^{\rho\theta}\right\}, \end{aligned} \tag{2.50}$$

or by the covariant components of the current as

$$\begin{aligned} \frac{4\pi}{c}J_\rho &= \frac{-I_{wall}}{\epsilon R_0^{3/2}}\hat{g}^{\rho\theta}\frac{dI}{d\rho}, \\ \frac{4\pi}{c}J_\theta &= \frac{1}{R_0}\rho\hat{g}^{\rho\rho}\frac{dI}{d\rho}, \\ \frac{4\pi}{c}J_\zeta &= \frac{4\pi}{c}R_0^2R^2J^\zeta. \end{aligned} \tag{2.51}$$

2.3 Neoclassical Reduced MHD Equations

The model presented here is a close derivative of the reduced-MHD models of both Strauss [24] and also Hazeltine and Meiss [25] , and as such reduces the

14 unknowns plus stress-tensors in the full MHD equations to three unknowns determined by a parallel Ohm's law, a vorticity evolution and a pressure evolution equation. While these models neglect the viscous stress tensor, this model includes such effects based on neoclassical closure arguments [26]. At this point it is convenient to define two timescales which will be relevant for the initial value equations. The first is the resistive time τ_R which is defined as

$$\tau_R = \frac{\epsilon^2 R_0^2}{\eta} \frac{4\pi}{c^2}, \tag{2.52}$$

and will be used to normalize all times. The second is the Alfven time τ_A which is defined as

$$\tau_A^{-2} = \frac{I_{wall}^2}{\rho_D R_0^4 4\pi}. \tag{2.53}$$

The ratio of these two time scales,

$$S = \frac{\tau_R}{\tau_A}, \tag{2.54}$$

is defined as the Lundquist or magnetic Reynold's number and for a hot tokamak plasma has the property $S \gg 1$; e.g., in TFTR $S \sim 10^8$.

2.3.1 Perturbed magnetic field

From Eq. (2.7), the perturbed magnetic field may be expressed in terms of a vector potential,

$$\vec{B}_1 = \nabla \times \vec{A}_1, \tag{2.55}$$

where

$$\vec{A}_1 = \epsilon^2 I_{wall} R_0 \left(-\psi_1 \nabla\zeta + \epsilon \chi_1 \nabla\theta \right), \tag{2.56}$$

in which $A_1^\rho = 0$ is the gauge condition. The ψ_1 is normalized by $\epsilon^2 I_{wall} R_0^2$ and is assumed to be $O(1)$, and χ_1 is normalized by $\epsilon^3 I_{wall} R_0^2$ and is also assumed to be $O(1)$. Consequently, the perturbed contravariant components of the magnetic field are

$$\begin{aligned} B_1^\rho &= \frac{\epsilon I_{wall}}{R_0^{3/2}} \frac{1}{\rho R^2} \frac{\partial \psi_1}{\partial \theta} + \epsilon^2 \frac{1}{\rho R^2} \frac{\partial \chi_1}{\partial \zeta}, \\ B_1^\theta &= -\frac{I_{wall}}{R_0^2} \frac{1}{\rho R^2} \frac{\partial \psi_1}{\partial \rho}, \\ B_1^\zeta &= -\epsilon \frac{I_{wall}}{R_0^2} \frac{1}{\rho R^2} \frac{\partial \chi_1}{\partial \rho}. \end{aligned} \tag{2.57}$$

The covariant components of the magnetic field are then

$$\begin{aligned}
B_{\rho 1} &= \frac{\epsilon I_{wall}}{R_0^{1/2}}\left\{-\frac{\hat{g}^{\theta\theta}}{\rho}\frac{\partial\psi_1}{\partial\theta} - \hat{g}^{\theta\theta}\frac{\partial\psi_1}{\partial\rho} + \epsilon\frac{\hat{g}^{\theta\theta}}{\rho}\frac{\partial\chi}{\partial\zeta}\right\}, \\
B_{\theta 1} &= I_{wall}\epsilon^2\left\{\rho\hat{g}^{\rho\theta}\frac{1}{\rho}\frac{\partial\psi_1}{\partial\theta} + \rho\hat{g}^{\rho\rho}\frac{\partial\psi_1}{\partial\rho} + \epsilon\hat{g}^{\rho\theta}\frac{\partial\chi}{\partial\zeta}\right\}, \qquad (2.58) \\
B_{\zeta 1} &= -\epsilon I_{wall}\frac{1}{\rho}\frac{\partial\chi}{\partial\rho}.
\end{aligned}$$

Subsequently, the following orderings will be made

$$\vec{B}_1 \cdot \vec{B}_0 = \frac{\epsilon I_{wall}^2}{R_0^2}\left\{-\frac{I}{\rho R^2}\frac{\partial\chi}{\partial\rho}\right\} + O(\epsilon^2), \qquad (2.59)$$

and

$$B_1^2 \sim O(\epsilon^2), \qquad (2.60)$$

in order to identify the order of various nonlinear terms which will be dropped when the reduced MHD equations are derived.

2.3.2 Perturbed currents

From Eq. (2.8), which is Ampere's law, the contravariant components of the fluctuating current can now be expressed as

$$\begin{aligned}
\frac{J_1^{\rho}4\pi}{c} &= \frac{I_{wall}}{R_0^{5/2}}\left\{\frac{1}{\rho R^2}\frac{\partial}{\partial\theta}\left(\frac{1}{\rho}\frac{\partial\chi}{\partial\rho}\right)\right\} + \\
&\quad \epsilon\frac{I_{wall}}{R_0^{5/2}}\left\{\frac{\hat{g}^{\rho\theta}}{R^2}\frac{1}{\rho}\frac{\partial^2\psi_1}{\partial\theta\partial\zeta} + \frac{\hat{g}^{\rho\rho}}{R^2}\frac{\partial^2\psi_1}{\partial\rho\partial\zeta}\right\} + \epsilon^2\frac{I_{wall}}{R_0^{5/2}}\left\{\frac{1}{\rho R^2}\hat{g}^{\rho\theta}\frac{\partial^2\chi}{\partial\zeta^2}\right\}, \\
\frac{J_1^{\theta}4\pi}{c} &= \frac{1}{\epsilon}\frac{I_{wall}}{R_0^3}\left\{\frac{-1}{\rho R^2}\frac{\partial}{\partial\rho}\left(\frac{1}{\rho}\frac{\partial\chi}{\partial\rho}\right)\right\} + \\
&\quad \frac{I_{wall}}{R_0^3}\left\{\frac{\hat{g}^{\theta\theta}}{\rho R^2}\frac{1}{\rho}\frac{\partial^2\psi_1}{\partial\theta\partial\zeta} + \frac{\hat{g}^{\rho\theta}}{\rho R^2}\frac{\partial^2\psi_1}{\partial\rho\partial\zeta}\right\} + \epsilon\frac{I_{wall}}{R_0^3}\left\{\frac{-1}{\rho R^2}\frac{\hat{g}^{\theta\theta}}{\rho}\frac{\partial^2\chi}{\partial\zeta^2}\right\}, \qquad (2.61) \\
\frac{J_1^{\zeta}4\pi}{c} &= \frac{I_{wall}}{R_0^3}\left\{\frac{\partial^2\psi_1}{\partial^2\rho}\left[\frac{\hat{g}^{\rho\rho}}{R^2}\right] + \frac{\partial\psi_1}{\partial\rho}\left[\frac{1}{\rho R^2}\frac{\partial}{\partial\theta}\hat{g}^{\rho\theta} + \frac{1}{\rho R^2}\frac{\partial}{\partial\rho}\rho\hat{g}^{\rho\rho}\right]\right. \\
&\quad + \frac{\partial^2\psi_1}{\partial\rho\partial\theta}\left[\frac{2\hat{g}^{\rho\theta}}{R^2}\right] + \frac{1}{\rho}\frac{\partial\psi_1}{\partial\theta}\left[\frac{1}{\rho R^2}\frac{\partial}{\partial\theta}\hat{g}^{\theta\theta} + \frac{1}{\rho R^2}\frac{\partial}{\partial\rho}\hat{g}^{\rho\theta}\right] \\
&\quad \left. + \frac{1}{\rho^2}\frac{\partial^2\psi_1}{\partial\theta^2}\left[\frac{\hat{g}^{\theta\theta}}{R^2}\right]\right\} + \epsilon\frac{I_{wall}}{R_0^3}\left\{\frac{-1}{\rho R^2}\frac{\partial}{\partial\rho}\hat{g}^{\rho\theta}\frac{\partial\chi}{\partial\zeta} + \frac{1}{\rho R^2}\frac{\partial}{\partial\theta}\frac{\hat{g}^{\theta\theta}}{\rho}\frac{\partial\chi}{\partial\zeta}\right\}.
\end{aligned}$$

The covariant components of the fluctuating current are then

$$\begin{aligned}
J_{1\rho} &= \frac{I_{wall}}{R_0^{3/2}} \left\{ \frac{\hat{g}^{\theta\theta}}{\rho} \frac{\partial}{\partial\theta} \left(\frac{1}{\rho} \frac{\partial\chi}{\partial\rho} \right) + \hat{g}^{\rho\theta} \frac{\partial}{\partial\rho} \left(\frac{1}{\rho} \frac{\partial\chi}{\partial\rho} \right) - \epsilon \frac{1}{R^2} \frac{\partial^2\psi}{\partial\rho\partial\zeta} \right\}, \\
J_{1\theta} &= -\epsilon \frac{I_{wall}}{R_0} \left\{ \hat{g}^{\rho\theta} \frac{\partial}{\partial\theta} \left(\frac{1}{\rho} \frac{\partial\chi}{\partial\rho} \right) + \epsilon\rho\hat{g}^{\rho\rho} \frac{\partial}{\partial\rho} \left(\frac{1}{\rho} \frac{\partial\chi}{\partial\rho} \right) \right\} \\
&\quad - \epsilon^2 \frac{I_{wall}}{R_0} \left\{ \frac{1}{R^2} \frac{\partial^2\psi}{\partial\theta\partial\zeta} \right\} + O(\epsilon^3), \qquad (2.62) \\
J_{1\zeta} &= R_0^2 R^2 J^\zeta.
\end{aligned}$$

Subsequently, the following orderings can be identified

$$J_1^2 \sim O(1), \tag{2.63}$$

and also

$$\vec{J}_1 \cdot \vec{J}_0 \sim O\left(\frac{1}{\epsilon} \frac{dI}{d\rho} \right) + O(1). \tag{2.64}$$

For the q-profiles considered here $dI/d\rho \sim \epsilon$ or smaller, which is roughly consistent with $\beta \sim O(\epsilon)$.

2.3.3 Perturbed velocity

In expanding the velocity, several levels of approximation are introduced. First, the equilibrium flow is assumed to be zero. Second, the plasma is assumed to be incompressible. This can either be attributed to the assumption of constant density or can be can be deduced from an assumption that the compressibility $\nabla \cdot \vec{v}$ equilibrates on the fastest time scale or that sound waves equilibrate density fluctuations on the fastest time scale. In analogy to the magnetic field, the velocity is represented by a stream function, in the form

$$\vec{v_1} = \nabla \times \vec{\Omega}_1, \tag{2.65}$$

where

$$\vec{\Omega}_1 = -\phi_1 \nabla\zeta + \Lambda_1 \nabla\theta, \tag{2.66}$$

and the gauge condition $\Omega_1^\rho = 0$ has been chosen. The evolution of Λ_1 will be neglected, which is consistent to lowest order in ϵ with $\vec{v}$ being an $\vec{E} \times \vec{B}$ flow from Ohm's law. Consequently, the perturbed contravariant components of the velocity are

$$\begin{aligned} v_1^\rho &= \frac{\phi^*}{\epsilon R_0^{5/2}} \frac{1}{\rho R^2} \frac{\partial \phi_1}{\partial \theta}, \\ v_1^\theta &= -\frac{\phi^*}{\epsilon^2 R_0^3} \frac{1}{\rho R^2} \frac{\partial \phi_1}{\partial \rho}, \\ v_1^\zeta &= 0, \end{aligned} \tag{2.67}$$

where ϕ has been normalized by ϕ^*, which is

$$\phi^* = \frac{\epsilon^2 R_0^3}{\tau_R}. \tag{2.68}$$

The covariant components of the velocity are then

$$\begin{aligned} v_{\rho 1} &= \frac{\phi^*}{\epsilon R_0^{3/2}} \left\{ \frac{\hat{g}^{\theta\theta}}{\rho} \frac{\partial \phi_1}{\partial \theta} + \hat{g}^{\rho\theta} \frac{\partial \phi_1}{\partial \rho} \right\}, \\ v_{\theta 1} &= -\frac{\phi^*}{R_0} \left\{ \rho \hat{g}^{\rho\theta} \frac{1}{\rho} \frac{\partial \phi_1}{\partial \theta} + \rho \hat{g}^{\rho\rho} \frac{\partial \phi_1}{\partial \rho} \right\}, \\ v_{\zeta 1} &= 0. \end{aligned} \tag{2.69}$$

2.3.4 Vorticity

In analogy with the relationship between the current and the magnetic field, the vorticity will be computed. The vorticity is defined as

$$\vec{w} = \nabla \times \vec{v}. \tag{2.70}$$

Only the toroidal projection of the vorticity will appear in the evolution equations derived in later sections. The toroidal projection of the vorticity is given by

$$\begin{aligned} w_1^\zeta = \frac{\phi_*}{\epsilon^2 R_0^4} \Bigg\{ & \frac{\partial^2 \phi_1}{\partial^2 \rho} \left[\frac{\hat{g}^{\rho\rho}}{R^2} \right] + \frac{\partial \phi_1}{\partial \rho} \left[\frac{1}{\rho R^2} \frac{\partial}{\partial \theta} \hat{g}^{\rho\theta} + \frac{1}{\rho R^2} \frac{\partial}{\partial \rho} \rho \hat{g}^{\rho\rho} \right] \\ & + \frac{\partial^2 \phi_1}{\partial \rho \partial \theta} \left[\frac{2 \hat{g}^{\rho\theta}}{R^2} \right] + \frac{1}{\rho^2} \frac{\partial^2 \phi_1}{\partial^2 \theta} \left[\frac{\hat{g}^{\theta\theta}}{R^2} \right] \\ & + \frac{1}{\rho} \frac{\partial \phi_1}{\partial \theta} \left[\frac{1}{\rho R^2} \frac{\partial}{\partial \theta} \hat{g}^{\theta\theta} + \frac{1}{\rho R^2} \frac{\partial}{\partial \rho} \hat{g}^{\rho\theta} \right] \Bigg\} \end{aligned} \tag{2.71}$$

which is the same operator, except for normalizations, as that which appears in the toroidal current definition, Eq. (2.62).

2.3.5 Divergence of the momentum equation

Since the plasma density is constant and $\nabla \cdot \vec{v} = 0$, the divergence of the momentum equation will be used to relate the magnetic potential χ to the pressure p. The divergence of the momentum equation is

$$\nabla^2 \left(p + \frac{B^2}{8\pi} \right) = \frac{4\pi}{c^2} J^2 - \rho_D w^2 - \nabla \cdot \nabla \cdot \vec{\vec{\pi}}_i - \nabla \cdot \nabla \cdot \vec{\vec{\pi}}_e. \qquad (2.72)$$

First, the equilibrium quantities are balanced and dropped from the equation, which in dimensionless form yields

$$\begin{aligned} &\left(\epsilon^{-2} \nabla_{\wedge}^2 + \frac{1}{R^2} \frac{\partial^2}{\partial \zeta^2} \right) \left(\beta p_1 + \epsilon \vec{B}_1 \cdot \vec{B}_0 + \epsilon^2 B_1^2 \right) \\ = \; & J_1^2 + \vec{J}_1 \cdot \vec{J}_0 - \frac{1}{S^2} \left(w^2 - \nabla \cdot \nabla \cdot \vec{\vec{\pi}}_i - \nabla \cdot \nabla \cdot \vec{\vec{\pi}}_e \right). \qquad (2.73) \end{aligned}$$

[The decomposition of ∇^2 into an $\epsilon^{-2}\nabla_{\wedge}^2 + (1/R^2)(\partial^2/\partial\zeta^2)$ operator will be dealt with later in the pressure evolution section where the operator appears in the context of the heat flux.] For $S \gg 1$, $\beta \sim \epsilon$, and to lowest order in ϵ, Eq. (2.73) reduces to

$$\nabla_{\wedge}^2 \left(p_1 - \frac{I}{\rho R^2} \frac{\partial \chi}{\partial \rho} \right) \simeq O(\epsilon), \qquad (2.74)$$

which can be satisfied with

$$p_1 = \frac{I}{\rho R^2} \frac{\partial \chi}{\partial \rho}. \qquad (2.75)$$

Equation 2.75 eliminates magnetosonic waves from the evolution equations and is to lowest order a statement of perturbed radial force balance: $p_1 + \vec{B}_1 \cdot \vec{B}_0 = 0$.

2.3.6 Parallel Ohm's law

In equilibrium, Eq. (2.3), which is Ohm's law, reduces to

$$\vec{E}^A = \eta \vec{J}_0 - \frac{m_i}{\rho_D e} \vec{\nabla} \cdot \vec{\vec{\pi}}_{0,e}. \qquad (2.76)$$

Such an expression remains consistent with the solution to a Grad Shafranov equation by treating the applied equilibrium electric field ($\vec{E}_A$) as the field which should have been applied to generate the desired equilibrium pressure and q profiles. Conveniently, for the initial value equations this equilibrium equation will be subtracted from Ohm's law; then $\vec{E}_A$ and the equilibrium $\vec{\vec{\pi}}_{0,e}$ need never be computed.

From Faraday's law, the perturbed electric field may be expressed in terms of a vector potential and a scalar potential ,

$$\vec{E}_1 = -\frac{1}{c}\frac{\partial \vec{A}}{\partial t} + \nabla \alpha, \tag{2.77}$$

where α is the electrostatic potential and is determined by the radial projection of Ohm's law, i.e., the gauge condition. The radial projection is

$$\frac{\partial \alpha}{\partial \rho} + \frac{I}{R^2}\frac{\partial \phi_1}{\partial \rho} = +\epsilon J_\rho + \frac{\mu_e}{\nu_{ei}}\hat{e}_\rho \cdot \nabla \cdot \vec{\vec{\pi}}_e, \tag{2.78}$$

where α has been normalized by

$$\alpha^* = \epsilon^2 \frac{I_{wall} R_0}{c\tau_R}. \tag{2.79}$$

Since $\mu_e/\nu_{ei} \sim 2.3\epsilon^{1/2}$, the solution to Eq. (2.78) to lowest order in ϵ is

$$\alpha = -\frac{I}{R^2}\phi_1, \tag{2.80}$$

or that ϕ_1 is basically the electrostatic potential. This is also consistent with the lowest order in ϵ solution of the $\hat{e}_\theta$ projection of Ohm's law.

Next, the lowest order in ϵ parallel $(\vec{B}\cdot)$ projection of Ohm's law is

$$\begin{aligned} \frac{\partial \psi_1}{\partial \tau} &= \frac{I}{R^2}\left[\frac{\partial \phi_1}{\partial \zeta} - \frac{1}{q}\frac{\partial \phi_1}{\partial \theta}\right] - \frac{1}{\rho R^2}\frac{\partial \phi_1}{\partial \theta}\frac{\partial \psi_1}{\partial \rho} + \frac{1}{\rho R^2}\frac{\partial \phi}{\partial \rho}\frac{\partial \psi}{\partial \theta} \\ &\quad + R^2 J_1^\zeta - \frac{R^2}{I}\vec{B} \cdot \nabla \cdot \vec{\vec{\pi}}_e, \end{aligned} \tag{2.81}$$

where all quantities have been normalized. (This equation generates most of the previously defined normalizations when written in a dimensional form.) Ordering of the stress tensor term is completed by first considering $(p_{||} - p_\perp)_e$

$$(p_{||} - p_\perp)_e = -2\frac{\langle B^2 \rangle}{\left\langle \left[\frac{\vec{B}\cdot\nabla B^2}{B^2}\right]^2 \right\rangle} \left\{ \frac{1}{\epsilon^2}\frac{\mu_e}{\omega_{ce}}\frac{\vec{v}\cdot\nabla(B^2)}{B^2} - \frac{\mu_e}{\nu_e}\frac{\vec{J}\cdot\nabla(B^2)}{B^2} \right\}, \tag{2.82}$$

in which $\omega_{ce} = eB/m_e c$ is the electron cyclotron frequency. To reduce the above equation to a programmable form, the flux-surface-averaged terms will be based on equilibrium quantities, as will factors of $1/B^2$. Such an approximation is valid because the particle trapping is not strongly affected by the presence of the island. Smolyakov [29] has calculated the change in the viscosity due to such variations and found them to be small, when the islands are sufficiently small.

The normalization factors scale roughly as $\mu_e/\omega_{ce} \sim 10^{-7}$ and $\mu_e/\nu_e \sim 2.3\epsilon^{1/2}$, which indicate the velocity component may be neglected. Next, only equilibrium and linear terms of $\vec{J}\cdot\nabla(B^2)$ are retained. Spong [30] indicates that the contribution of similar nonlinear terms is small. Therefore, the electron pressure anisotropy is

$$\begin{aligned}(p_{\|}-p_{\perp})_e \;=\; & +2\frac{\mu_e}{\nu_e}\frac{\langle B_0^2\rangle}{\left\langle\left[\frac{\vec{B}_0\cdot\nabla B_0^2}{B_0^2}\right]^2\right\rangle}\frac{1}{B_0^2}\left\{\vec{J}_0\cdot\nabla(B_0^2)+\vec{J}_1\cdot\nabla(B_0^2)\right.\\ & \left.+\vec{J}_0\cdot\nabla(\vec{B}_1\cdot\vec{B}_0)\right\}. \qquad (2.83)\end{aligned}$$

From Section 2.2.7, $\vec{B}_1\cdot\vec{B}_0$ will be expressed in terms of the pressure. Then, to lowest order

$$\begin{aligned}(p_{\|}-p_{\perp})_e \;=\; & \frac{2}{\epsilon^2}\frac{\mu_e}{\nu_e}\frac{\langle B_0^2\rangle}{\left\langle\left[\frac{\vec{B}_0\cdot\nabla B_0^2}{B_0^2}\right]^2\right\rangle}\left\{\frac{1}{R^2B_0^2}\frac{1}{\rho}\frac{\partial B_0^2}{\partial\theta}\frac{dI}{d\rho}-\frac{\beta}{IB_0^2}\frac{1}{\rho}\frac{\partial B_0^2}{\partial\theta}\frac{\partial p}{\partial\rho}\right.\\ & \left.-\frac{\beta}{R^2B_0^2}\frac{dI}{d\rho}\frac{1}{\rho}\frac{\partial p}{\partial\theta}+\frac{\beta}{IB_0^2}\frac{\partial B_0^2}{\partial\rho}\frac{1}{\rho}\frac{\partial p}{\partial\theta}\right\}. \qquad (2.84)\end{aligned}$$

Next, the parallel projection of the stress-tensor term of Eq. (2.17) is computed and found to be

$$\vec{B}\cdot\nabla\cdot\vec{\vec{\pi}}_e=\frac{2}{3}\vec{B}\cdot\nabla(p_{\|}-p_{\perp})_e-\frac{1}{2}\frac{(p_{\|}-p_{\perp})_e}{B^2}\vec{B}\cdot\nabla(B^2), \qquad (2.85)$$

which when expanded into a form suitable for numerical implementation becomes

$$\begin{aligned}
-\frac{R^2}{I}\vec{B}\cdot\nabla\cdot\vec{\vec{\pi}}_e \simeq\ & \frac{\partial p_1}{\partial\rho}\left\{\frac{-\beta}{\epsilon^2}\frac{\mu_e}{\nu_e}\frac{\langle B_0^2\rangle}{\left\langle\left[\frac{\vec{B_0}\cdot\nabla B_0^2}{B_0^2}\right]^2\right\rangle}\frac{1}{R^2B_0^4}\frac{\rho}{q}\left(\frac{1}{\rho}\frac{\partial B_0^2}{\partial\theta}\right)^2\right\} \\
& +\frac{1}{\rho}\frac{\partial p_1}{\partial\theta}\left\{\frac{\beta}{\epsilon^2}\frac{\mu_e}{\nu_e}\frac{\langle B_0^2\rangle}{\left\langle\left[\frac{\vec{B_0}\cdot\nabla B_0^2}{B_0^2}\right]^2\right\rangle}\frac{1}{R^2B_0^4}\frac{1}{\rho}\frac{\partial B_0^2}{\partial\theta}\frac{\rho}{q}\left[\frac{\partial B_0^2}{\partial\rho}-\frac{I}{R^2}\frac{dI}{d\rho}\right]\right\} \\
& +\frac{1}{\rho}\frac{\partial p_1}{\partial\theta}\left\{\frac{-2\beta}{\epsilon^3}\frac{\mu_e}{\nu_e}\frac{\langle B_0^2\rangle}{\left\langle\left[\frac{\vec{B_0}\cdot\nabla B_0^2}{B_0^2}\right]^2\right\rangle}\frac{1}{R^4B_0^4}\frac{\rho I}{q}\frac{1}{\rho}\frac{\partial B_0^2}{\partial\theta}\frac{dI}{d\rho}\right\} \\
& +\frac{\partial p_1}{\partial\zeta}\left\{\frac{2\beta}{\epsilon^3}\frac{\mu_e}{\nu_e}\frac{\langle B_0^2\rangle}{\left\langle\left[\frac{\vec{B_0}\cdot\nabla B_0^2}{B_0^2}\right]^2\right\rangle}\frac{1}{R^4B_0^4}\frac{1}{\rho}\frac{\partial B_0^2}{\partial\theta}I\frac{dI}{d\rho}\right\} \\
& +\frac{\partial\psi_1}{\partial\rho}\left\{\frac{1}{\epsilon^2}\frac{\mu_e}{\nu_e}\frac{\langle B_0^2\rangle}{\left\langle\left[\frac{\vec{B_0}\cdot\nabla B_0^2}{B_0^2}\right]^2\right\rangle}\frac{1}{R^4B_0^4}\frac{dI}{d\rho}\left(\frac{1}{\rho}\frac{\partial B_0^2}{\partial\theta}\right)^2\right\} \\
& +\frac{1}{\rho}\frac{\partial\psi_1}{\partial\theta}\left\{\frac{-1}{\epsilon^2}\frac{\mu_e}{\nu_e}\frac{\langle B_0^2\rangle}{\left\langle\left[\frac{\vec{B_0}\cdot\nabla B_0^2}{B_0^2}\right]^2\right\rangle}\frac{1}{R^4B_0^4}\frac{dI}{d\rho}\frac{\partial B_0^2}{\partial\rho}\frac{1}{\rho}\frac{\partial B_0^2}{\partial\theta}\right\},
\end{aligned}\tag{2.86}$$

where the nonlinear contributions have been dropped [30]. Also, the $\vec{B}\cdot\nabla(p_{||}-p_{\perp})_e$ has been ordered small and therefore dropped. A flux surface average of this quantity would also annihilate this latter term. Equation 2.86 is the model which will be used to describe the perturbed bootstrap current.

2.3.7 Toroidal vorticity evolution

The toroidal vorticity evolution equation is generated by operating on the momentum balance equation with the operator $\nabla\zeta\cdot\nabla\times$. The result is

$$\frac{\rho_D}{\tau_R^2R_0}\frac{\partial w^\zeta}{\partial\tau}=\rho_D\nabla\cdot\left(\vec{w}v^\zeta-\vec{v}w^\zeta\right)+\frac{1}{c}\nabla\cdot\left(\vec{B}J^\zeta-\vec{J}B^\zeta\right)-\nabla\zeta\cdot\nabla\times\nabla\cdot\vec{\vec{\pi}},\tag{2.87}$$

where ρ_D is the plasma density which is assumed to be a constant. The normalized vorticity evolution equation detailed in a form necessary for the numerical implementation is

$$\begin{aligned}\frac{\partial w^\zeta}{\partial \tau} = {} & \frac{1}{\rho R^2}\frac{\partial \phi}{\partial \rho}\frac{\partial w^\zeta}{\partial \theta} - \frac{1}{\rho R^2}\frac{\partial \phi}{\partial \theta}\frac{\partial w^\zeta}{\partial \rho} + S^2\left\{\frac{1}{\rho R^2}\frac{\partial \psi}{\partial \theta}\frac{\partial J_0^\zeta}{\partial \rho} - \frac{1}{\rho R^2}\frac{\partial \psi}{\partial \rho}\frac{\partial J_0^\zeta}{\partial \theta}\right. \\ & - J_1^\rho \frac{\partial}{\partial \rho}\left(\frac{I}{R^2}\right) - J_1^\theta \frac{\partial}{\partial \theta}\left(\frac{I}{R^2}\right) + \frac{I\rho}{R^2 q}\frac{1}{\rho}\frac{\partial}{\partial \theta}J_1^\zeta + \frac{I}{R^2}\frac{\partial}{\partial \zeta}J_1^\zeta \\ & \left. + \frac{1}{\rho R^2}\frac{\partial \psi}{\partial \theta}\frac{\partial J_1^\zeta}{\partial \rho} - \frac{1}{\rho R^2}\frac{\partial \psi}{\partial \rho}\frac{\partial J_1^\zeta}{\partial \theta}\right\} - \nabla \zeta \cdot \nabla \times \nabla \cdot \vec{\vec{\pi}}. \end{aligned} \tag{2.88}$$

The interpretation of each of these terms is as follows. The first two terms on the right-hand-side represent the convection of vorticity, the $\vec{J}_1^\rho$ and $\vec{J}_1^\theta$ are curvature pieces and expand as

$$\begin{aligned} J_1^\rho \frac{\partial}{\partial \rho}\left(\frac{I}{R^2}\right) + J_1^\theta \frac{\partial}{\partial \theta}\left(\frac{I}{R^2}\right) = {} & \left\{\frac{1}{\rho}\frac{\partial^2 \psi_1}{\partial \theta \partial \zeta}\right\}\left\{\frac{\hat{g}^{\rho\theta}}{R^2}\frac{\partial}{\partial \rho}\left(\frac{I}{R^2}\right) + \frac{\hat{g}^{\theta\theta}}{R^2}\frac{1}{\rho}\frac{\partial}{\partial \theta}\left(\frac{I}{R^2}\right)\right\} \\ & + \left\{\frac{1}{\rho}\frac{\partial^2 \psi_1}{\partial \rho \partial \zeta}\right\}\left\{\frac{\hat{g}^{\rho\rho}}{R^2}\frac{\partial}{\partial \rho}\left(\frac{I}{R^2}\right) + \frac{\hat{g}^{\rho\theta}}{R^2}\frac{1}{\rho}\frac{\partial}{\partial \theta}\left(\frac{I}{R^2}\right)\right\} \\ & + \left\{\frac{1}{\rho}\frac{\partial p_1}{\partial \theta}\right\}\left\{\frac{-\beta_0}{\epsilon^2}\frac{1}{I}\frac{\partial}{\partial \rho}\left(\frac{I}{R^2}\right)\right\} \\ & + \left\{\frac{\partial p_1}{\partial \rho}\right\}\left\{\frac{\beta_0}{\epsilon^2}\frac{1}{I}\frac{1}{\rho}\frac{\partial}{\partial \theta}\left(\frac{I}{R^2}\right)\right\} \end{aligned} \tag{2.89}$$

The last two terms of Eq. (2.89) are often referred to as the pressure curvature pieces and lead to the Glasser effect [31, 32], which produces a stabilizing effect linearly and nonlinear when the equilibrium has good average curvature. The 6 remaining current pieces are the linear and nonlinear portions of $\vec{B} \cdot \nabla J^\zeta$. The final stress tensor term is the ion viscosity. For the numerical implementation, the J_1^ζ terms must also be expanded into operators on ψ_1, so that

$$\begin{aligned} \frac{I}{R^2}\frac{\partial}{\partial \zeta}J_1^\zeta = {} & \frac{1}{\rho}\frac{\partial^2 \psi_1}{\partial \theta \partial \zeta}\left\{\frac{I}{R^4}\left[\frac{\partial}{\partial \rho}\hat{g}^{\rho\theta} + \frac{1}{\rho}\frac{\partial}{\partial \theta}\hat{g}^{\theta\theta}\right]\right\} + \frac{1}{\rho}\frac{\partial^3 \psi_1}{\partial \theta \partial \rho \partial \zeta}\left\{\frac{2I}{R^4}\hat{g}^{\rho\theta}\right\} \\ & + \frac{\partial^3 \psi_1}{\partial \zeta \partial \rho^2}\left\{\frac{I}{R^4}\hat{g}^{\rho\rho}\right\} + \frac{1}{\rho^2}\frac{\partial^3 \psi_1}{\partial \zeta \partial \theta^2}\left\{\frac{I}{R^4}\hat{g}^{\theta\theta}\right\} \\ & + \frac{\partial^2 \psi_1}{\partial \zeta \partial \rho}\left\{\frac{I}{R^4}\left[\frac{1}{\rho}\frac{\partial}{\partial \rho}\rho \hat{g}^{\rho\rho} + \frac{1}{\rho}\frac{\partial}{\partial \theta}\hat{g}^{\rho\theta}\right]\right\}, \end{aligned} \tag{2.90}$$

and also

$$
\begin{aligned}
\frac{I\rho}{R^2 q}\frac{1}{\rho}\frac{\partial}{\partial\theta}J_1^\zeta = {} & \frac{1}{\rho^2}\frac{\partial^2\psi_1}{\partial\theta^2}\left\{\frac{I\rho}{qR^4}\left[\frac{\partial}{\partial\rho}\hat{g}^{\rho\theta}+\frac{1}{\rho}\frac{\partial}{\partial\theta}\hat{g}^{\theta\theta}\right]\right\}+\frac{1}{\rho^2}\frac{\partial^3\psi_1}{\partial\theta^2\partial\rho}\left\{\frac{I\rho}{qR^4}2\hat{g}^{\rho\theta}\right\} \\
& +\frac{1}{\rho^3}\frac{\partial^3\psi_1}{\partial\theta^3}\left\{\frac{I\rho}{qR^4}\hat{g}^{\theta\theta}\right\}+\frac{1}{\rho}\frac{\partial^2\psi_1}{\partial\theta\partial\rho}\left\{\frac{I\rho}{qR^4}\left[\frac{1}{\rho}\frac{\partial}{\partial\rho}\rho\hat{g}^{\rho\rho}+\frac{1}{\rho}\frac{\partial}{\partial\theta}\hat{g}^{\rho\theta}\right]\right\} \\
& +\frac{1}{\rho}\frac{\partial^3\psi_1}{\partial\theta\partial\rho^2}\left\{\frac{I\rho}{qR^4}\hat{g}^{\rho\rho}\right\} \\
& +\frac{1}{\rho}\frac{\partial\psi_1}{\partial\theta}\left\{\frac{1}{R^2\rho}\frac{\partial}{\partial\theta}\left[\frac{I\rho}{qR^2}\left(\frac{\partial}{\partial\rho}\hat{g}^{\rho\theta}+\frac{1}{\rho}\frac{\partial}{\partial\theta}\hat{g}^{\theta\theta}\right)\right]\right\} \\
& +\frac{1}{\rho}\frac{\partial^2\psi_1}{\partial\theta\partial\rho}\left\{\frac{1}{R^2}\frac{1}{\rho}\frac{\partial}{\partial\theta}\left[\frac{I\rho}{qR^2}2\hat{g}^{\rho\theta}\right]\right\}+\frac{1}{\rho^2}\frac{\partial^2\psi_1}{\partial\theta^2}\left\{\frac{1}{R^2}\frac{1}{\rho}\frac{\partial}{\partial\theta}\left[\frac{I\rho}{qR^2}\hat{g}^{\theta\theta}\right]\right\} \\
& +\frac{\partial^2\psi_1}{\partial\rho^2}\left\{\frac{1}{R^2}\frac{1}{\rho}\frac{\partial}{\partial\theta}\left[\frac{I\rho}{qR^2}\hat{g}^{\rho\rho}\right]\right\} \\
& +\frac{\partial\psi_1}{\partial\rho}\left\{\frac{1}{R^2}\frac{1}{\rho}\frac{\partial}{\partial\theta}\left[\frac{I\rho}{qR^2}\left(\frac{1}{\rho}\frac{\partial}{\partial\rho}\rho\hat{g}^{\rho\rho}+\frac{1}{\rho}\frac{\partial}{\partial\theta}\hat{g}^{\rho\theta}\right)\right]\right\}.
\end{aligned}
\tag{2.91}
$$

2.3.8 Neoclassical closure for the momentum balance

The reduction of the pair of stress-tensor terms which appear in the momentum balance proceeds in several steps. First, the electron stress-tensor term is smaller than the ion stress-tensor term by $\sim (m_e/m_i)^{1/2}$ and thus can be neglected. Next, Eq. (2.17) is split into the two notationally convenient components

$$
\nabla\cdot\vec{\vec{\pi}}_A = \vec{B}\vec{B}\cdot\nabla\left(\frac{f}{B^2}\right)+\frac{f}{B^2}\nabla\left(\frac{B^2}{2}\right)-\frac{f}{B^2}\vec{B}\times\nabla\times\vec{B}, \tag{2.92}
$$

$$
\nabla\cdot\vec{\vec{\pi}}_B = -\frac{1}{3}\nabla f, \tag{2.93}
$$

where $f = p_{||} - p_\perp$ and

$$
\nabla\cdot\vec{\vec{\pi}} = \nabla\cdot\vec{\vec{\pi}}_A + \nabla\cdot\vec{\vec{\pi}}_B. \tag{2.94}
$$

Furthermore, the closure simplifies to

$$
\nabla\zeta\cdot\nabla\times\nabla\cdot\vec{\vec{\pi}} = \nabla\zeta\cdot\nabla\times\nabla\cdot\vec{\vec{\pi}}_A. \tag{2.95}
$$

To generate an expression for $\nabla\zeta\cdot\nabla\times\nabla\cdot\vec{\vec{\pi}}_A$ the $\vec{J}\times\vec{B}$ expression from the momentum balance is substituted into Eq. (2.92) and then solved for $\nabla\cdot\vec{\vec{\pi}}_A$.

The result is

$$\begin{aligned}\nabla\cdot\vec{\vec{\pi}}_A &= \frac{1}{1-\frac{f}{B^2}}\left\{\vec{B}\vec{B}\cdot\nabla\left(\frac{f}{B^2}\right)+\frac{f}{B^2}\nabla\left(\frac{B^2}{2}\right)\right.\\ &\left.+\frac{f}{B^2}\left[\rho_D\frac{D\vec{v}}{Dt}+\nabla p+\nabla\cdot\vec{\vec{\pi}}_B\right]\right\}, \qquad (2.96)\end{aligned}$$

where $f=(p_{||}-p_{\perp})$ and $D/Dt=\partial/\partial t+\vec{v}\cdot\nabla$. Since $f/B^2\sim S^{-2}\mu_i/\nu_{ei}\ll 1$, Eq. 2.96 becomes

$$\nabla\cdot\vec{\vec{\pi}}_A\simeq\left\{\vec{B}\vec{B}\cdot\nabla\left(\frac{f}{B^2}\right)+\frac{f}{B^2}\nabla\left(\frac{B^2}{2}\right)\right\}. \qquad (2.97)$$

This result is now substituted into Eq. (2.95) and common terms are collected. The stress-tensor term is then

$$\nabla\zeta\cdot\nabla\times\nabla\cdot\vec{\vec{\pi}}=\nabla\zeta\times\nabla\cdot\left[\vec{B}\vec{B}\cdot\nabla\left(\frac{f}{B^2}\right)\right]+\frac{1}{2}\nabla\zeta\cdot\nabla\left(\frac{f}{B^2}\right)\times\nabla B^2. \quad (2.98)$$

The first term is neglected since it is $O(\epsilon)$ smaller than the second term. After the various operators are expanded and also approximating $B^2\simeq B_0^2$, the stress tensor term becomes

$$\begin{aligned}\nabla\zeta\cdot\nabla\times\nabla\cdot\vec{\vec{\pi}} &= \left\{\frac{\partial^2\phi}{\partial\rho^2}\right\}\left\{\frac{1}{\epsilon^2}\frac{\mu_i}{\nu_{ei}}\frac{1}{B^2R^2}\frac{1}{R^2}\frac{\langle B^2\rangle}{\left\langle\left[\frac{\vec{B}\cdot\nabla B^2}{B^2}\right]^2\right\rangle}\left(\frac{1}{\rho}\frac{\partial B^2}{\partial\theta}\right)^2\right\}\\ &+ \left\{\frac{\partial\phi}{\partial\rho}\right\}\left\{-\frac{1}{\epsilon^2}\frac{\mu_i}{\nu_{ei}}\frac{1}{B^2R^2}\frac{1}{\rho}\frac{\partial^2}{\partial\rho\partial\theta}\left[\frac{B^2}{R^2}\frac{\langle B^2\rangle}{\left\langle\left[\frac{\vec{B}\cdot\nabla B^2}{B^2}\right]^2\right\rangle}\frac{1}{\rho}\frac{\partial B^2}{\partial\theta}\right]\right\}\\ &+ \left\{\frac{1}{\rho^2}\frac{\partial^2\phi}{\partial\theta^2}\right\}\left\{\frac{1}{\epsilon^2}\frac{\mu_i}{\nu_{ei}}\frac{1}{B^2R^2}\frac{1}{R^2}\frac{\langle B^2\rangle}{\left\langle\left[\frac{\vec{B}\cdot\nabla B^2}{B^2}\right]^2\right\rangle}\left(\frac{\partial B^2}{\partial\rho}\right)^2\right\}\\ &+ \left\{\frac{1}{\rho}\frac{\partial\phi}{\partial\theta}\right\}\left\{\frac{1}{\epsilon^2}\frac{\mu_i}{\nu_{ei}}\frac{1}{B^2R^2}\frac{\partial^2}{\partial\rho\partial\theta}\left[\frac{B^2}{R^2}\frac{\langle B^2\rangle}{\left\langle\left[\frac{\vec{B}\cdot\nabla B^2}{B^2}\right]^2\right\rangle}\frac{1}{\rho}\frac{\partial B^2}{\partial\rho}\right]\right\}\\ &+\left\{\frac{1}{\rho}\frac{\partial^2\phi}{\partial\rho\partial\theta}\right\}\left\{-\frac{2}{\epsilon^2}\frac{\mu_i}{\nu_{ei}}\frac{1}{B^2R^2}\frac{1}{R^2}\frac{\langle B^2\rangle}{\left\langle\left[\frac{\vec{B}\cdot\nabla B^2}{B^2}\right]^2\right\rangle}\frac{\partial B^2}{\partial\rho}\frac{1}{\rho}\frac{\partial B^2}{\partial\theta}\right\}. \quad (2.99)\end{aligned}$$

2.4 Pressure Evolution

The pressure evolution equation for an incompressible plasma is

$$\frac{\partial p}{\partial t} + \vec{v}_1 \cdot \nabla p = Q - \nabla \cdot \vec{q}, \tag{2.100}$$

where the heat flux is

$$\vec{q} = -\chi_\perp \nabla p - (\chi_\| - \chi_\perp)\frac{\vec{B}\vec{B} \cdot \nabla p}{B^2}, \tag{2.101}$$

Q is the plasma heating source, and $\chi_\perp$ and $\chi_\|$ are the perpendicular and parallel pressure diffusivities, respectively. Both will be treated as constants.

One of the difficulties in the numerical implementation of this pressure equation is to connect the heat source term Q, which is generally unknown, with the equilibrium pressure profile, which is the input required for the equilibrium code. To simplify the numerical implementation, the pressure is decomposed into the equilibrium and fluctuating portions:

$$p = p_0 + p_1. \tag{2.102}$$

The revised pressure equation is then

$$\frac{\partial p_1}{\partial t} + \vec{v}_1 \cdot \nabla p_0 + \vec{v}_1 \cdot \nabla p_1 = \nabla \cdot \vec{q}_1, \tag{2.103}$$

where Q has been balanced with the equilibrium portion of the heat flux and changes to the resistive heating are deemed to be small. The $\vec{q}_1$ fluctuation is given by

$$\vec{q}_1 = -\chi_\perp \nabla p_1 - (\chi_\| - \chi_\perp)\left[\frac{\vec{B}\vec{B} \cdot \nabla p_1}{B^2} + \frac{\vec{B}\vec{B}_1 \cdot \nabla p_0}{B^2}\right], \tag{2.104}$$

where $\vec{B}_0 \cdot \nabla p_0$ is equal to zero, since the equilibrium pressure profile is a flux function [i.e., $p_0 = p_0(\rho)$ and $\vec{B} \cdot \nabla \rho = 0$].

Next, the convective portion of Eq. (2.103) is expanded into a form suitable for numerical implementation:

$$\frac{\partial p_1}{\partial \tau} = \frac{1}{\rho R^2}\frac{\partial \phi_1}{\partial \theta}\frac{\partial p_0}{\partial \rho} + \frac{1}{\rho R^2}\frac{\partial \phi_1}{\partial \theta}\frac{\partial p_1}{\partial \rho} - \frac{1}{\rho R^2}\frac{\partial \phi_1}{\partial \rho}\frac{\partial p_1}{\partial \theta} - \nabla \cdot \vec{q}_1. \tag{2.105}$$

The "perpendicular" portion of $-\nabla \cdot \vec{q}_1$ is given by

$$\begin{aligned}
-\nabla \cdot \vec{q_\perp} \;=\;& \chi_\perp \left\{ \frac{\partial^2 p_1}{\partial \rho^2} \left\{ \hat{g}^{\rho\rho} \right\} + \frac{\partial p_1}{\partial \rho} \left\{ \frac{1}{\rho R^2} \frac{\partial}{\partial \rho} \hat{g}^{\rho\rho} \rho R^2 + \frac{1}{\rho R^2} \frac{\partial}{\partial \theta} \hat{g}^{\rho\theta} \rho R^2 \right\} \right. \\
& + \frac{1}{\rho} \frac{\partial^2 p_1}{\partial \rho \partial \theta} \left\{ 2 \hat{g}^{\rho\theta} \right\} + \frac{1}{\rho} \frac{\partial p_1}{\partial \theta} \left\{ \frac{1}{R^2} \frac{\partial}{\partial \rho} \hat{g}^{\rho\theta} R^2 + \frac{1}{\rho R^2} \frac{\partial}{\partial \theta} \hat{g}^{\theta\theta} R^2 \right\} \\
& \left. + \frac{1}{\rho^2} \frac{\partial^2 p_1}{\partial \theta^2} \left\{ \hat{g}^{\theta\theta} \right\} + \frac{\partial^2 p_1}{\partial \zeta^2} \left\{ \frac{\epsilon^2}{R^2} \right\} \right\}, \qquad (2.106)
\end{aligned}$$

where the perpendicular diffusivity has been normalized by $\epsilon^2 R_0^2 / \tau_R$. Since $-\nabla \cdot \vec{q_\perp} \sim \nabla^2 p_1$, the operator ∇^2 is easily observed to decompose into $\epsilon^{-2} \nabla_\wedge^2 + 1/R^2 \partial^2 / \partial \zeta^2$. The parallel heat flux is decomposed into two linear terms and one group of nonlinear terms:

$$\begin{aligned}
-\nabla \cdot \vec{q}_\parallel \;=\;& (\chi_\parallel - \chi_\perp) \vec{B}_0 \cdot \nabla \left(\frac{\vec{B}_0 \cdot \nabla p_1}{B_0^2} \right) + \\
& (\chi_\parallel - \chi_\perp) \vec{B}_0 \cdot \nabla \left(\frac{\vec{B}_1 \cdot \nabla p_0}{B_0^2} \right) + \\
& (\chi_\parallel - \chi_\perp) \left[\vec{B}_0 \cdot \nabla \left(\frac{\vec{B}_1 \cdot \nabla p_1}{B_0^2} \right) + \right. \\
& \left. \vec{B}_1 \cdot \nabla \left(\frac{\vec{B}_0 \cdot \nabla p_1}{B_0^2} + \frac{\vec{B}_1 \cdot \nabla p_0}{B_0^2} + \frac{\vec{B}_1 \cdot \nabla p_1}{B_0^2} \right) \right], \qquad (2.107)
\end{aligned}$$

where $1/B^2 \simeq 1/B_0^2$. Now each of these terms is expanded in a form suitable for numerical implementation:

$$\begin{aligned}
\text{Term 1} \;=\;& \frac{\partial^2 p_1}{\partial \zeta^2} \left\{ \frac{I^2}{R^2} \frac{1}{R^2 B_0^2} \right\} + \frac{1}{\rho} \frac{\partial^2 p_1}{\partial \theta \partial \zeta} \left\{ \frac{2 \rho I^2}{R^2 q} \frac{1}{R^2 B_0^2} \right\} + \\
& \frac{\partial p_1}{\partial \zeta} \left\{ \frac{\rho I^2}{R^2 q} \frac{1}{\rho} \frac{\partial}{\partial \theta} \frac{1}{R^2 B_0^2} \right\} + \frac{1}{\rho^2} \frac{\partial^2 p_1}{\partial \theta^2} \left\{ \frac{\rho^2 I^2}{R^2 q^2} \frac{1}{R^2 B_0^2} \right\} + \\
& \frac{1}{\rho} \frac{\partial p_1}{\partial \theta} \left\{ \frac{\rho^2 I^2}{R^2 q^2} \frac{1}{\rho} \frac{\partial}{\partial \theta} \frac{1}{R^2 B_0^2} \right\}, \qquad (2.108)
\end{aligned}$$

$$\begin{aligned}
\text{Term 2} \;=\;& -\frac{1}{\rho} \frac{\partial^2 \psi_1}{\partial \theta \partial \zeta} \left\{ \frac{I}{R^2} \frac{1}{B_0^2 R^2} \frac{d p_0}{d \rho} \right\} - \frac{1}{\rho^2} \frac{\partial^2 \psi_1}{\partial \theta^2} \left\{ \frac{\rho I}{R^2 q} \frac{1}{B_0^2 R^2} \frac{d p_0}{d \rho} \right\} + \\
& -\frac{1}{\rho} \frac{\partial \psi_1}{\partial \theta} \left\{ \frac{\rho I}{R^2 q} \frac{d p_0}{d \rho} \frac{1}{\rho} \frac{\partial}{\partial \theta} \frac{1}{B_0^2 R^2} \right\}. \qquad (2.109)
\end{aligned}$$

The last term of Eq. (2.107), Term 3, is a nonlinear term and is dealt with differently than the linear terms in the numerical implementation (see the numerical implementation section). To reduce computational time, Term 3 must be expressed in a form which minimizes the total number of operations. Hence, Term 3 becomes

$$\text{Term 3} \;=\; \frac{I}{R^2}\left(\frac{\partial g_3}{\partial \zeta}+\frac{\rho}{q}\frac{1}{\rho}\frac{\partial g_3}{\partial \theta}\right)+\frac{1}{\rho R^2}\left\{\frac{\partial \psi_1}{\partial \rho}\frac{\partial f_3}{\partial \theta}-\frac{\partial \psi_1}{\partial \theta}\frac{\partial f_3}{\partial \rho}\right\}, \tag{2.110}$$

where

$$g_3=\frac{1}{B_0^2R^2}\left\{\frac{1}{\rho}\frac{\partial \psi_1}{\partial \rho}\frac{\partial p_1}{\partial \theta}-\frac{1}{\rho}\frac{\partial \psi_1}{\partial \theta}\frac{\partial p_1}{\partial \rho}\right\}, \tag{2.111}$$

and

$$f_3=g_3+\frac{1}{B_0^2R^2}\left\{I\frac{\partial p_1}{\partial \zeta}+\frac{\rho I}{q}\frac{1}{\rho}\frac{\partial p_1}{\partial \theta}-\frac{1}{\rho}\frac{\partial \psi_1}{\partial \theta}\frac{dp_0}{d\rho}\right\}. \tag{2.112}$$

2.5 Energy Integral

The neoclassical reduced MHD model presented satisfies an energy integral, which is computed by a summation of the multiplication of the parallel Ohm's law plus equilibrium Ohm's law by $J_0^\zeta + J_1^\zeta$, with the multiplication of the vorticity evolution by $S^{-2}\phi$, and the multiplication of the pressure equation by $\beta\epsilon^{-2}lnI/R^2$. This result is then integrated over the plasma volume. The result is

$$\begin{aligned}
\frac{\partial}{\partial t}\int d^3V\left\{\frac{1}{2}|\nabla\zeta\times\nabla\left(\psi_0+\psi_1\right)|^2+\frac{1}{2}|\nabla\zeta\times\nabla\phi_1|^2-\frac{\beta}{\epsilon^2}pln\frac{I}{R^2}\right\} = \\
-\int d^3V\Big\{\left(J_{1\zeta}+J_{0\zeta}\right)\left(J_1^\zeta+J_0^\zeta\right) \\
+\left(J_0^\zeta+J_1^\zeta\right)\left(\frac{R^2}{I}\vec{B}\cdot\nabla\cdot\vec{\vec{\pi}}_e+\frac{R^2}{I}\vec{B}\cdot\nabla\cdot\vec{\vec{\pi}}_{e,eq}\right)+\frac{1}{S^2}\vec{v}\cdot\nabla\cdot\vec{\vec{\pi}}_i \\
+\frac{\nu}{S^2}w^\zeta\left(\frac{\partial^2\phi}{\partial\rho^2}+\frac{\phi}{\rho^2}\frac{\partial^2\phi}{\partial\theta^2}+\frac{\phi}{\rho}\frac{\partial\phi}{\partial\rho}\right) \\
-\frac{\beta}{\epsilon^2}ln\frac{I}{R^2}\left[-Q+\chi_\perp\nabla^2p+\left(\chi_\parallel-\chi_\perp\right)\vec{B}\cdot\nabla\left(\frac{\vec{B}\cdot\nabla p}{B^2}\right)\right]\Big\} \\
+\int d^3V\left\{\left(J_0^\zeta+J_1^\zeta\right)E^{A\zeta}\right\}.
\end{aligned} \tag{2.113}$$

The first term (ψ_1) on the left-hand-side (LHS) of the equal sign represents the energy in the magnetic fluctuations, the second term (ϕ_1) on the LHS represents the kinetic energy of flows in the plasma, the third term can either be interpreted as the energy in the magnetic fluctuations associated with $\vec{B}_0 \cdot \vec{B}_1$ or more commonly as the interchange term [25].

The third term on the LHS develops from the $\vec{J} \times \vec{B}$ force in the momentum balance. Recall that the energy integral for the full MHD equations is developed by vector multiplication (dot product) of the momentum equation with $\vec{v}$ and the Ohm's law dotted with $\vec{J}$. The resultant $\vec{v} \cdot \vec{J} \times \vec{B}$ cancel each other in the Ohm's law and the momentum equation. In this model when ϕ is multiplied by the vorticity equation, a term of the form $I/R^2 \vec{J}_{1/\epsilon} \cdot \nabla\phi_1$ develops, where $\vec{J}_{1/\epsilon}$ is the order $1/\epsilon$ perturbed current of Eq. (2.62). This current depends only on χ and therefore the pressure and also has no toroidal component. This term can be shown to explicitly cancel with appropriate terms from the poloidal and radial projections from the full MHD Ohm's law. However, since these equations are not explicitly solved in the numerical simulations , the "correct" procedure is to base the energy balance only on the set of equations which are time advanced. In that case, the above term can be massaged into the form $ln(I/R^2)\vec{v} \cdot \nabla p$. The $ln(I/R^2)$ moment of the pressure equation can then be used to generate term 3 of the LHS and term 5 of the right-hand-side (RHS) of Eq. (2.113). These terms have the general feature that when integrated over the plasma volume, the only non-zero contributions are pressure perturbations which change equilibrium harmonics (i.e., $n = 0$ toroidal harmonics). Also, in the limit of cylindrical geometry ($I = 1, R^2 = 1$), these terms vanish exactly. In comparison with Hazeltine and Meiss [25], $Q = 0$, $\chi_\perp = 0$, and $\chi_\| = 0$ so that these dissipation terms do not appear. Term 3 of the LHS is then described as the stabilizing effect of good average curvature in the tokamak.

The terms on the right-hand-side (RHS) represent energy sources and sinks. The first term on the RHS, J^2 is the resistive dissipation and is manifestly negative. The second and third set of terms on the RHS represent electron and ion stress viscous dissipation. The fourth term is a numerical viscous dissipation. This viscosity has minimal impact on the numerical results, but was added primarily to improve numerical stability by increasing grid coupling in the vorticity equation. To lowest order in ϵ, this term is positive, because the operators on ϕ are nearly equivalent to those in w^ζ. The operator is a carryover from the original Charlton numerical implementation [22] and should be rewritten and reprogrammed for future work. The fifth term on the RHS is less easily interpretable, since it does not appear to be convertible to a positive definite form. Perhaps as with the pressure curvature term, the term produces dissipation on the average. The sixth and final term on the RHS is an energy source from the applied electric field. (The neoclassical MHD simulations have been run with the Glasser terms disabled to avoid this possible energy source.)

Finally, the pressure equation also satisfies an energy integral independent of the above analysis. The form is

$$\begin{aligned}\frac{\partial}{\partial t}\int d^3V\frac{p^2}{2} &= \int d^3V pQ \\ &\quad - \int d^3V\left\{\chi_\perp\left|\nabla p\right|^2 + \chi_{||}\frac{\left|\vec{B}\cdot\nabla p\right|^2}{B^2}\right\}. \end{aligned} \tag{2.114}$$

2.6 Numerical Model

The numerical model implemented in the FARGO code consists of a Fourier decomposition in the poloidal and toroidal directions and a central-finite differencing scheme in the radial or flux coordinate direction. The advantage of such a representation is that it provides the most accurate method for computing the operator $\vec{B}_0\cdot\nabla$ since it reduces the operator to the algebraic form $(I/R^2)(-m/q+n)$. An accurate evaluation of this operator is important because in the evolution equations the operator $\vec{B}_0\cdot\nabla$ appears numerous places and is often multiplied by a large coefficient (i.e., S^2 or $\chi_{||}$, which can be $> 10^{10}$ for reactor grade plasmas), which makes it prone to numerical error. Since only up/down symmetric tokamak equilibria will be considered, the following Fourier decomposition is used for fluctuation quantities:

$$\psi_1 = \sum_l \psi_l(\rho_j)\cos(m_l\theta + n_l\zeta), \tag{2.115}$$

$$\phi_1 = \sum_l \phi_l(\rho_j)\sin(m_l\theta + n_l\zeta), \tag{2.116}$$

$$p_1 = \sum_l p_l(\rho_j)\cos(m_l\theta + n_l\zeta), \tag{2.117}$$

where the summation is over the modes "included" in the calculation. Equilibrium quantities are similarly Fourier decomposed except with no toroidal dependence. To clarify which modes are included in the calculation, this study should be contrasted with turbulence calculations which require a summation over a very large set of modes (> 5000) to accurately produce results [33]. However, in the case of magnetic islands/tearing modes, usually only a few modes are unstable and they tend to be large and coherent in nature. Furthermore, the poloidal mode coupling between various helicities is typically on the order of ϵ so that just a few modes are required to include the effects from coupled modes. Consequently, an accurate model of magnetic island phenomena can be described with relatively few harmonics.

The FARGO code is an initial value code, and each simulation has been initialized with a perturbation of the form

$$\psi_{m,n}(\rho, \tau = 0) = \begin{cases} \psi_{start}\rho^m, & \rho < \rho_s \\ \psi_{start}\frac{(1-\rho^{-m})}{(1-\rho_s^{-m})}, & \rho > \rho_s, \end{cases} \tag{2.118}$$

where ψ_{start} is the initial perturbation magnitude and ρ_s is the radial location of the rational surface. This initial perturbation approximates the eigenfunction for a stable Δ' tearing mode and accurately reproduces the mode shape near the magnetic axis and conducting wall. This perturbation shape also reduces the time required for initial transients to decay and leave only the desired eigenfunction. Finally, a finite perturbation of this type assists the initial destabilization of the neoclassical tearing mode.

As an illustration of the time advance, the basic equations can be expressed as follows

$$\frac{\partial \vec{\vec{L}} \cdot \vec{x}}{\partial t} = \vec{\vec{R}} \cdot \vec{x} + \vec{N}(\vec{x}); \qquad \vec{x} = \begin{bmatrix} \psi_1 \\ \phi_1 \\ p_1 \\ w_1^\zeta \end{bmatrix}, \tag{2.119}$$

where $\vec{\vec{L}}$ and $\vec{\vec{R}}$ are linear operators and $\vec{N}$ represents the nonlinear terms. In general, $\vec{\vec{L}}$ and $\vec{\vec{R}}$ are a series of block tridiagonal matrices. The matrices are tridiagonal due to the central-differencing in the flux coordinate ρ and are block due to both the four equations and also because of poloidal mode coupling. The exact details are not important for the current discussion. However, the form of the time-differencing is important since it has important implications for the stability of the calculation. The central time-differencing scheme takes the form

$$\left(\vec{\vec{L}} - \frac{\Delta t}{2}\vec{\vec{R}}\right) \cdot \vec{x}^{t+\Delta t} = \left(\vec{\vec{L}} + \frac{\Delta t}{2}\vec{\vec{R}}\right) \cdot \vec{x}^{t} + \Delta t \vec{N}(\vec{x}). \tag{2.120}$$

Numerically, the linear portion is solved implicitly with a block tridiagonal solver [34] and the nonlinear term is solved explicitly. Initially, in the linear phase, large time steps can be taken. However, when the nonlinear terms become important, the explicit nature of the nonlinear term requires Δt to be reduced to insure stability. In the linear regime, an Alfven time is often needed ($\Delta\tau = 1/S$), and, in the nonlinear regime for an island width of 20% of the plasma minor radius, $\Delta t = 0.001/S$.

Throughout the simulations a uniform spatial mesh of 500 radial grid points has been chosen, with the exception of parameter scans over the magnetic Reynold's number S. In that case, 300 radial grid points are localized within a gap of 0.05 about the resonant rational surface; then 100 grid points are placed between each of the boundaries and the boundaries of the localized mesh. The two meshes begin to disagree for $S \sim 10^9$. The absolute maximum on the mesh appears to be about 1000 grid points, at which point point the block solver indicates the matrix has become singular.

Finally, the "convolutions" which are required when equilibrium quantities are multiplied together, or when fluctuation quantities are combined, are dealt with as a spectral sum over the coupled modes with nonzero weights $w_{i,j,k}$, i.e.,

$$\vec{N}_i\left(\vec{x}\right) = \sum_{j,k} w_{i,j,k}\phi_j\psi_k \quad , \tag{2.121}$$

where the subscripts i, j, k each refer to a specific m and n helicity.

Chapter 3

Numerical Results

This chapter covers a wide range of observations based on numerical simulations for both single and multiple helicity magnetic islands in toroidal geometry which, within a resistive MHD model, are either unstable or stable but driven unstable by either poloidal mode coupling to an unstable mode or by neoclassical bootstrap currents. A convenient organizational scheme to describe this collection of tearing modes is to begin with a single helicity tearing mode and then add complexity to the model. To accomplish this task, preliminary concepts and definitions that are common to the analysis of the tearing modes are presented in Section 3.1. In Section 3.2, the results of numerical simulations for standard resistive MHD (Δ') unstable tearing modes are presented. In the first subsection, 3.2.1, of this section numerical simulations based on low β toroidal equilibria are used to benchmark the code with theoretical predictions of the linear, Rutherford, and saturation growth regimes for single helicity tearing modes. Next, the plasma pressure, as measured by β_0 will be increased and shown to stabilize the tearing mode through curvature effects. In the final subsection, 3.2.2, poloidal mode coupling is demonstrated. The final section of this chapter, Section 3.3, presents results of numerical simulations for single helicity magnetic islands that are stable to resistive MHD instabilities but instead are driven by the neoclassical bootstrap current.

3.1 Preliminaries

3.1.1 Profile parameterization

Throughout much of the following analysis, the q-profiles will be parameterized by [41]

$$q = q_0 \left(1 + \left(\frac{\rho}{\rho_0}\right)^{2\lambda}\right)^{1/\lambda}, \tag{3.1}$$

where ρ_0 is determined by the limiter or edge value of q,

$$\rho_0 = \left(\left(\frac{q_{limiter}}{q_0}\right)^{\lambda} - 1\right)^{-1/2\lambda}. \tag{3.2}$$

In general, three values of λ have been considered: $\lambda = 1$, 2, and 3. The effect of increasing λ is to peak the current profile near the magnetic axis. Additionally, the equilibrium pressure profile has been parameterized by

$$p_0 = 1 - a\rho^2 - (1+a)\rho^3, \tag{3.3}$$

where $0 < a < 3$ to insure a monotonically decreasing pressure profile. Additional details pertaining to specific equilibria that have been used throughout these simulations, are provided in Appendix A.

3.1.2 Island width evaluation

Before proceeding to a detailed analysis of various tearing modes, various definitions are required. First, the helical flux is defined as

$$\psi^* = \left\{\int_{\rho_0}^{\rho} d\rho\, \rho I \left(\frac{1}{q_0} - \frac{1}{q}\right)\right\} - \sum_{m,n} \psi_{m,n}(\rho) \cos(m\theta + n\zeta), \tag{3.4}$$

where $\rho = \rho_0$ occurs at $q = q_0$, q is the q-profile corrected for the nonlinear generation of a 0/0 current, and q_0 is the q value at a particular rational surface. The helical flux describes the amount of flux passing a helical ribbon between a surface in the plasma relative to the rational surface $q = q_0$. Figure 3.1 illustrates contours of constant ψ^* for a typical $m/n = 2/1$ mode. The procedure for determination of the island width from the helical flux is illustrated in Figure 3.2. First, the minimum value of the helical flux across the X-point is identified. Next, the two values of ρ, ρ_+ and ρ_- are determined by locating the values of

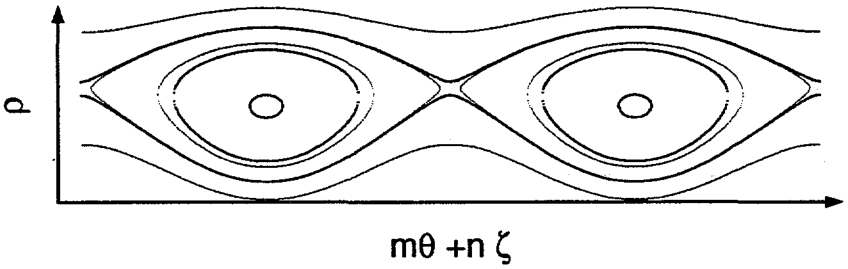

Figure 3.1: The contours of constant helical flux ψ^* illustrating the X-points and O-points for a single helicity 2/1 magnetic island. The helical flux is used to compute the island width.

ψ^* across the O-point which equal this minimum X-point value. The difference in these two values is then the island width in terms of the normalized flux coordinate ρ. When the island width is small and for a single helicity mode, the nonlinear correction to q is small and an analytical formula for the island width can be developed by Taylor expansion of ψ^*. The resultant island width is

$$\rho_+ - \rho_- = 4 \left(\frac{\psi_{m/n}}{\rho_0} \frac{1}{q_0^2} \left. \frac{dq}{d\rho} \right|_{\rho=\rho_0} \right)^{0.5} \tag{3.5}$$

While analytically this procedure is straightforward, when the island width is smaller than the local grid size, a numerical evaluation of the island width cannot be computed. In general this will not pose a problem, since the region of primary interest is for large macroscopic islands in the nonlinear regime, rather than micro-magnetic islands. The only caveat to this statement is that some of the benchmarks compare the numerical results for linear tearing modes with theory. However, in these cases the growth rates can still be computed either directly from the growth rate of $\psi_{m/n}$ or from a magnetic fluctuation energy growth rate. The problem can be marginally ameliorated by localizing the spatial grid about the rational surface of interest. However, for multiple helicity modes a uniform grid is preferable.

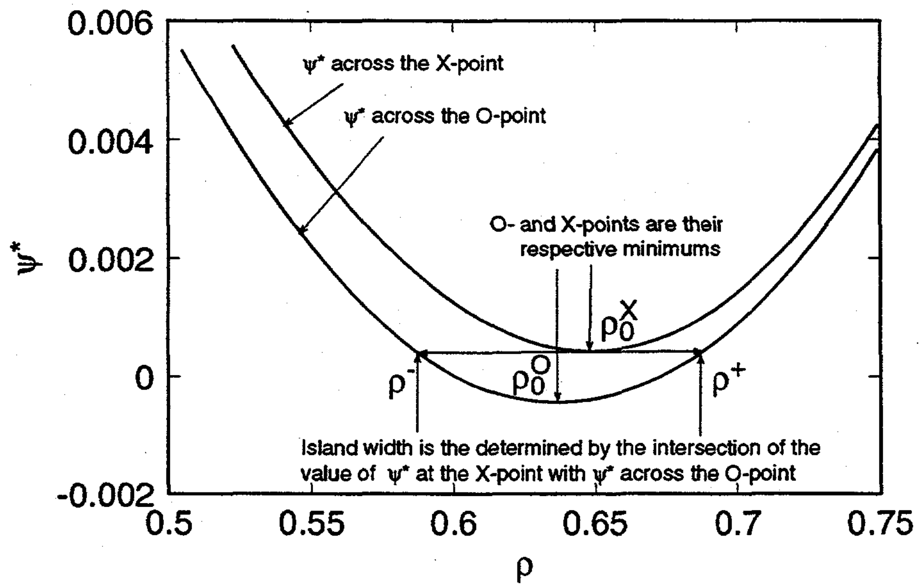

Figure 3.2: The procedure for computing the island width from the helical flux ψ^* is to compute the island width across the X-point and O-points. The minimum value across the X-point defines the X-point and provides a value of ψ^* on the island separatrix. The two values across the O-point which correspond to this value determine the island width in terms of the flux coordinate ρ.

3.2 Standard Tearing Mode

The standard tearing mode is defined in this context as a tearing mode which is driven not by neoclassical effects ($\mu_e = \mu_i = 0$) but is instead driven by gradients in the equilibrium current. The foray into these modes will begin with a qualitative benchmarking of the numerical simulations by a comparison of a single helicity mode with existing theory. Only a qualitative benchmarking is possible since most of the analytic theory is for cylindrical geometries and all of the simulations which follow will be for toroidal geometries. A single helicity mode will refer to a resonant mode (e.g., the $m = 2/n = 1$ resonant at the $q = 2$ surface) and the equilibrium modes (i.e., all the $n = 0$ harmonics used to describe the equilibrium). Furthermore, single helicity will not include higher harmonics of the resonant surface (e.g., the 4/2 and 6/3 are resonant at the $q = 2$ surface) nor poloidaly coupled peripheral modes (e.g., the 1/1 and 3/1) which nonlinearly couple to the 2/1 mode. While this thesis does not demonstrate the role the higher harmonics have on the principal harmonic, the simulations are extended to include multiple helicities in subsection 3.2.2 and a qualitative comparison with the toroidal coupling physics of E-matrix [8, 37] theory is made, which suggests that the coupling is $O(\epsilon)$. This section is completed with a discussion of the pressure evolution dynamics.

3.2.1 Dynamics of a single helicity magnetic island

The basic phenomenology of the time evolution of an unstable single helicity tearing mode is illustrated in Figure 3.3. The initial linear growth regime, where the mode width increases exponentially in time, is observed by considering the magnetic fluctuation energy. (The island width is smaller than the radial mesh size.) As the island width approaches the resistive layer width, the flux reconnection at the X-point slows and the mode amplitude grows linearly with time. Finally, the nonlinear generation of an $m = 0/n = 0$ current flattens the local current gradient, eliminates the drive mechanism for the island $[\Delta'(w_{sat}) = 0]$, and saturates the island width at a width w_{sat}. These three regimes, linear, Rutherford, and saturation phases, will be used to qualitatively benchmark the numerical simulations with existing theoretical predictions.

The linear growth rate for the tearing mode at small amplitude in cylindrical geometry, and therefore with no pressure/curvature effects, is predicted to be [35]

$$\gamma\tau_R = \left(\frac{\Delta'}{2.12366}\right)^{4/5} \left(\frac{m}{\rho_0 L_s}\right)^{2/5} S^{2/5}, \tag{3.6}$$

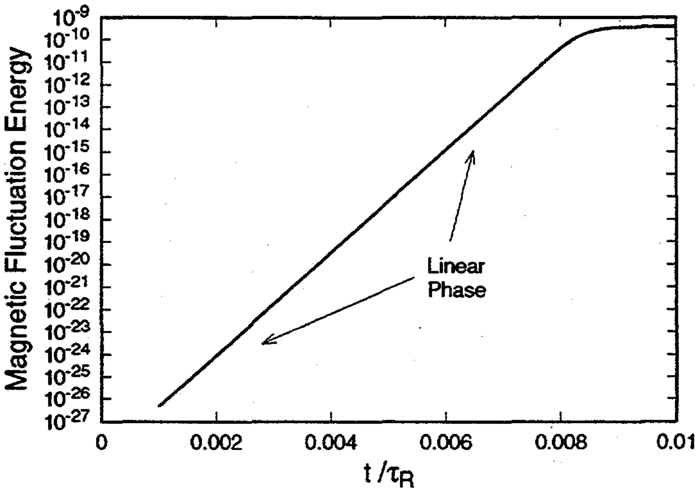

Figure 3.3: The $m = 2/n = 1$ magnetic island grows exponentially in time when the island is small. Parameters of $S = 10^7$, $\epsilon = 0.25$, $\chi_\perp = 10^2$, and $\chi_{||} = 10^6$ have been assumed. Neoclassical viscous effects are neglected and the conventional viscosity coefficient is $\mu = 10^{-5}$.

where Δ' is the tearing mode matching parameter, S is the magnetic Reynold's number, m is the poloidal mode number, ρ_0 is the radius of the mode resonance, and L_s is the local magnetic shear length. While the numerical simulations presented here are strictly for toroidal geometry and Eq. (3.6) was developed for cylindrical geometry, Eq. (3.6) is still implicitly correct since this growth rate is due to the inherently slablike nature of the layer physics. The toroidal geometry enters through Δ'.

The parameter Δ' warrants further discussion, since it is the general criterion often quoted for the stability (< 0) or instability (> 0) of the tearing mode in theoretical discourses. The simulations presented here do not formally compute this parameter Δ', which represents the free energy available for reconnection [43], because this parameter represents an analytic solution to the problem of asymptotic matching of an outer ideal MHD solution far from the resonant rational surface to the resistive inner boundary layer solution in the vicinity of the resonant rational surface. The numerical simulations do not and cannot formally separate these two regions.

Another important check on the linear simulations is whether the S scaling indicated by Eq. (3.6) is observed. Figure 3.4 illustrates the observed asymptotic scaling of the growth rate normalized to the resistive time is $S^{0.44}$, which agrees relatively well with the theoretical expectation of $S^{0.4}$. This deviation is likely attributable to both higher order corrections from toroidicity and modification of the growth rate do to viscosity. At sufficiently large S ($S \sim 10^{10}$), the asymptotic behavior breaks down because the spatial mesh can no longer resolve the vorticity and the solution becomes erratic. At low S, theory also breaks down because the resistive layer,

$$\delta_R = \left(\frac{\Delta'}{2.12366}\right)^{1/5} \left(\frac{L_s \rho_0}{Sm}\right)^{2/5}, \tag{3.7}$$

is no longer small ($\ll 1$). An estimate of the normalized Δ' for the case being considered based on the asymptotic behavior is $\Delta' \simeq 16$, where $m/\rho_0 L_s = 2.36$. The prior analysis was based on the pressure/curvature piece term turned off,

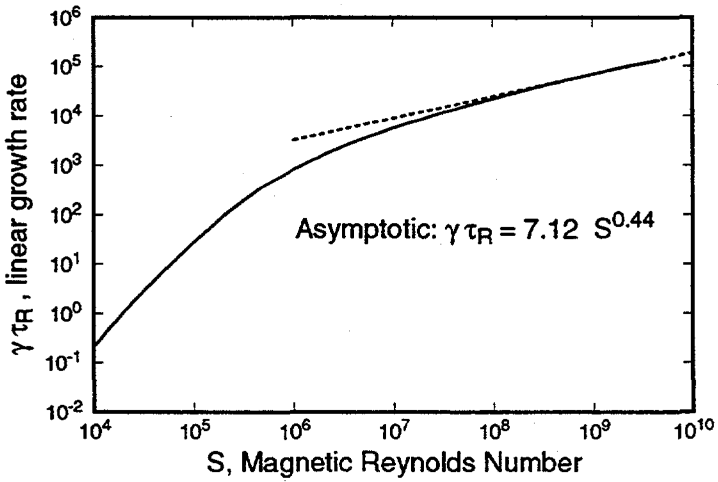

Figure 3.4: Single helicity S scan for the $m = 2/n = 1$ magnetic island illustrates the asymptotic behavior of the tearing mode in the absence of the pressure curvature term. Values of $\chi_\perp = 100$, and $\chi_\| = 10^6$ have been chosen, neoclassical viscous effects are neglected and the conventional viscosity coefficient is $\mu = 10^{-5}$.

since in cylindrical geometry the curvature piece is naturally zero. In the presence of the pressure curvature piece, additional stabilization of the tearing mode is predicted (a.k.a. the Glasser effect [31]) and indicated in Figure 3.5. The figure suggests an asymptotic behavior, but cannot be demonstrated because the solutions at values of $S > 10^8$ become ideally unstable due to the rapid growth of a 2/1 mode localized about a region near the magnetic axis where $dq/d\rho = 0$. This difficulty is common to all the equilibria generated by the RSTEQ equilibrium solver, which has numerical problems near the magnetic axis.

The stabilization due to the plasma pressure curvature effect is more readily identified, as illustrated in Figure 3.6, if a parameter scan of the linear growth rate versus the plasma pressure β_0 is conducted with the pressure curvature terms turned on and off. The figure identifies about half of the stabilization occurs directly from changes in the metric elements due to the Shafranov shift at increasing β_0 and the other half directly from the pressure curvature terms.

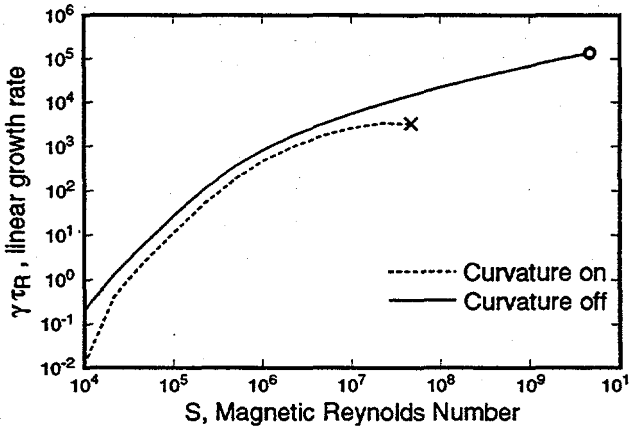

Figure 3.5: Single helicity S scan for the $m = 2/n = 1$ magnetic island which demonstrates the stabilizing effect of the pressure curvature term on the linear mode. Values of $\chi_\perp = 100$, and $\chi_\| = 10^6$ have been chosen, neoclassical viscous effects are neglected and the conventional viscosity coefficient is $\mu = 10^{-5}$.

As the island width becomes sufficiently large, the mode changes from an exponential growth rate to a growth rate which is proportional to t, as illustrated in Figure 3.7. This growth phase, referred to as the Rutherford regime [14], is expected to take place when $W \gtrsim \delta_R$, where W is the island width. From the previous estimates of Δ', the resistive layer is approximately $\delta_R \simeq 0.0016$ and as illustrated in Figure 3.7 this agrees well with the observation of the Rutherford regime. Analytically, the island width is expected to be

$$\frac{dw}{dt} \simeq \Delta', \tag{3.8}$$

where Δ' is the tearing mode matching condition. In this regime, the nonlinear portion of $\vec{B} \cdot \nabla J$, that appears in the vorticity evolution equation, generates eddy currents, which, when crossed with the radial component of the perturbed magnetic field, produce a force that opposes the vortex flow. As the mode grows this effect dominates over the inertia (dw^ζ/dt) and causes the growth rate to

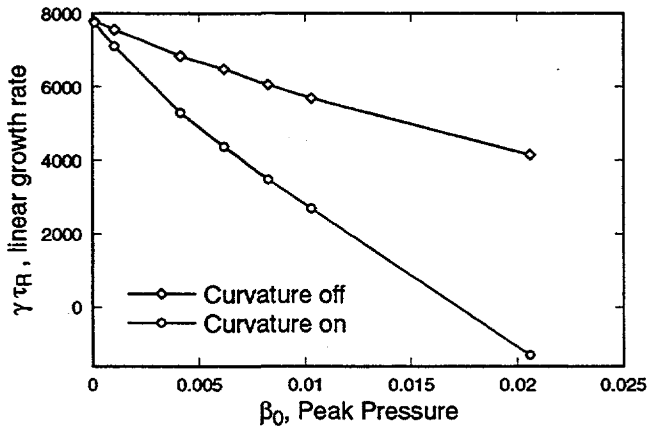

Figure 3.6: Linear stabilization of the tearing mode due to increasing pressure is caused by a combination of the pressure curvature effect and geometric changes caused by the Shafranov shift. The pressure profile is parameterized by the peak pressure on axis.

slow from exponential to linear. The nonlinearly generated equilibrium current is still small in this regime and the stabilization is not from quasilinear flattening of the equilibrium current.

In the saturation phase ($\gamma\tau_R \to 0$), the mode eventually generates an equilibrium current sufficient to flatten the current profile about the 2/1 surface [36]. This current flattening eliminates the current gradient drive mechanism for the island and the mode saturates. The temporal behavior of the island width in this region is observed to be approximated by

$$\frac{dW}{dt} = \Delta'(0)\left(1 - \frac{W_{sat}}{W}\right), \tag{3.9}$$

where $\Delta'(0)$ is the Δ' at zero island width and W_{sat} is the saturated island width.

The final feature of the various regimes to check is the qualitative character of the eigenfunctions. The eigenfunctions for the 2/1 and the 0/0 components are illustrated in Figures 3.9 through 3.14 covering a time slice corresponding to the linear, Rutherford, and saturation phases. The higher order equilibrium harmonics up to an $m = 10/n = 0$ employed in the calculations have not been displayed. All these eigenfunctions are based on the set of parameters: $S = 10^7$, $\epsilon = 0.25$, $\chi_\perp = 10^2$, $\chi_\parallel = 10^6$, $\mu = 10^{-5}$, $\mu_e = 0$, and $\mu_i = 0$. The common features to be observed are: 1) The shape of $\psi_{2/1}$, especially about the rational surface where a large jump in the gradient of $\psi_{2/1}$ exists which

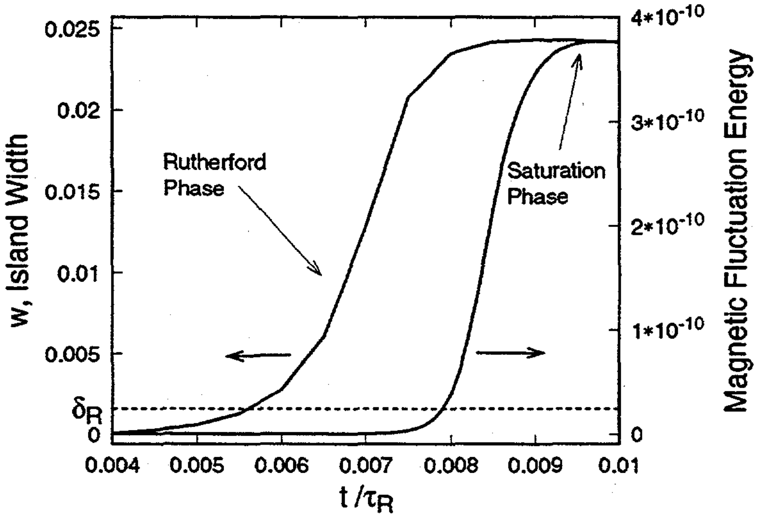

Figure 3.7: Prior to mode saturation, the $m = 2/n = 1$ magnetic island width grows linearly in time. Values of $S = 10^7$, $\epsilon = 0.25$ $\chi_\perp = 10$, and $\chi_{||} = 10^6$ have been assumed. Neoclassical viscous effects are neglected and the conventional viscosity coefficient is $\mu = 10^{-5}$.

corresponds to Δ'; 2) The value of $\psi_{2/1}$ is approximately constant across the resistive layer, which is necessary to satisfy the constant ψ approximation used to derive the theory; 3) Near the magnetic axis $\psi_{2/1}$ has an r^m behavior and near the conducting wall boundary it has an r^{-m} behavior. (This behavior is common for all the $m \neq 0, n \neq 0$ modes); 4) Both $\phi_{2/1}$ and $w^\zeta_{2/1}$ are localized in the vicinity of the magnetic island within roughly the resistive layer width δ_R; 5) The $\phi_{2/1}$ is roughly a factor of S larger than $\psi_{2/1}$, which is more a reflection of the normalizations rather than a flow velocity much larger than the magnetic field; 6) The helical portion of the pressure perturbation corresponds to the helical structure of ψ, which is indicative of pressure equilibration on the flux surfaces; and 7) A reduction in the 0/0 component of the pressure on axis due to fast parallel transport around the island (see subsection 3.2.2). The feature which does not correspond to theoretical expectations is that $\phi_{2/1}$ should be odd about the mode rational surface; here, in toroidal geometry a mixing of the magnetic tearing (even) and twisting (odd) parity modes could generate the observed behavior.

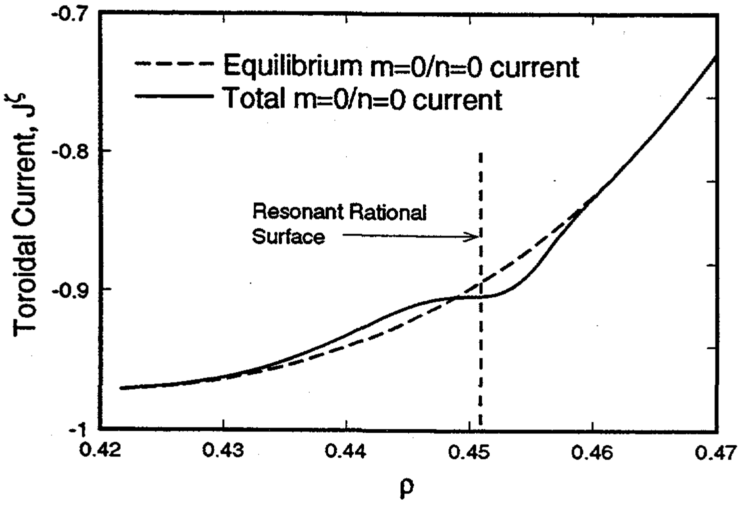

Figure 3.8: Nonlinear generation of $m/n = 0/0$ currents produce a quasilinear flattening of the equilibrium current which eliminates the current gradient drive for the island.

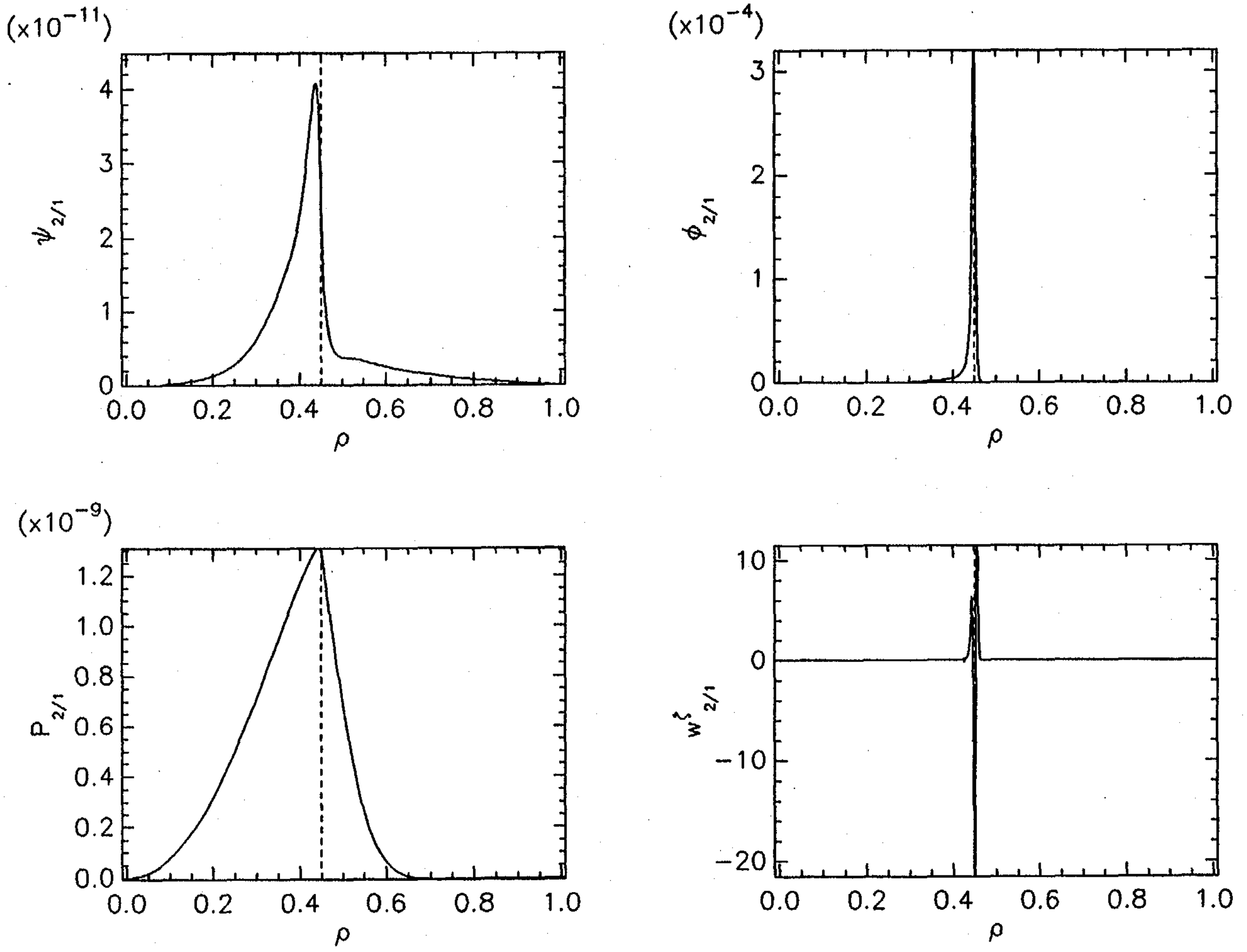

Figure 3.9: Eigenfunctions for the 2/1 mode in the linear regime for equilibrium A.1. The vertical dashed line indicates the location of the rational surface in terms of ρ the radial flux coordinate.

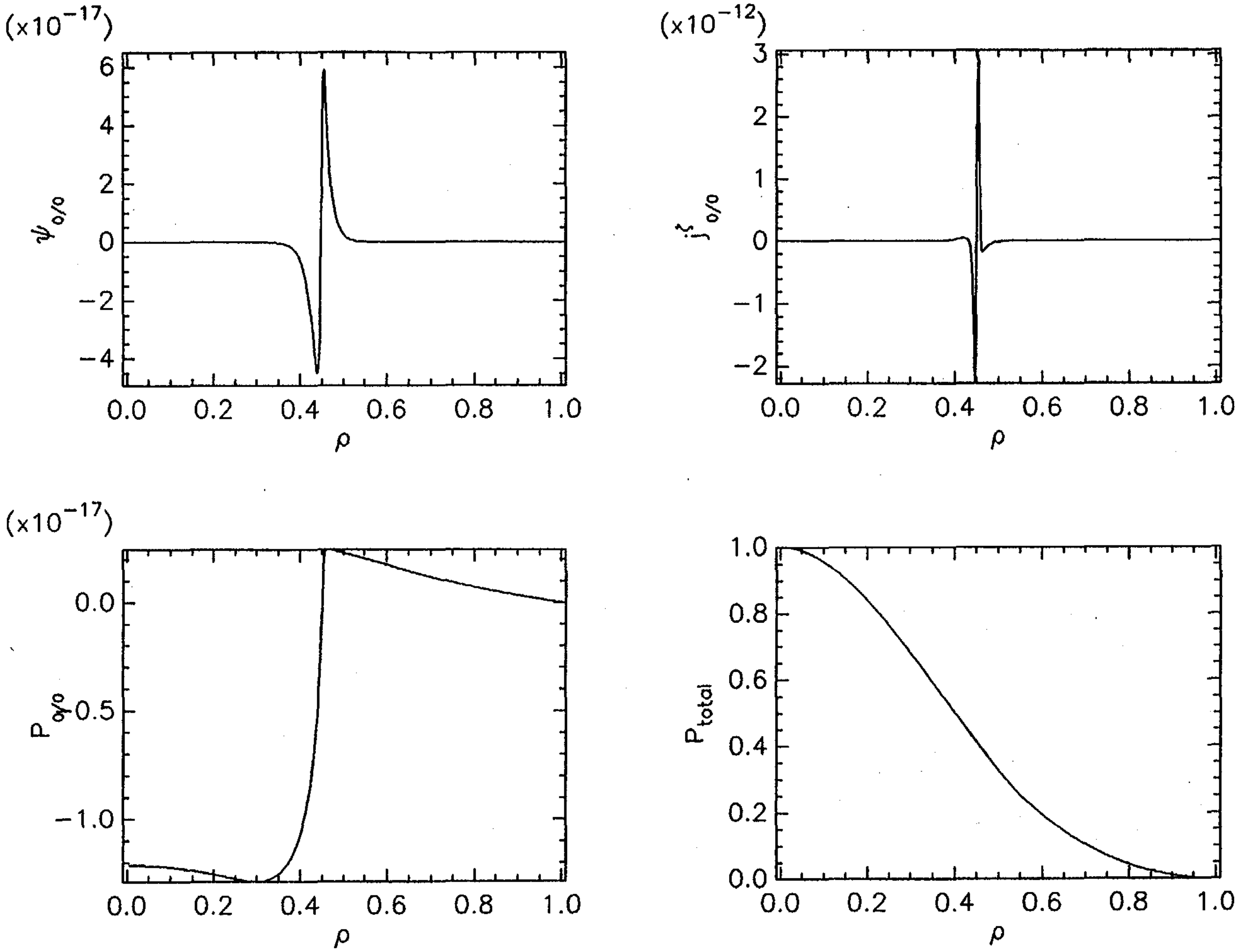

Figure 3.10: Eigenfunctions for the 0/0 mode in the linear regime for equilibrium A.1.

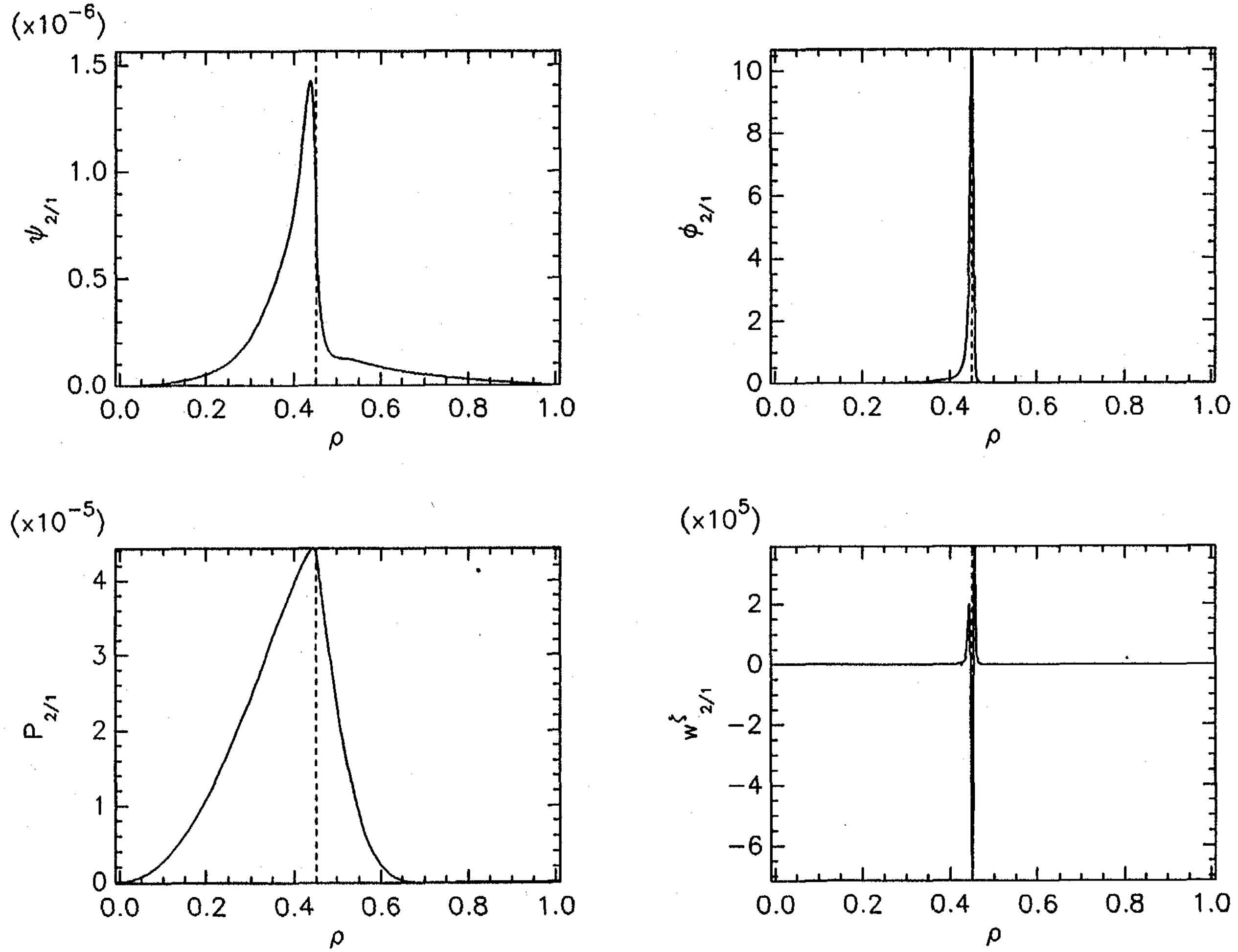

Figure 3.11: Eigenfunctions for the 2/1 mode in the Rutherford regime for equilibrium A.1.

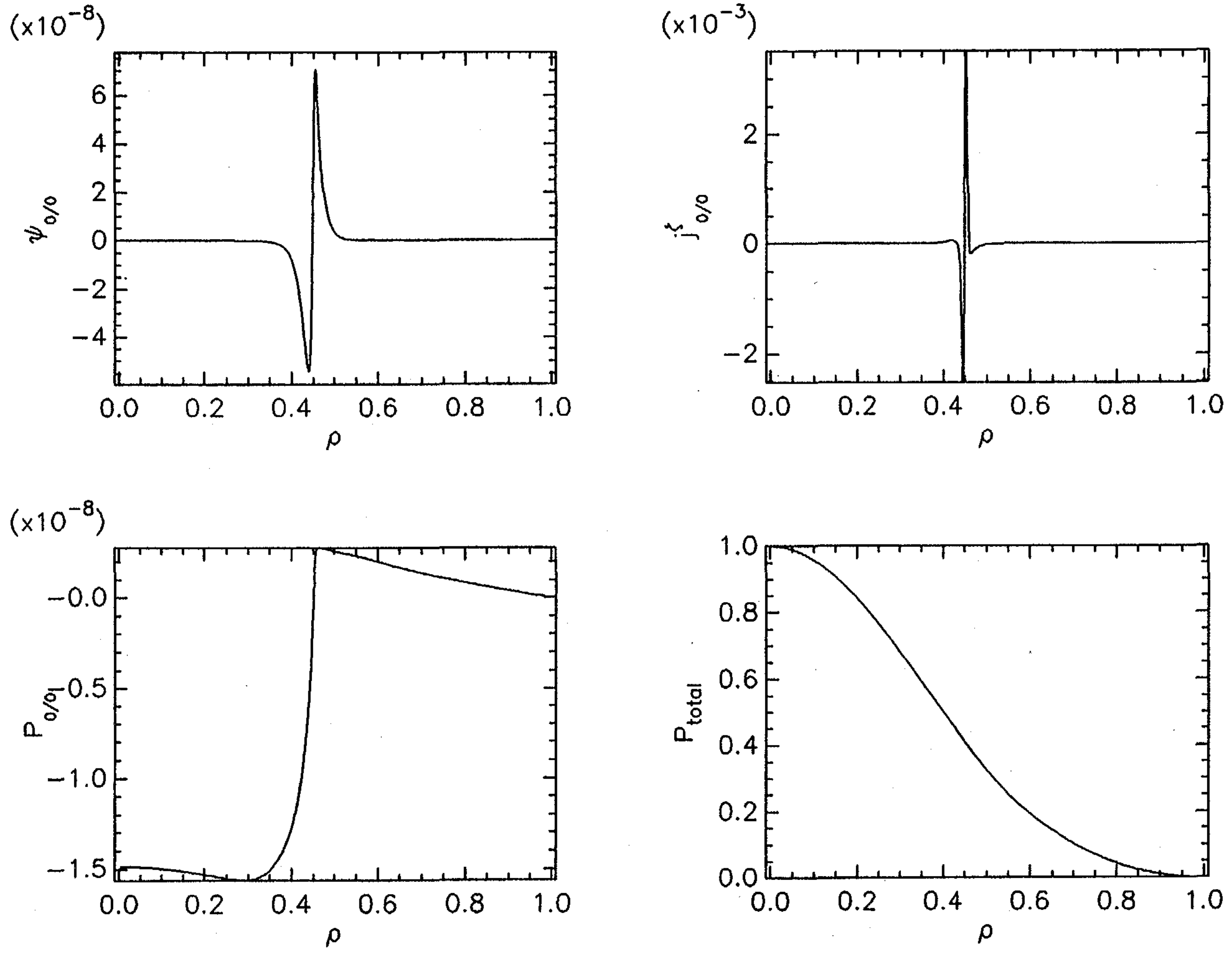

Figure 3.12: Eigenfunctions for the 0/0 mode in the Rutherford regime for equilibrium A.1.

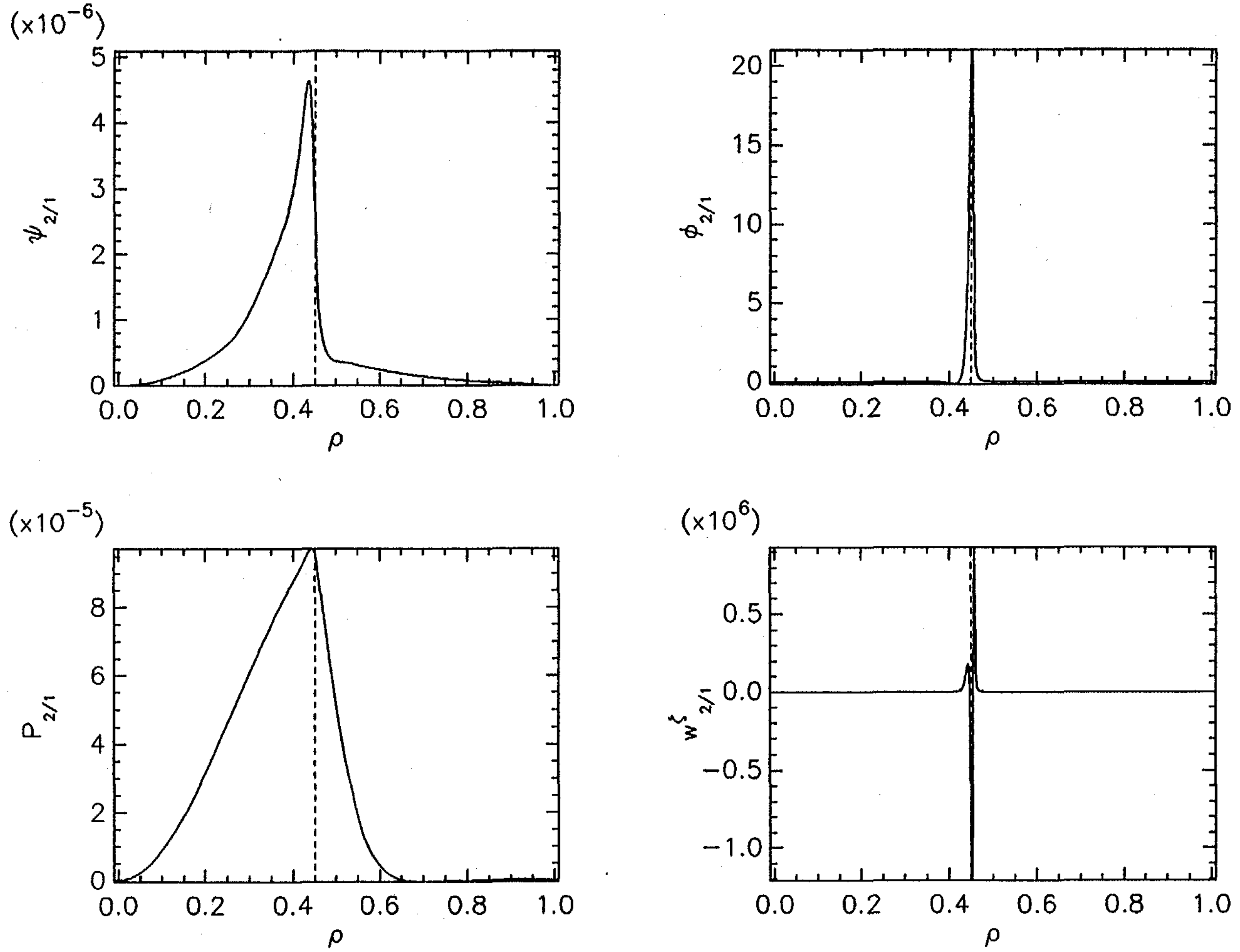

Figure 3.13: Eigenfunctions for the 2/1 mode in the saturation regime for equilibrium A.1.

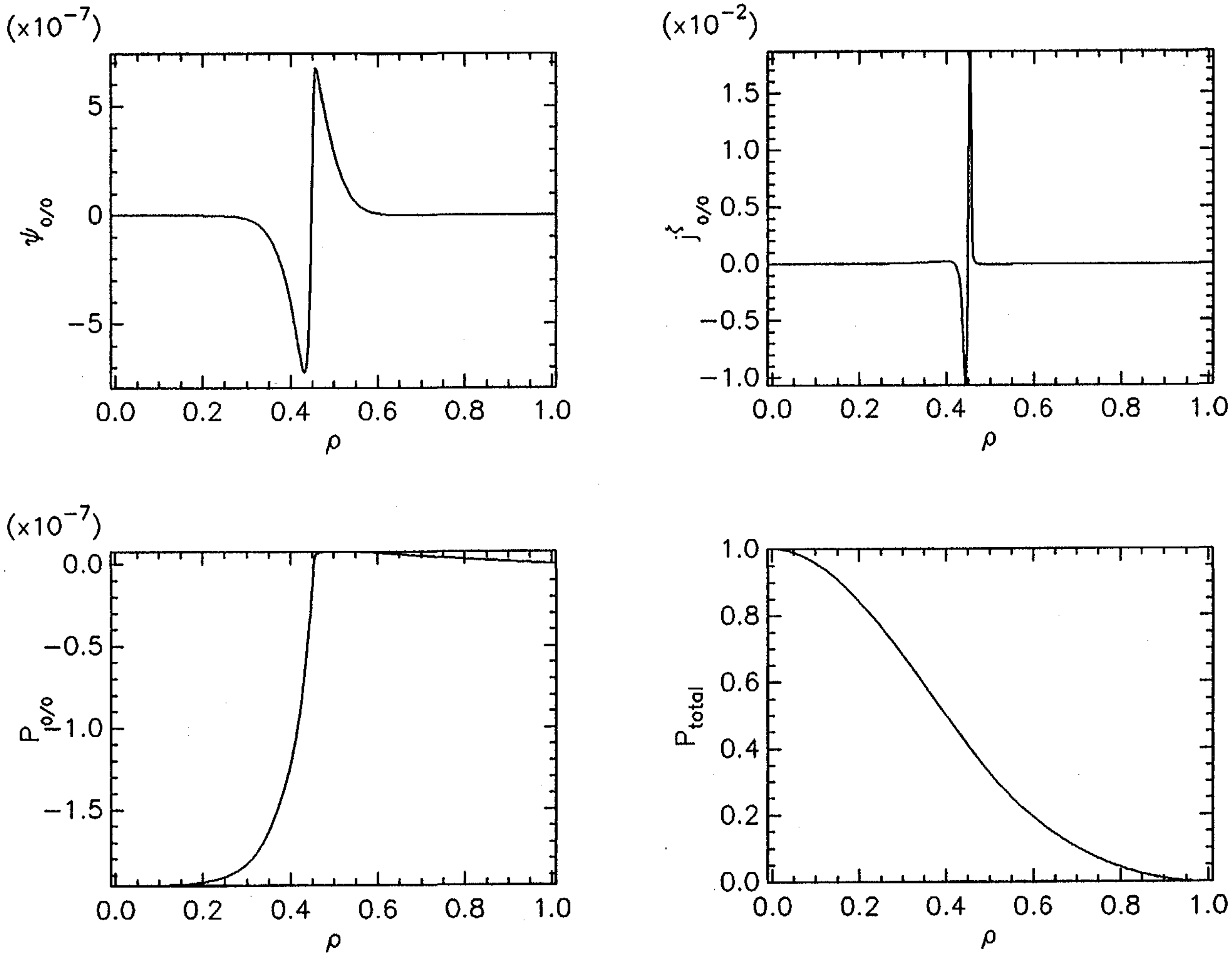

Figure 3.14: Eigenfunctions for the 0/0 mode in the saturation regime for equilibrium A.1.

3.2.2 Dynamics of toroidal tearing mode

While the single helicity magnetic island provides an important check of the numerical simulation, in a real tokamak the toroidal geometry produces coupling between Fourier harmonics with the same toroidal mode number—coupling which can lead to a ballooning/twisting/tearing plethora of modes [44]. Hence, in the previous section the unstable 2/1 mode would also generate 3/1, 4/1, and 5/1 modes at their respective surfaces, in addition to the remaining non-resonant $n = 1$ harmonics. The coupling results of this section should be interpreted lightly since this model does not include differential plasma rotation, which might mask the effects of the poloidal mode coupling in a real tokamak plasma [45, 29]. Nonetheless, the simulations will be a useful benchmark. This subsection will be completed with the description of a mode, which is robustly unstable at high β and exhibits no nonlinear saturation. The mode has been included as a matter of completeness, but the question of a theoretical interpretation is still speculative.

Only a limited set of equilibria have been chosen for the numerical simulations of this section. The equilibria have the general property that if a numerical simulation were conducted on any of the individual modes as per the previous section (i.e., single helicity with no poloidal coupling) then the observed tearing mode would be Δ' stable. However, such equilibria, as will be demonstrated, do not necessarily insure that an unstable resistive mode structure does not develop.

The basic phenomenology of the time evolution of a coupled set of 2/1, 3/1, and 4/1 modes is illustrated in the dynamics of the 2/1 mode as illustrated in Figures 3.15 and 3.16 for equilibrium A.1 which is detailed in Appendix A. Many of the features which describe single helicity unstable modes also appear to describe this mode. An initial linear growth regime, where the mode width increases exponentially in time exists. As the island width increases beyond the resistive layer $w \sim \delta_R$, a Rutherford regime appears to exist. Finally, the nonlinear generation of an $m = 0/n = 0$ current flattens the current gradient in the vicinity of the 2/1 island, and apparently eliminates the drive mechanism for the island. Throughout the simulations the 2/1, 3/1, and 4/1 modes each grow at nearly the same rate in both the linear and the nonlinear regimes, as illustrated in Figure 3.17. Furthermore, the mode shapes also remain nearly the same throughout the simulations, which provides credence to the idea that the external region solutions are basically described by ideal MHD and are unaffected by either the linear or nonlinear layer physics. In these simulations the $m = 1/n = 1$ mode has been neglected, because it does not have a resonant surface within the plasma and also the coupling to this mode can be large [10] which makes later benchmark comparisons difficult.

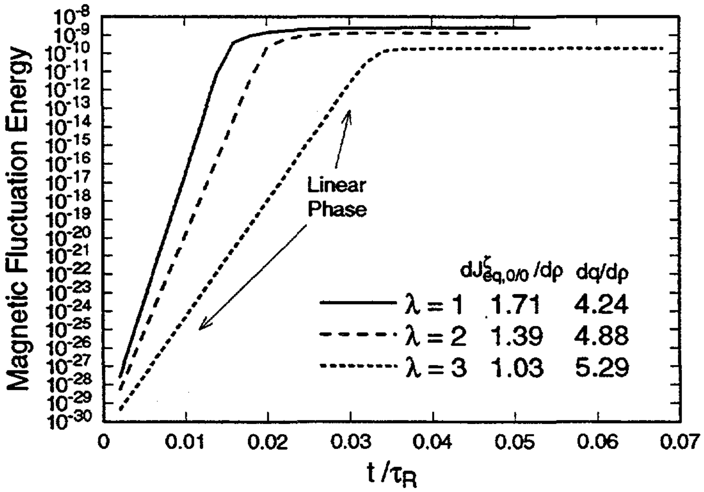

Figure 3.15: The $m = 2/n = 1$ magnetic island coupled to the $m = 3/n = 1$ and the $m = 4/n = 1$ modes grows exponentially in time when the island is small. The three curves share the common parameters of $S = 5\,(10^6)$, $\chi_\perp = 10$, and $\chi_{||} = 10^6$. Neoclassical viscous effects are neglected and the conventional viscosity coefficient is $\mu = 10^{-5}$. The figure is also indicative of the current gradient dependency of the mode.

Another interesting feature is that the S scaling appears to be consistent with the growth rate indicated by Eq. (3.6) for the standard Δ' tearing mode. Figure 3.18 illustrates that the observed asymptotic scaling is almost the expected $S^{2/5}$ for each of the three current profiles even when the coupling to the 3/1 and 4/1 modes are included. Figure 3.18 also shows that these modes are current gradient driven since the pressure profile is the same in these simulations.

Figures 3.19 to 3.22 illustrate typical eigenfunctions in the linear regime for each of the harmonics. The 2/1 mode is qualitatively similar to the single helicity 2/1 mode of the previous subsection: 1) ψ has an r^m behavior near the magnetic axis and an r^{-m} behavior near the conducting wall boundary for the $m \neq 0/n \neq 0$ modes; 2) ϕ is localized about the mode rational surface and is odd about this surface; 3) ϕ is approximately a factor of S larger in amplitude than ψ; and 4) The pressure equilibrates along the magnetic flux surfaces. However, the 3/1 and 4/1 modes exhibit different behaviors. First, the coupling to the 2/1 mode tends to make these modes peaked about the 2/1 resonant surface. This coupling will be discussed in the next paragraph based on approximate estimates derived from E-matrix theory [8, 37].

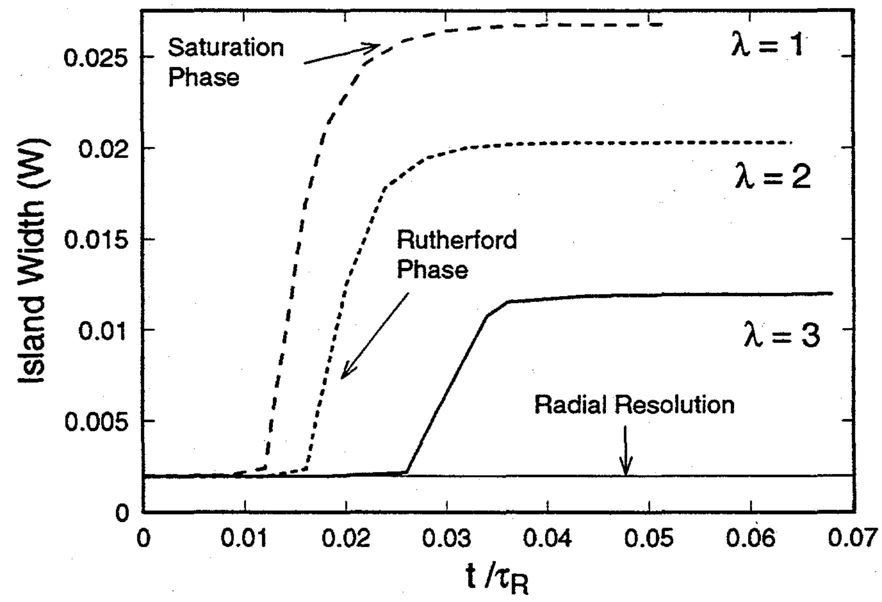

Figure 3.16: Prior to mode saturation, the $m = 2/n = 1$ magnetic island width grows linearly in time. The three curves share the common parameters of $S = 5(10^6)$, $\chi_\perp = 10$, and $\chi_{||} = 10^6$. Neoclassical viscous effects are neglected and the conventional viscosity coefficient is $\mu = 10^{-5}$. As λ decreases the equilibrium current gradient steepens at the mode rational surface which further destabilizes the mode. The island width cannot be computed for island widths smaller than the radial mesh size.

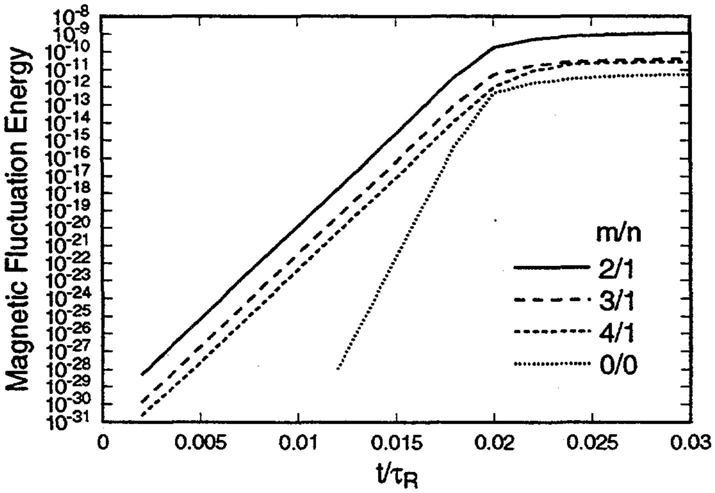

Figure 3.17: The $m = 2/n = 1$, $m = 3/n = 1$ and $m = 4/n = 1$ modes grow at the same rate. The three curves share the common parameters of $S = 5\,(10^6)$, $\chi_\perp = 10$, and $\chi_{||} = 10^6$. Neoclassical viscous effects are neglected and the conventional viscosity coefficient is $\mu = 10^{-5}$. As λ decreases the equilibrium current gradient steepens at the mode rational surface which further destabilizes the mode.

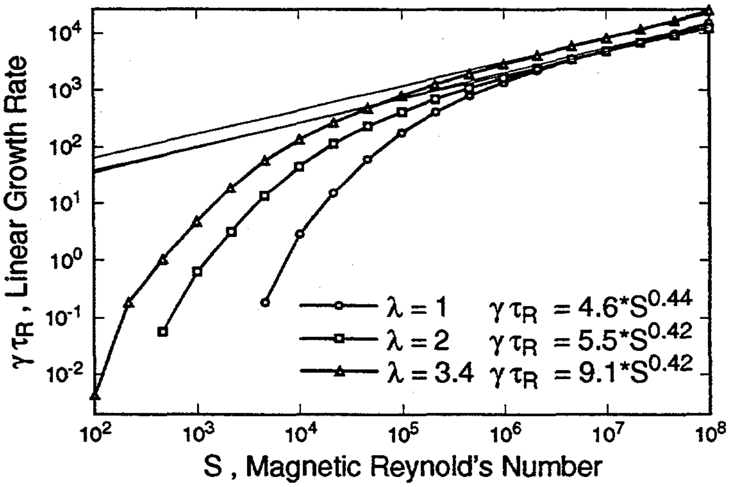

Figure 3.18: At large magnetic Reynold's number S, the linear growth rate of the 2/1 tearing mode asymptotes to S^α, where $\alpha \simeq 0.44$. The simulations include the 3/1 and 4/1 modes.

Also, Figures 3.20 and 3.21 illustrate the presence of poloidal mode coupling. The poloidal mode coupling as implemented in this code assumes a phase which produces the maximum coupling between modes. In a real tokamak plasma, differential plasma rotation would be expected to reduce and possibly eliminate this mode coupling. Several observations can be made about the mode coupling and interpreted based on E-matrix theory [8, 37], an asymptotic theory for the ideal external problem which is an MHD generalization to toroidal geometry of the cylindrical Δ' analysis with ϵ and $\epsilon\beta_p$ as expansion parameters. (Here, β_p is the poloidal β.) The E-matrix theory finds that for plasmas with weak shaping the only important coupling for a tearing mode of helicity m/n are the $(m-1)/n$ and $(m+1)/n$ harmonics. A more complete coupling theory which allows for coupling of tearing modes with ballooning modes has been done by Fitzpatrick [8]. However, even with this more complicated model, the coupling coefficients are roughly the same for either type of mode so the coupling can still be qualitatively discussed with tearing E-matrix theory. In this simple case, the E-matrix coupled with the layer physics is represented as

$$\begin{bmatrix} E_{11} & E_{12} & 0 \\ E_{21} & E_{22} & E_{23} \\ 0 & E_{32} & E_{33} \end{bmatrix} \begin{vmatrix} \psi_{2/1}(\rho_{2/1}) \\ \psi_{3/1}(\rho_{3/1}) \\ \psi_{4/1}(\rho_{4/1}) \end{vmatrix} = \begin{vmatrix} \Delta_{2/1}(\gamma)\psi_{2/1}(\rho_{2/1}) \\ \Delta_{3/1}(\gamma)\psi_{3/1}(\rho_{3/1}) \\ \Delta_{4/1}(\gamma)\psi_{4/1}(\rho_{4/1}) \end{vmatrix}, \tag{3.10}$$

where the Δ's contain the layer physics as a function of the growth rate γ, the E_{ij}'s are constants which have the general property that off-diagonal elements are order ϵ smaller than the diagonal elements, and $\rho_{2/1}$, $\rho_{3/1}$, and $\rho_{4/1}$ indicate that ψ is to be evaluated at the respective mode surface. With these assumptions, the E-matrix implies that

$$\psi_{3/1} \simeq -\frac{E_{2/1}}{E_{22} - \Delta_{3/1}} \psi_{2/1} \sim \epsilon\psi_{2/1}. \tag{3.11}$$

In a similar manner $\psi_{4/1} \sim \epsilon\psi_{3/1} \sim \epsilon^2\psi_{2/1}$.

To further explore the mode coupling, Figures 3.19 through 3.22 illustrate the eigenfunctions for a time slice during the linear phase for the 2/1, 3/1, 4/1, and 0/0 modes for Equilibrium A.1 at $\beta_0 = 0.006$. In Figure 3.19, the 2/1 mode is tearing in structure as per the previous section and mode the coupling is small. The 3/1 harmonic illustrated in Figure 3.20 is indicative of mode coupling with a strong peaking about the 2/1 rational surface. The second peak is the natural response of the 3/1 mode about its resonant surface. The effect of the 4/1 mode appears to show up only in the vorticity as a small spike. In this case, the ratio $\psi_{3/1}(\rho_{3/1})/\psi_{2/1}(\rho_{2/1}) = 0.08$, which is $O(\epsilon)$. The 4/1 mode illustrated in Figure 3.21 is similar to the 3/1. A peak is observed about the 2/1 resonant surface, which is probably not due to direct coupling with the 2/1 mode $[O(\epsilon^2)]$, but rather to the large magnitude of the 3/1 mode at this surface and then the resultant coupling. For this harmonic, the natural response is much larger in amplitude though narrower in width than the nonlinear coupling contribution. In this case, the ratio $\psi_{4/1}(\rho_{4/1})/\psi_{3/1}(\rho_{3/1}) = 0.53$, which is also $O(\epsilon)$.

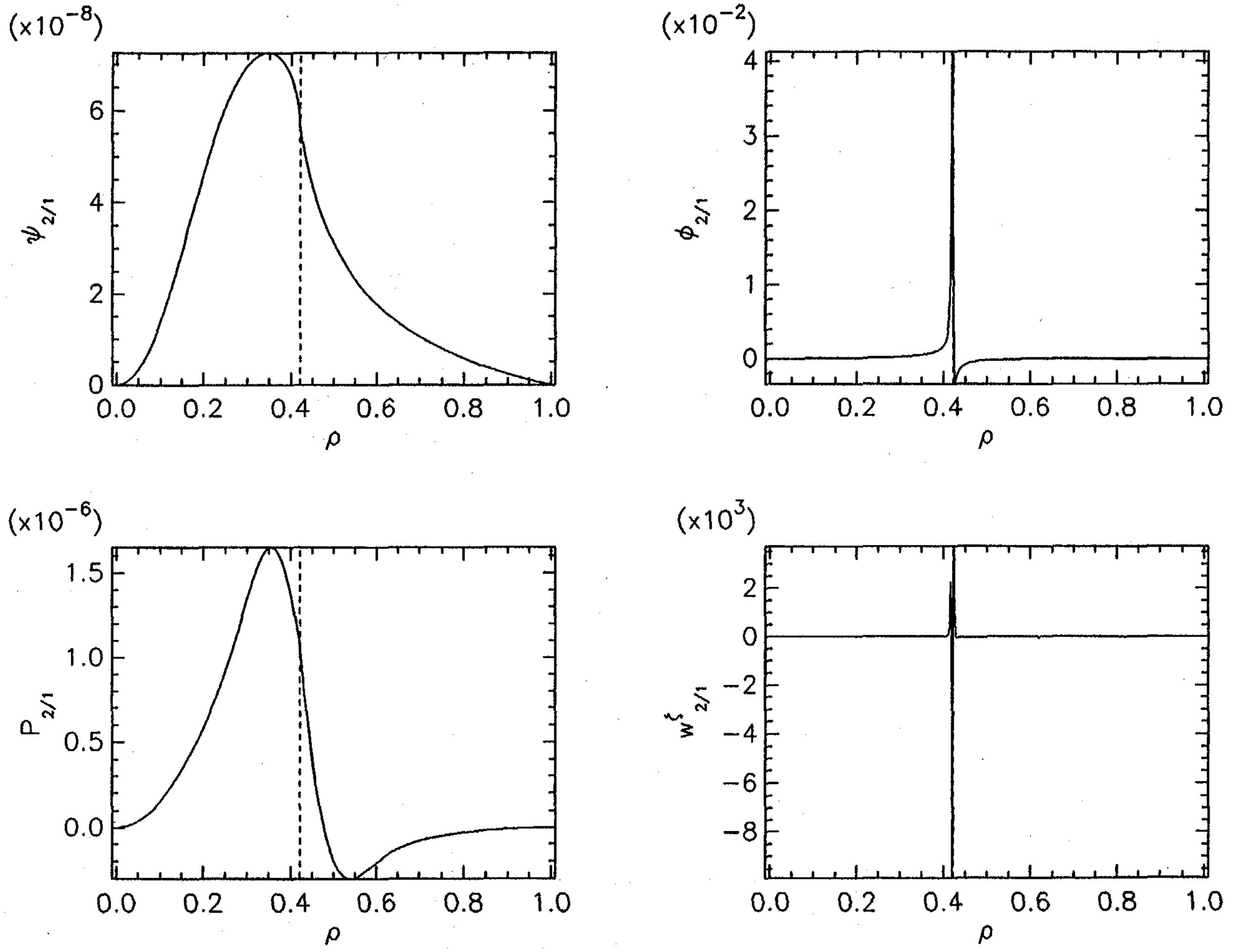

Figure 3.19: Eigenfunctions for the 2/1 mode in the linear regime for equilibrium A.1 and $\beta_0 = 0.006$ illustrate a tearing structure at the $q = 2/1$ rational surface, which is marked by the dashed vertical line.

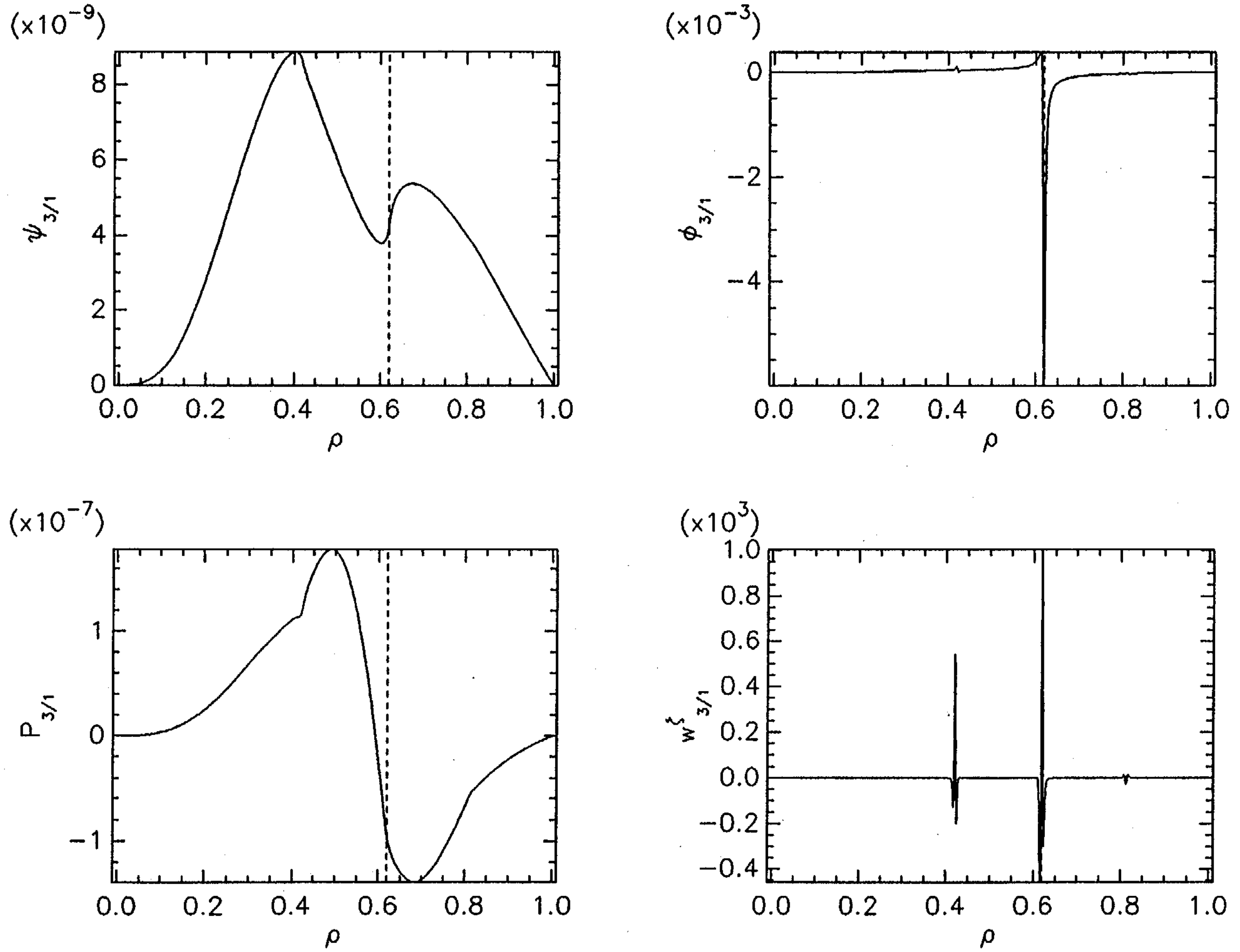

Figure 3.20: Eigenfunctions for the 3/1 mode in the linear regime for equilibrium A.1 and $\beta_0 = 0.006$ illustrate two peaks and a valley. The largest peak corresponds to the poloidal mode coupling with the 2/1 perturbation. The other peak corresponds to the natural response of the $m/n = 3/1$ mode. The valley occurs when the contributions from these two components are combined.

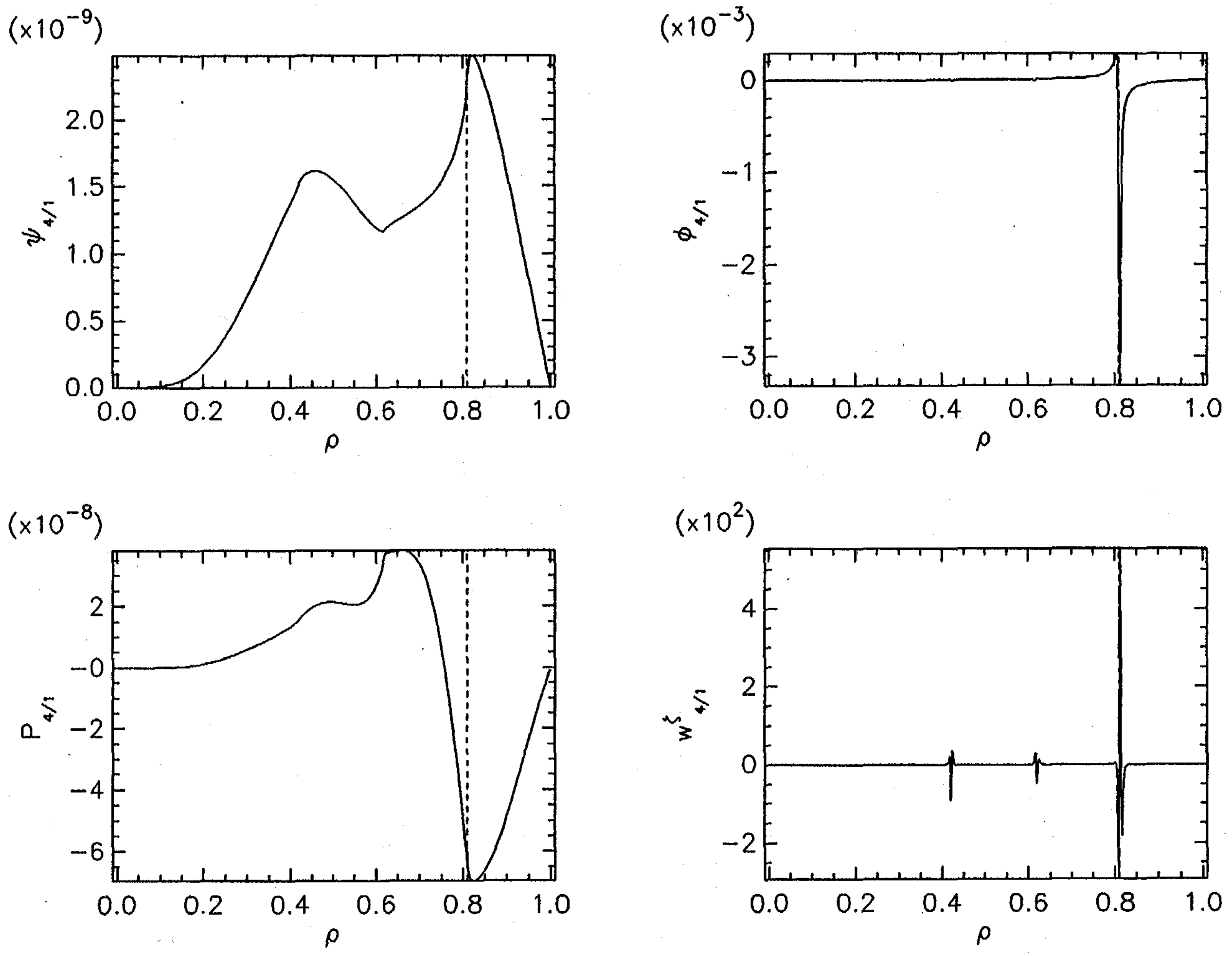

Figure 3.21: Eigenfunctions for the 4/1 mode in the linear regime for equilibrium A.1 and $\beta_0 = 0.006$ illustrate two peaks and a valley. The largest peak corresponds to the poloidal mode coupling with the 3/1 perturbation, which is largest at the 2/1 surface do poloidal mode coupling with the 3/1. The other peak is the natural response of the $m/n = 4/1$ mode.

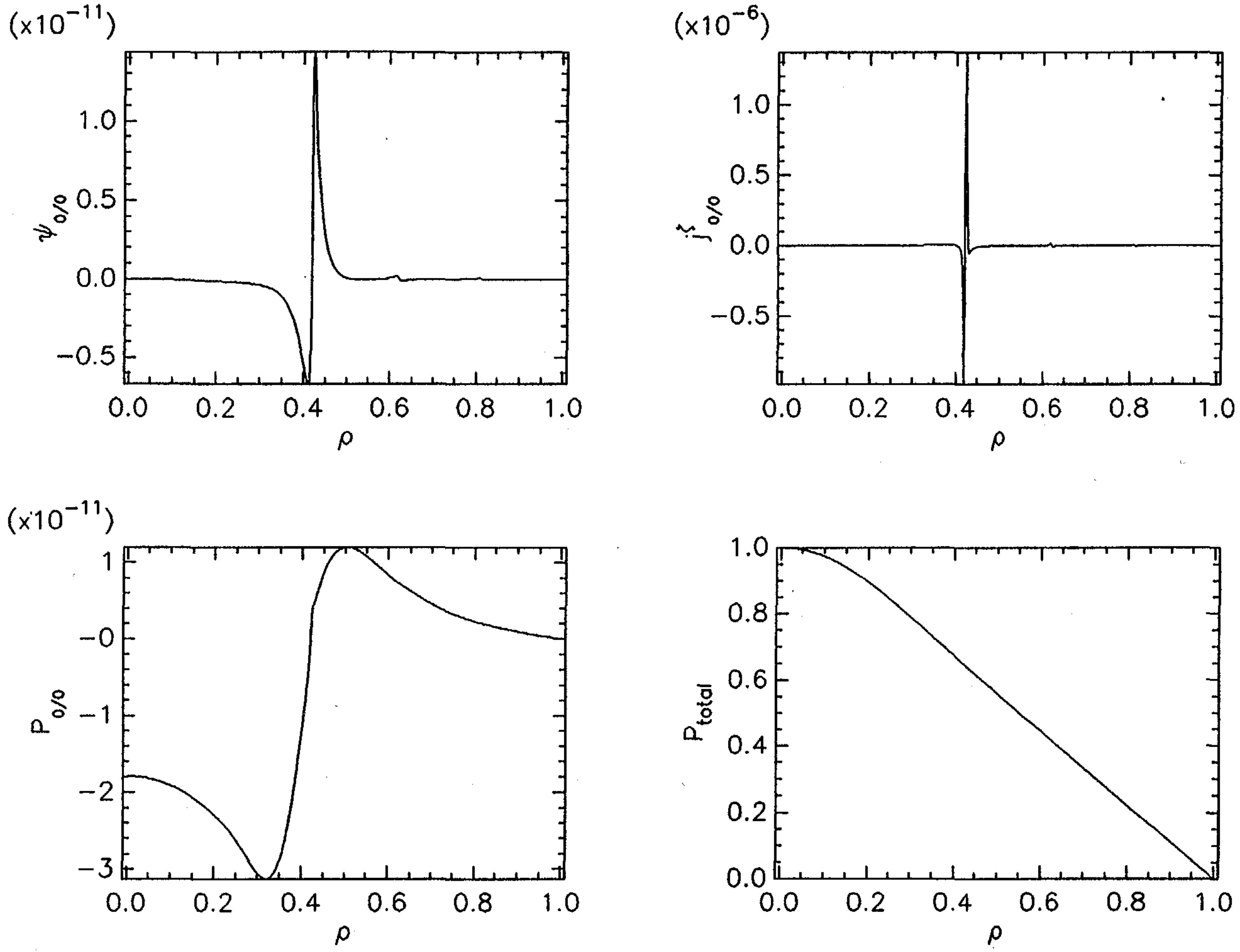

Figure 3.22: Eigenfunctions for the 0/0 mode in the linear regime for equilibrium A.1 and $\beta_0 = 0.006$. Only the nonlinear interaction of the 2/1 mode drives the 0/0 mode in the linear growth regime. The 0/0 component of the pressure lags the island evolution as evidenced by the lack of a flat profile near the magnetic axis.

As the island width becomes sufficiently large, the mode changes from an exponential growth rate to a growth rate proportional to time, which will be labeled as the "Rutherford" regime. Except for minor differences, the nonlinear mode coupling in this regime remains almost the same as the previous linear regime. First, as illustrated in Figure 3.23, except for an increase in the mode amplitude, the 2/1 eigenfunctions are essentially unchanged from the linear regime. However, both the 3/1 and 4/1 eigenfunctions, as illustrated in Figures 3.24 and 3.25, respectively, exhibit an increase in their magnitude relative to their magnitude at the $q = 2/1$ resonant surface. This difference is driven by a decrease in the mode stability brought about by a steepening of the current profile about the 3/1 and 4/1 surfaces as evidenced in Figure 3.26. This introduces a rather interesting question, which will not be addressed in this thesis, but could be addressed by the numerical model: Can the quasilinear stability of the 2/1 mode destabilize the 3/1 mode due to current steepening at the 3/1 resonant surface caused by the nonlinear coupling of the 2/1 mode?

Finally, the 0/0 component of the pressure continues to lag the island evolution, as evidenced by the lack of a flat pressure profile near the magnetic axis in the perturbative component. As will be explained in the next subsection, the choice of $\chi_\perp = 10$ is insufficient to produce rapid equilibration of the cross-field pressure profile. Note that the pressure perturbation is not large enough in this case to produce a strong flattening of the total pressure profile across the resonant surface.

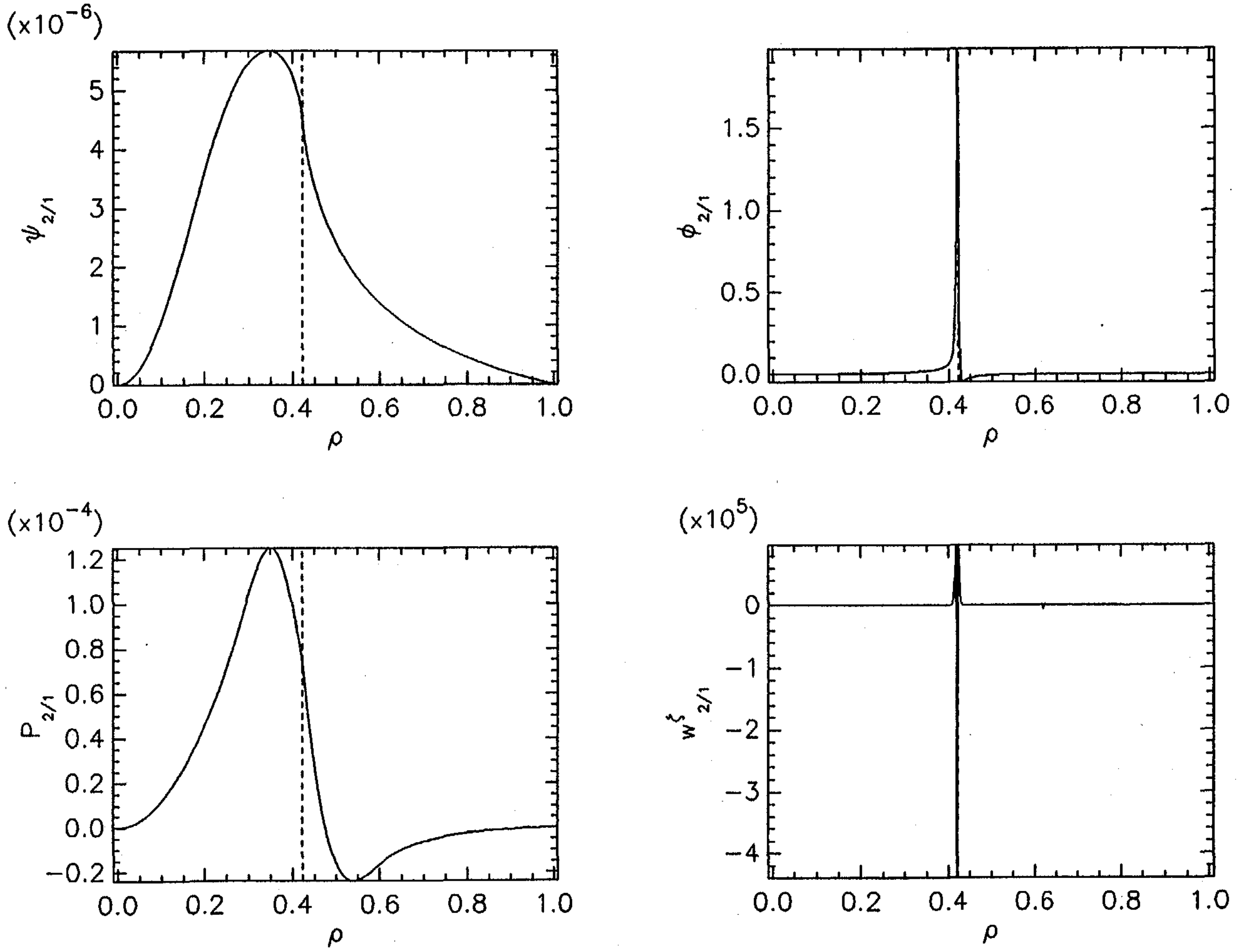

Figure 3.23: Eigenfunctions for the 2/1 mode in the Rutherford regime for equilibrium A.1 and β_0 = 0.006 illustrate a tearing structure at the $q = 2/1$ rational surface. The $q = 2/1$ rational surface is marked by the dashed vertical line.

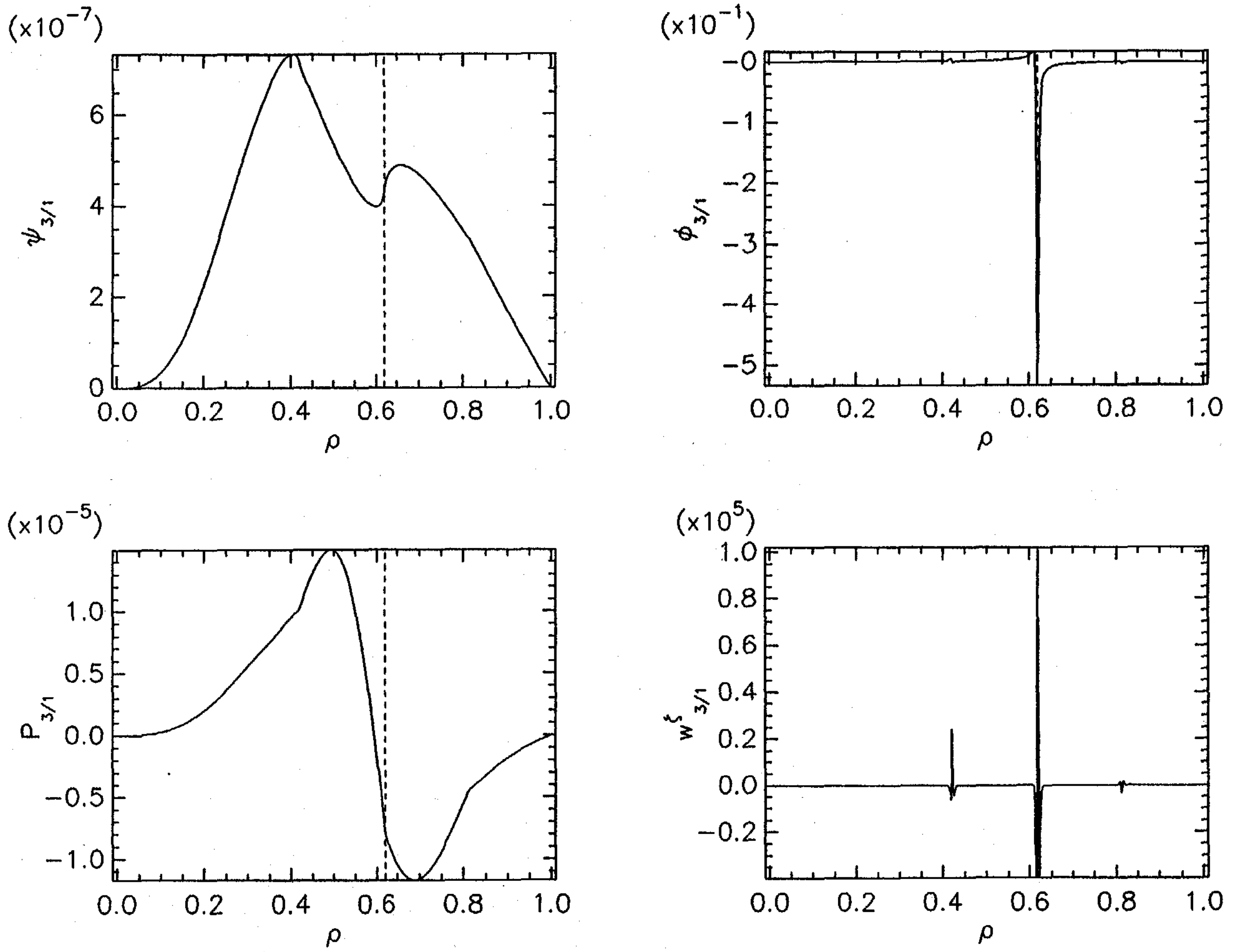

Figure 3.24: Eigenfunctions for the 3/1 mode in the Rutherford regime for equilibrium A.1 and $\beta_0 = 0.006$. In comparison with the linear regime, an increase in the magnitude of the 3/1 eigenfunction relative to the magnitude at the $q = 2/1$ surface is observed. The largest peak corresponds to the poloidal mode coupling with the 2/1 perturbation. The other peak corresponds to the natural response of the $m/n = 3/1$ mode.

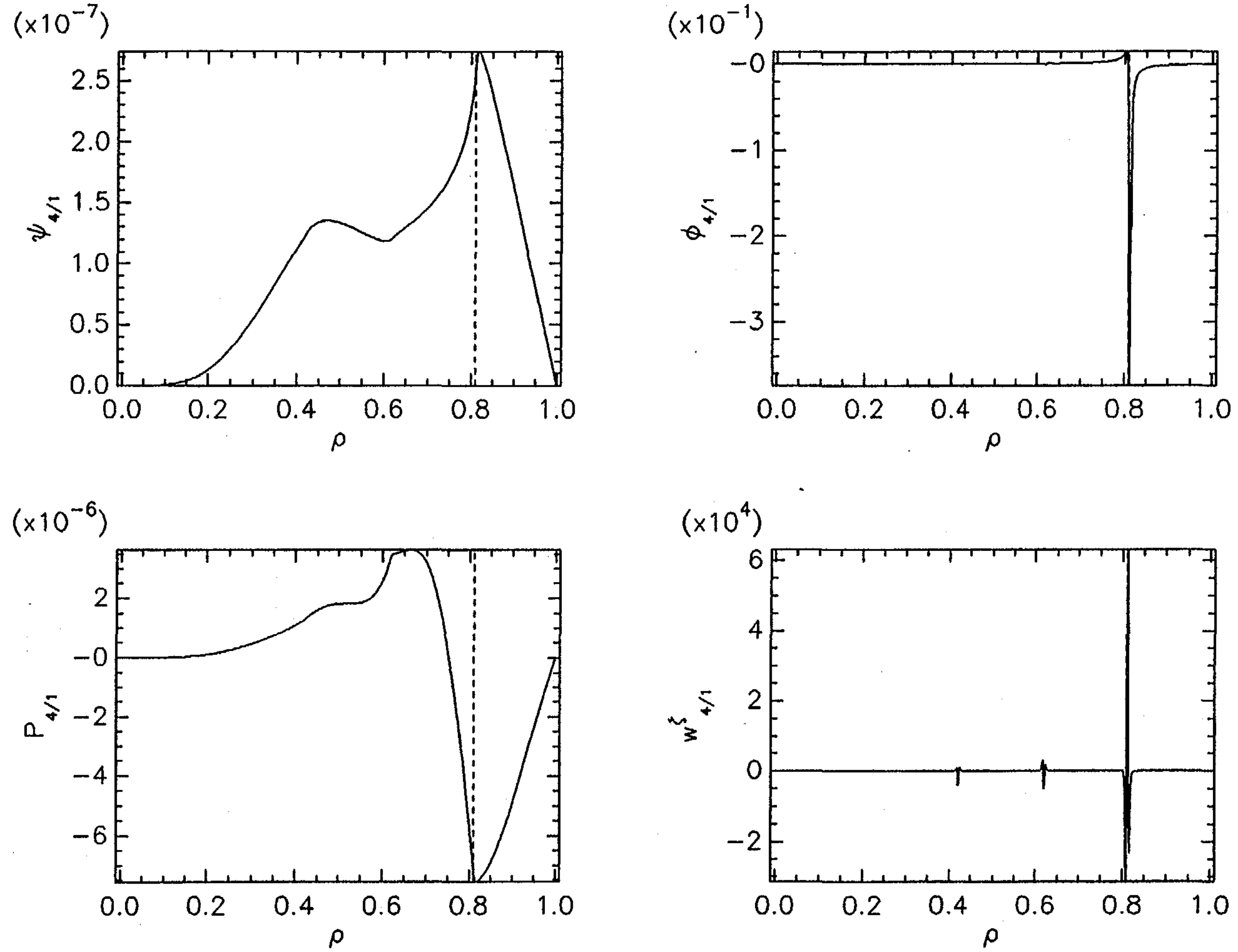

Figure 3.25: Eigenfunctions for the 4/1 mode in the Rutherford regime for equilibrium A.1 and $\beta_0 = 0.006$. In comparison with the linear regime, an increase in the magnitude of the 4/1 eigenfunction relative to the magnitude at the $q = 2/1$ surface is observed. The largest peak corresponds to the poloidal mode coupling with the 3/1 perturbation. The other peak corresponds to the natural response of the $m/n = 4/1$ mode.

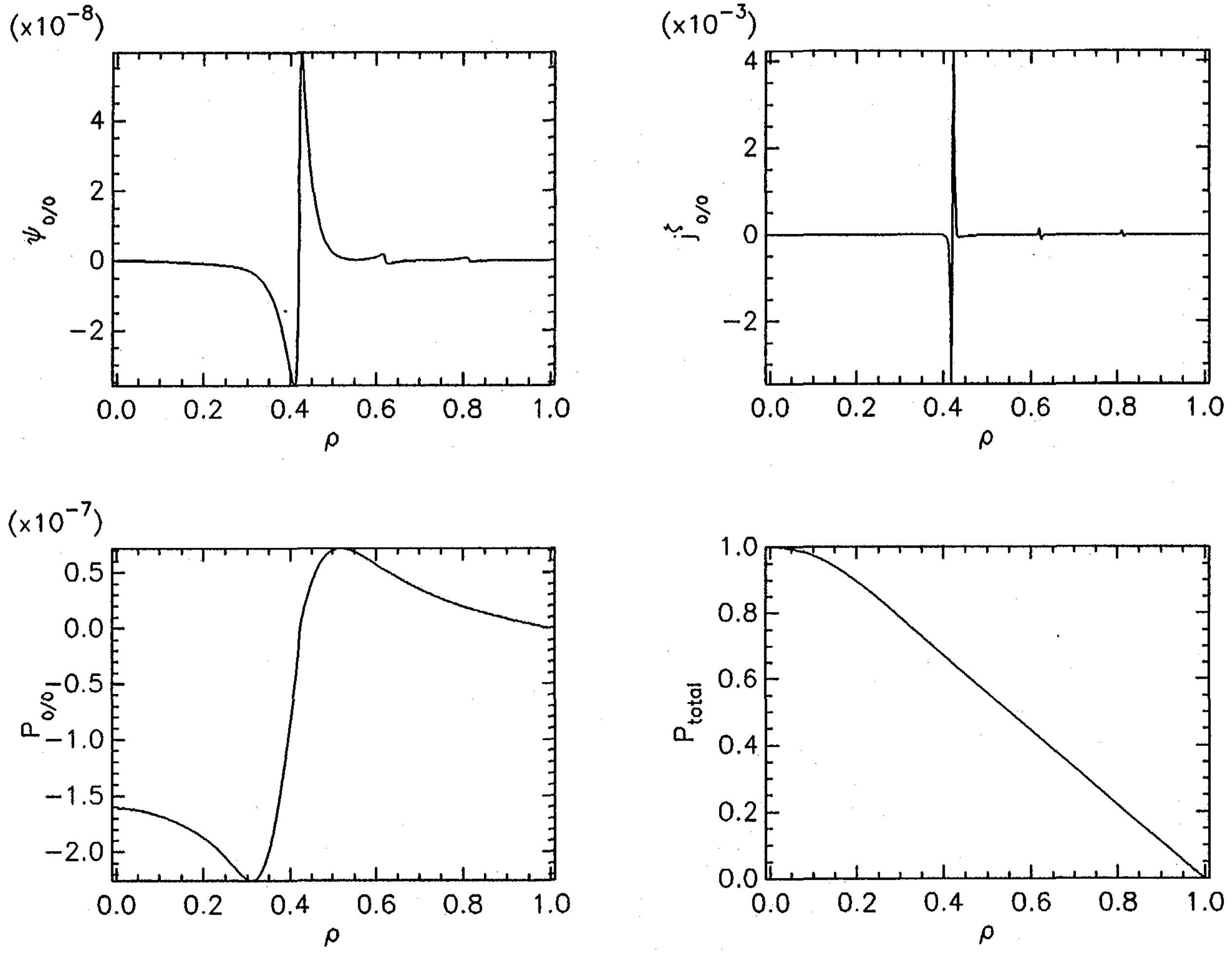

Figure 3.26: Eigenfunctions for the 0/0 mode in the Rutherford regime for equilibrium A.1 and $\beta_0 = 0.006$. The nonlinear interaction of the 2/1 mode principally drives the 0/0 mode in this regime. The 0/0 component of the pressure continues to lag island evolution as evidenced by the lack of a flat profile near the magnetic axis.

In the saturation phase ($\gamma\tau_R \rightarrow 0$), the mode eventually generates an equilibrium current sufficient to flatten the current profile about the 2/1 surface [36]. This current flattening eliminates the current gradient drive mechanism for the island and the mode saturates. First, as illustrated in Figure 3.27, except for an increase in the mode amplitude, the 2/1 eigenfunctions are essentially unchanged from the Rutherford regime. The nonlinear mode coupling in the saturation regime remains almost the same except for further increases in the magnitude of the 3/1 and 4/1 eigenfunctions relative to their magnitude at the $q = 2$ resonant surface (see Figures 3.28 and 3.29). As with the Rutherford regime, but to a greater extent, the 0/0 current gradient is steepened about the 3/1 and 4/1 surfaces as evidenced by Figure 3.30, but not yet enough to destabilize a tearing mode at either surface.

Another interesting feature is that ϕ changes from an odd function about the resonant rational surface in the linear regime to an even function in the saturation phase. From the previous analysis of the single helicity mode in the Rutherford regime, the change can be attributed to the decreasing role of the inertia in these regimes and the increasing generation of nonlinear eddy currents.

Finally, the perturbed $p_{0/0}$ is reduced near the magnetic axis ($\rho = 0$), which is a reflection of fast parallel transport around the magnetic island. However, this pressure perturbation is insufficient to flatten the total pressure profile. Details of the pressure evolution dynamics are discussed in the next subsection.

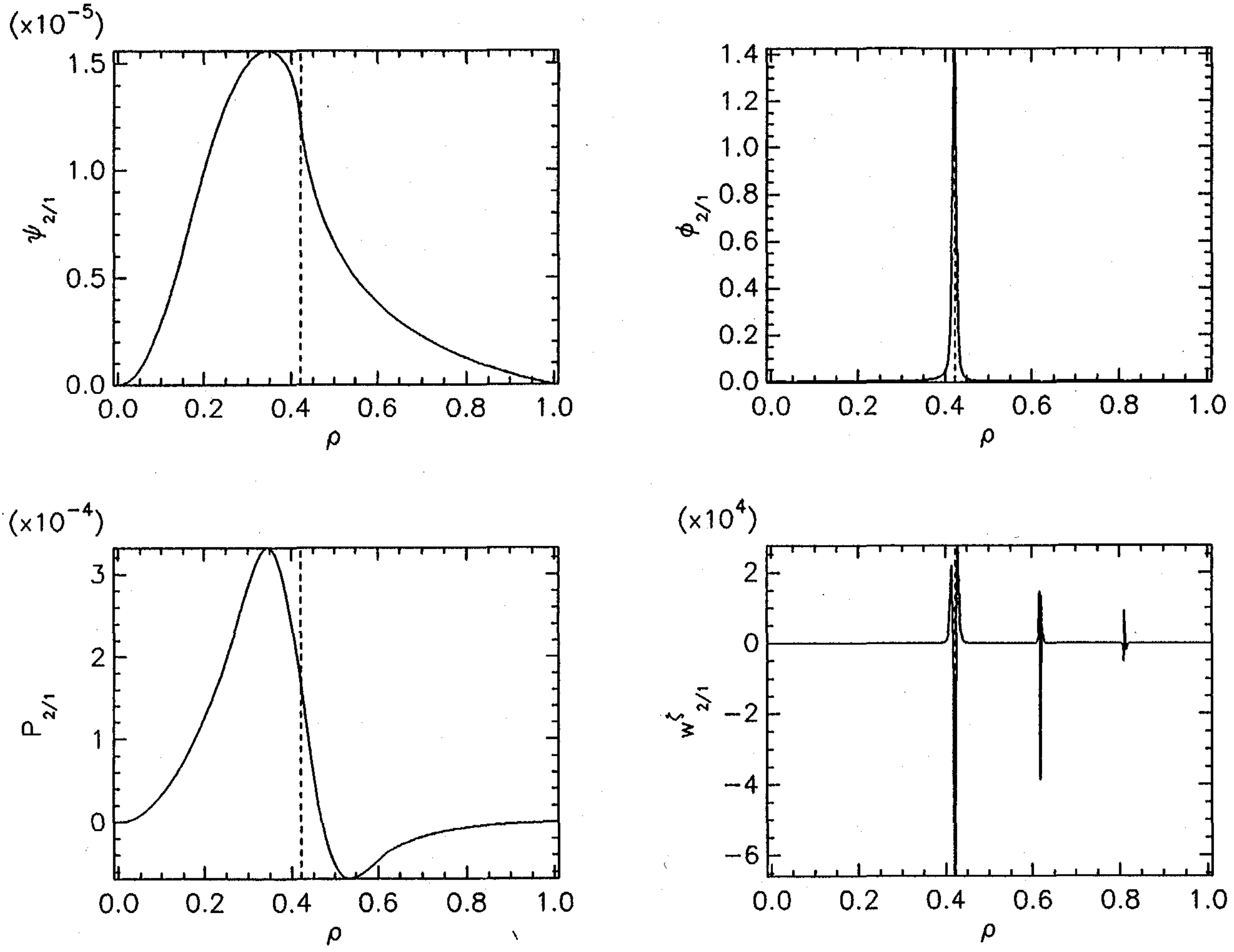

Figure 3.27: Eigenfunctions for the 2/1 mode in the saturation regime for equilibrium A.1 and $\beta_0 = 0.006$ illustrate a saturated tearing mode at the $q = 2/1$ rational surface. The $q = 2/1$ rational surface is marked by the dashed vertical line.

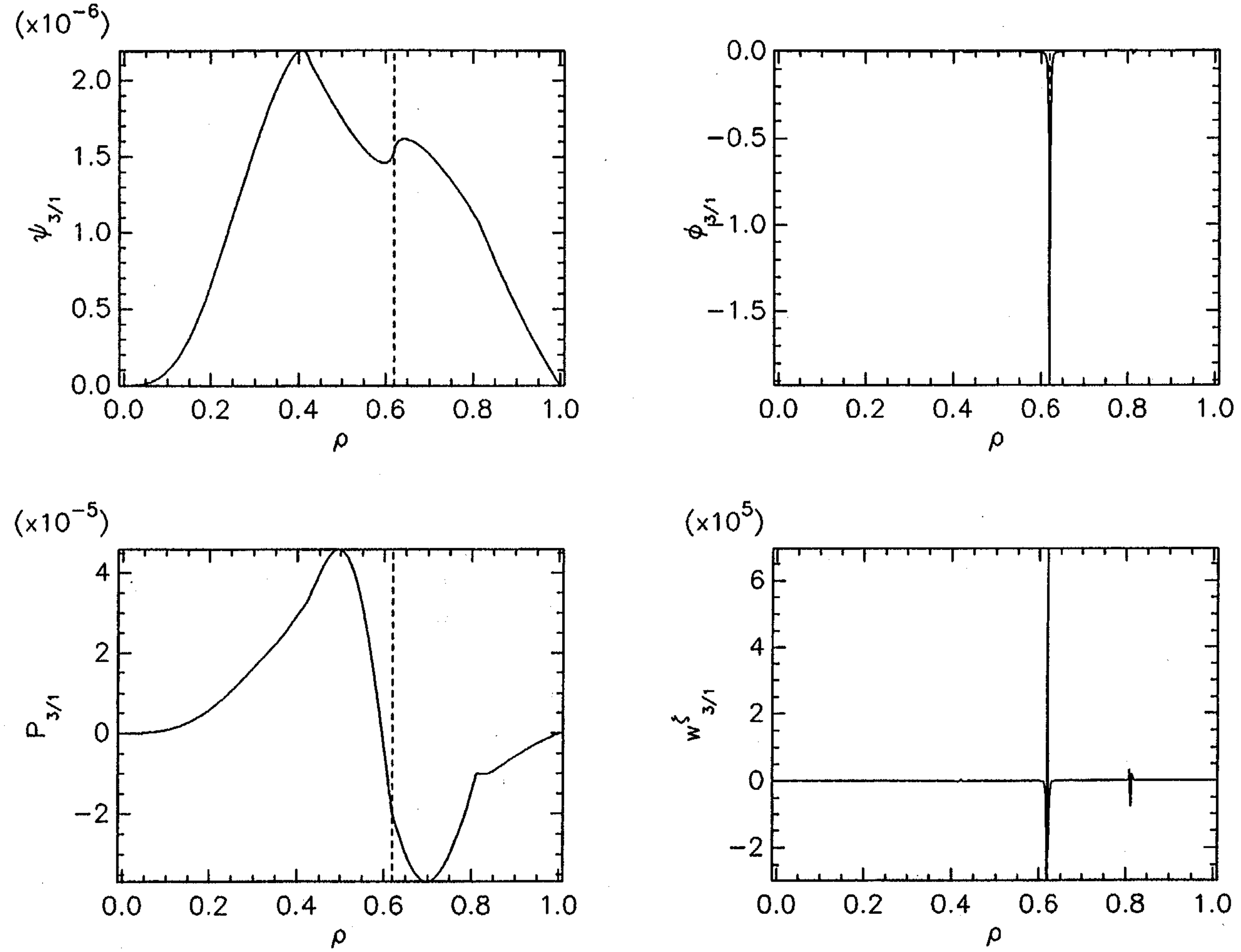

Figure 3.28: Eigenfunctions for the 3/1 mode in the saturation regime for equilibrium A.1 and $\beta_0 = 0.006$. In comparison with the Rutherford regime, an increase in the magnitude of the 3/1 eigenfunction relative to the magnitude at the $q = 2/1$ surface is observed. The largest peak corresponds to the poloidal mode coupling with the 2/1 perturbation. The other peak corresponds to the natural response of the $m/n = 3/1$ mode.

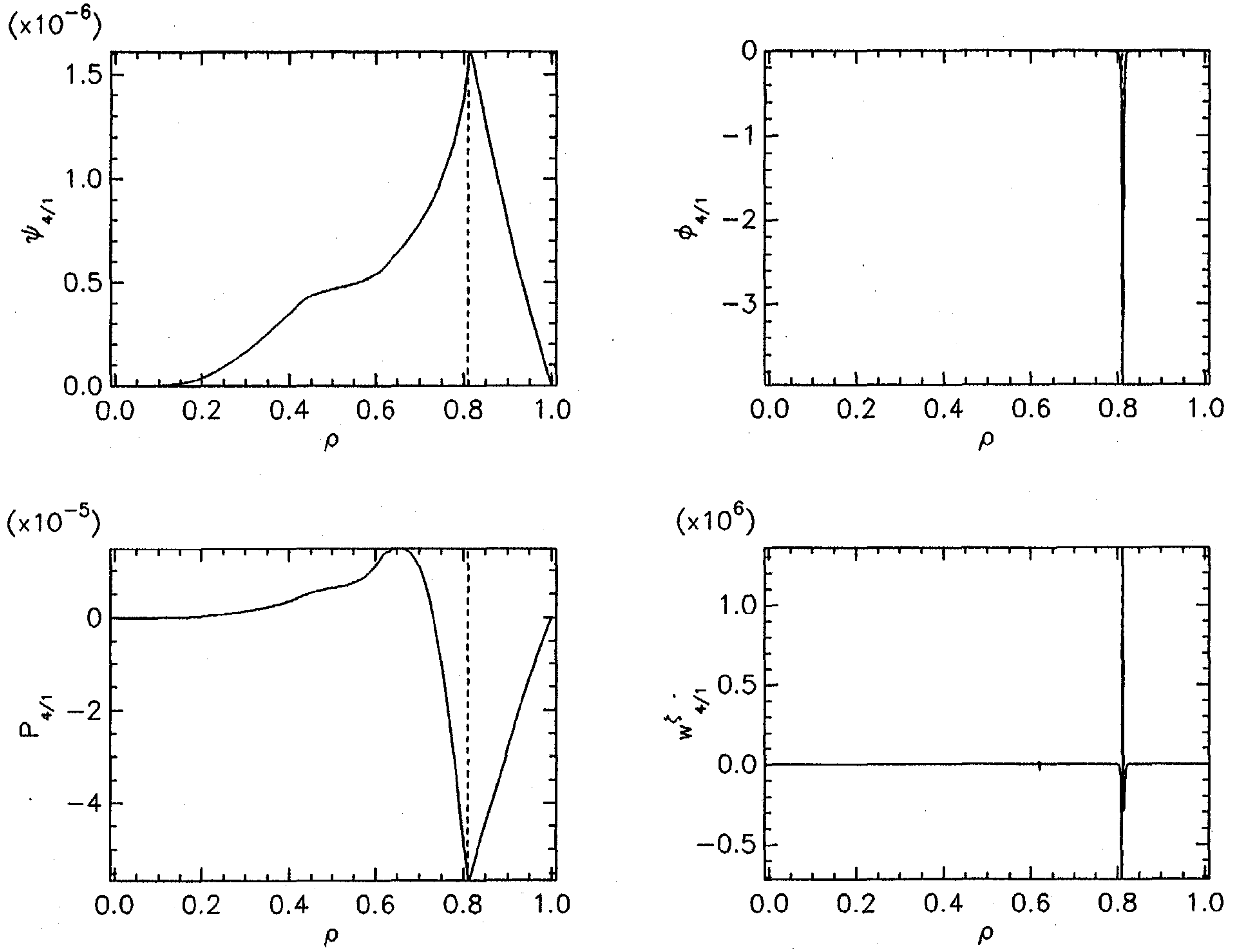

Figure 3.29: Eigenfunctions for the 4/1 mode in the saturation regime for equilibrium A.1 and $\beta_0 = 0.006$. In comparison with the Rutherford regime, an increase in the magnitude of the 4/1 eigenfunction relative to the magnitude at the $q = 2/1$ surface is observed. The largest peak corresponds to the poloidal mode coupling with the 3/1 perturbation. The other peak corresponds to the natural response of the $m/n = 4/1$ mode.

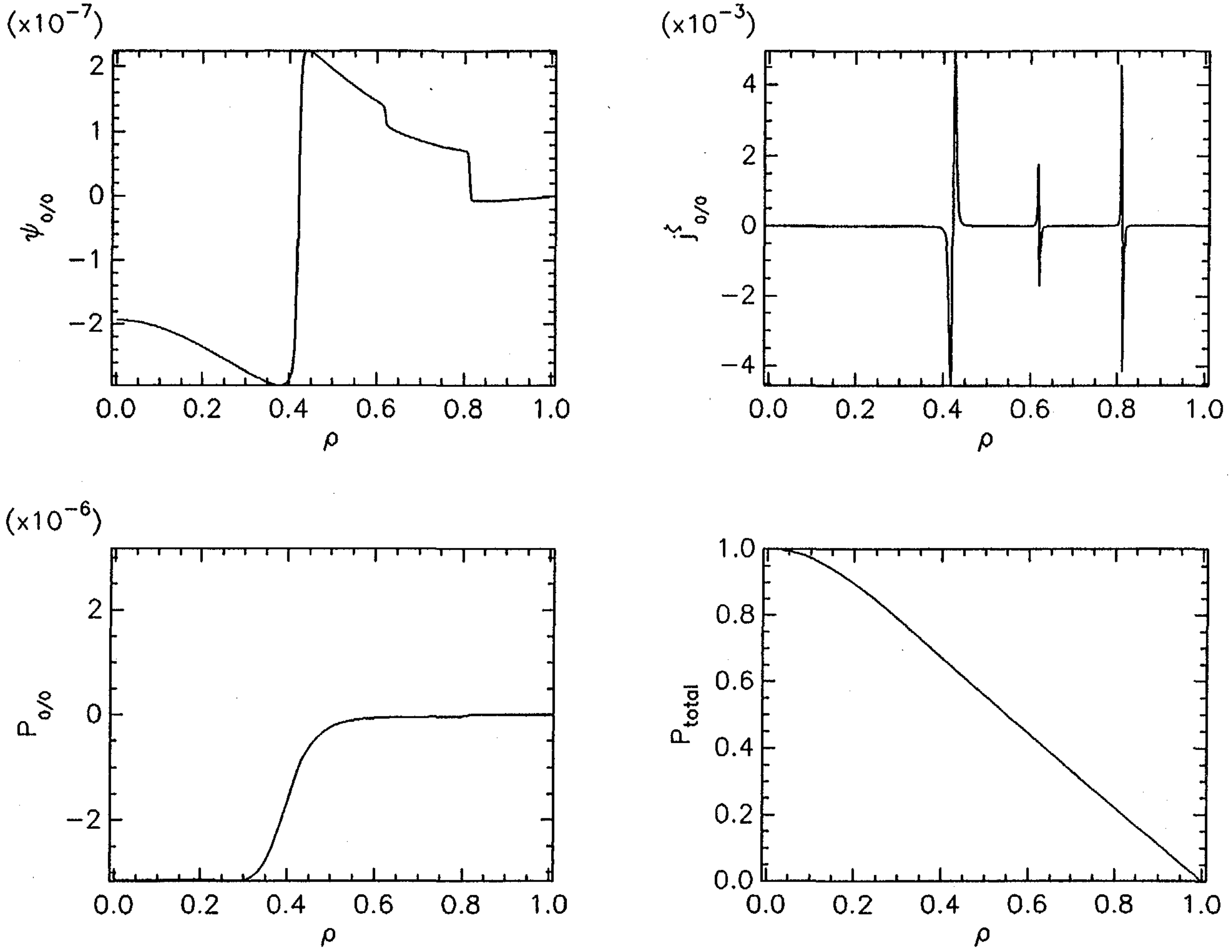

Figure 3.30: Eigenfunctions for the 0/0 mode in the saturation regime for equilibrium A.1 and $\beta_0 = 0.006$. The nonlinear interaction of the 2/1 mode principally drives the 0/0 mode in this regime. The 0/0 component of the pressure reflects fast transport around the magnetic island, which produces a shortcircuit of the perpendicular gradients in the vicinity of the resonant rational surface.

The previous analysis was based on a low β scenario. As the peak plasma pressure indicated by β_0 is increased, the mode dynamics undergo a change in character. At modest values of β_0, the 2/1 mode remains tearing in structure and, similar to the single helicity mode illustrated in Figure 3.31, exhibits a reduced growth rate due to an increase in the pressure.

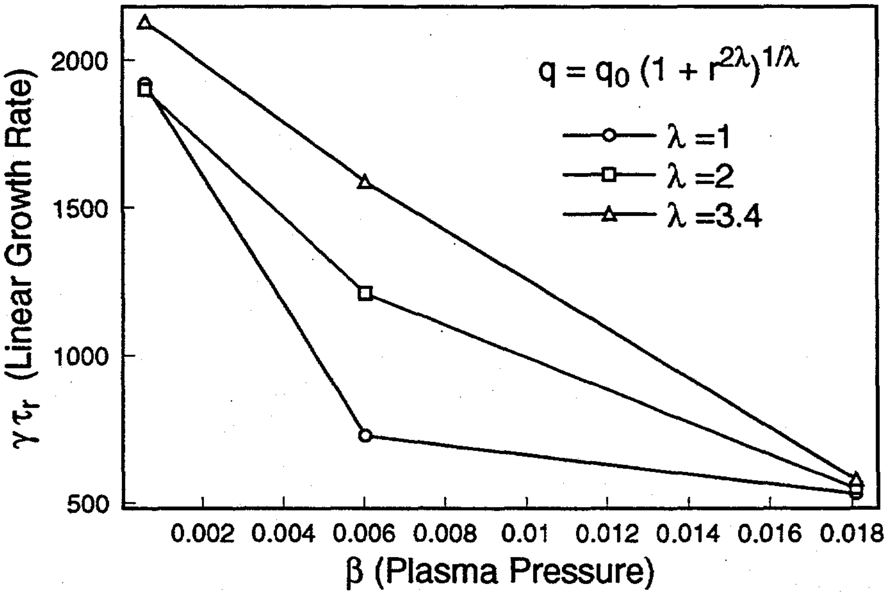

Figure 3.31: Increased β stabilizes the standard tearing mode. The J_1^ρ and J_1^θ currents are low β versions and do not include the pressure curvature piece.

However, as β_0 is increased, the dynamics of the island evolution dramatically changes (see Figure 3.32). The principal change appears to be the linear destabilization of an oscillatory mode, $\psi_1 \sim e^{\gamma t} cos(\omega t)$ (see Figure 3.33). (The 2/1, 3/1, and 4/1 coupled mode simulations exhibit a 3/1 mode which slightly lags the 2/1 mode, which slightly lags the 4/1 mode.) The temptation is to label this a twisting/ballooning mode, since a twisting mode is characterized by a ψ which is odd about the mode rational surface (see Figures 3.34, 3.35, and 3.36), but twisting modes have growth rates on the resistive MHD timescale $\gamma\tau_R \sim S^{2/5}$ and these modes have a growth rate approximately 10% of the ideal growth rate. This growth rate would also rule out ideal kink modes which grow on the ideal time scale [12]. Furthermore, the puncture plot of Figure 3.37, indicates that both the 2/1 and 3/1 modes are clearly tearing and not twisting in nature. However, since the instability at the $q = 4/1$ surface couples to the 2/1 and the 3/1 modes the tearing structure at these surfaces is perhaps not

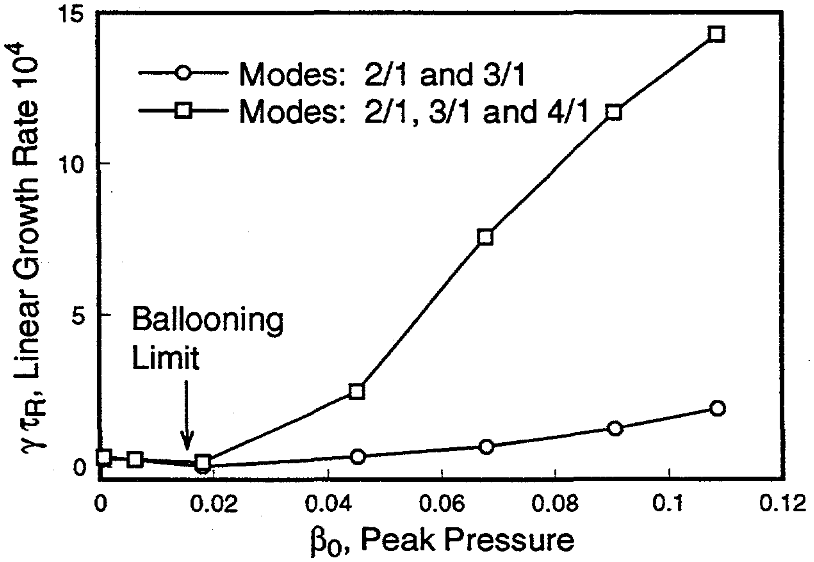

Figure 3.32: Above a threshold $\beta_0 \simeq 0.02$ for equilibrium A.1, a linear destabilization occurs for the highest harmonic in the simulation. The growth rate scales linearly with β_0. The "Modes" are which modes were included in the simulations. The threshold may be a resistive ballooning mode limit.

surprising. Finally, this mode is driven not by the pressure curvature pieces (a.k.a. Glasser terms) but by gradients in the parallel current, because only minimal difference in the mode dynamics is observed when these terms are excluded from the simulations. (Note, that since this is the term which could provide an extraneous source of energy if it does not properly cancel in the energy integral, the lack of a change in the dynamics rules out this possibility.) Also in nonlinear simulations, the mode does not saturate due to a flattening of the equilibrium current profile. If this mode is actually a ballooning/twisting mode variant, and not driven by an unidentified numerical problem, then perhaps plasma compressibility, which this model lacks, might stabilize the mode [30].

The final observation is that Glasser's DCON code [13, 40] makes several predictions about this set of equilibria: 1) the plasma is Mercier stable; 2) the plasma is ideal MHD stable to n=1 modes; and 3) the plasma is unstable to high-n ideal ballooning modes for $\beta_0 > 0.02$. The second and third points suggest that the mode is not an ideal ballooning mode, but leaves open the possibility of resistive ballooning modes.

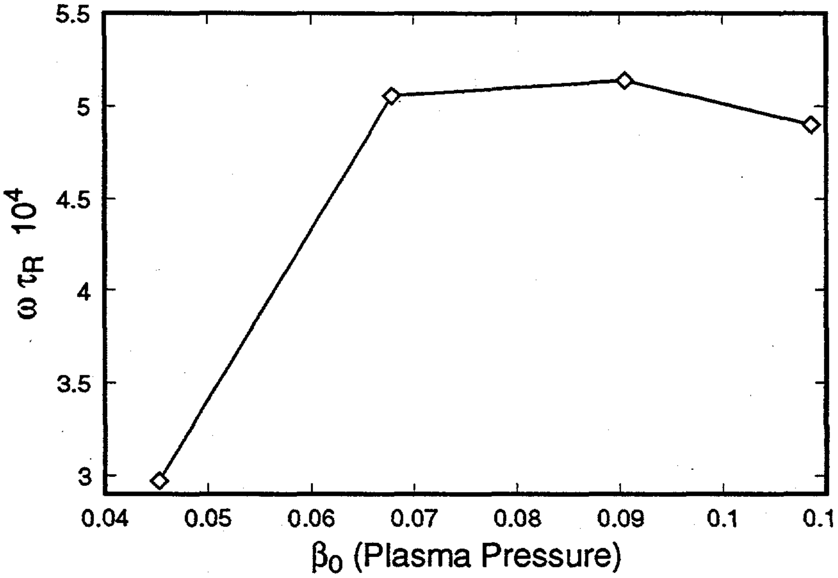

Figure 3.33: Above a threshold $\beta_0 \simeq 0.02$ for equilibrium A.1, the coupled 2/1, 3/1, and 4/1 modes exhibit a real oscillation frequency.

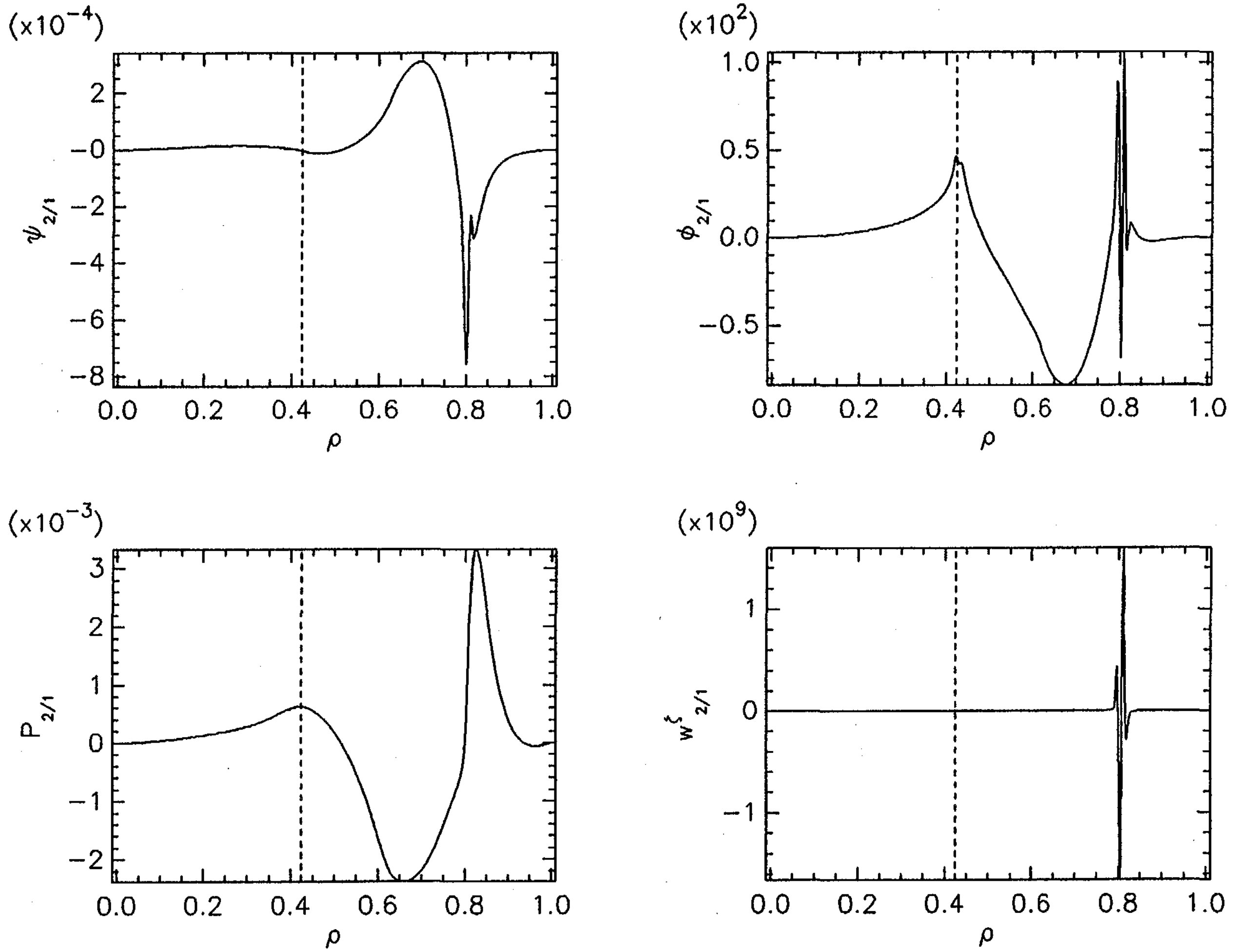

Figure 3.34: Eigenfunctions for the 2/1 mode for equilibrium A.1 and $\beta_0 = 0.068$ illustrate significant mode coupling to an instability at the $q = 4/1$ surface. The $q = 2/1$ rational surface is marked by the dashed vertical line.

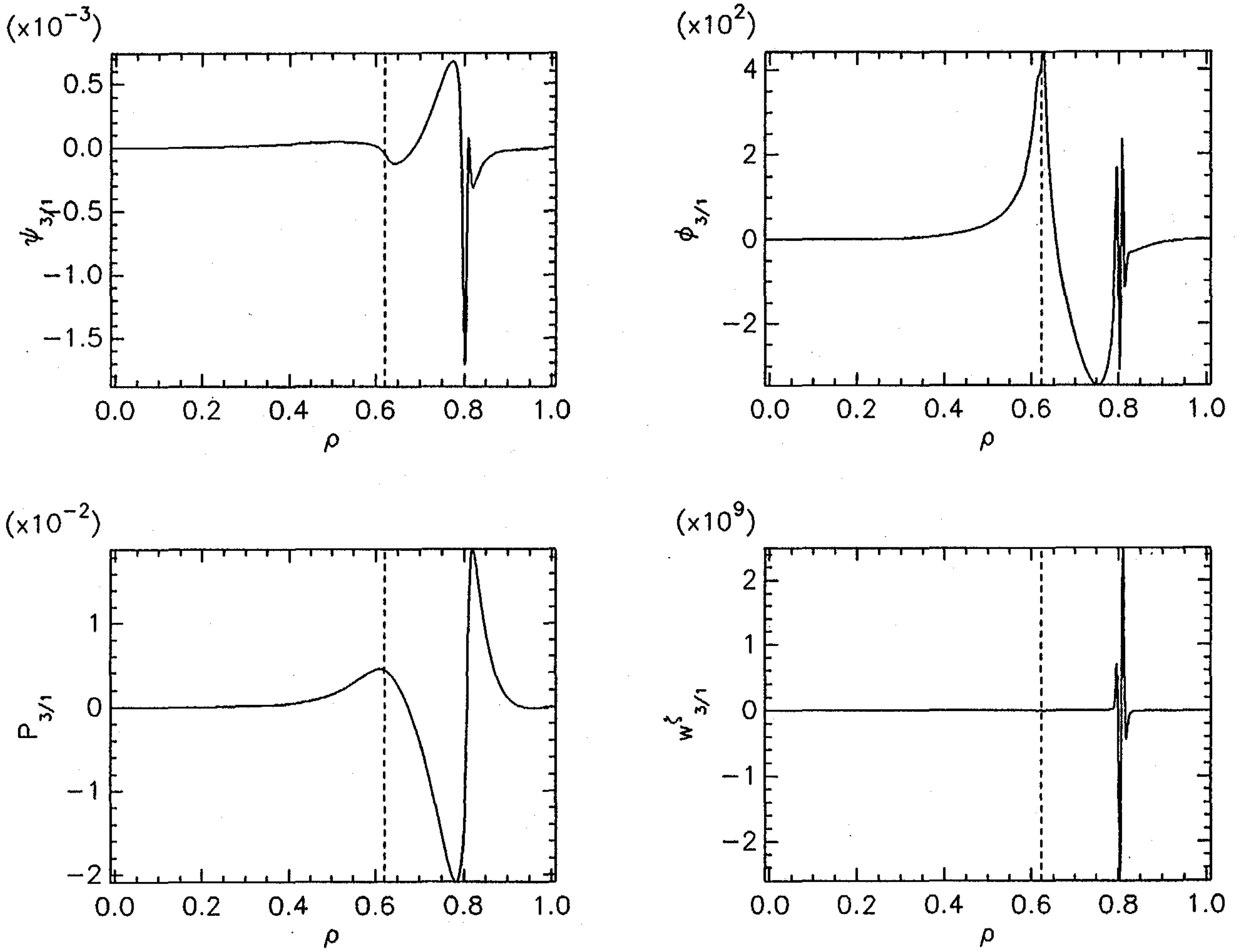

Figure 3.35: Eigenfunctions for the 3/1 mode for equilibrium A.1 and $\beta_0 = 0.068$ illustrate significant mode coupling to an instability at the $q = 4/1$ surface.

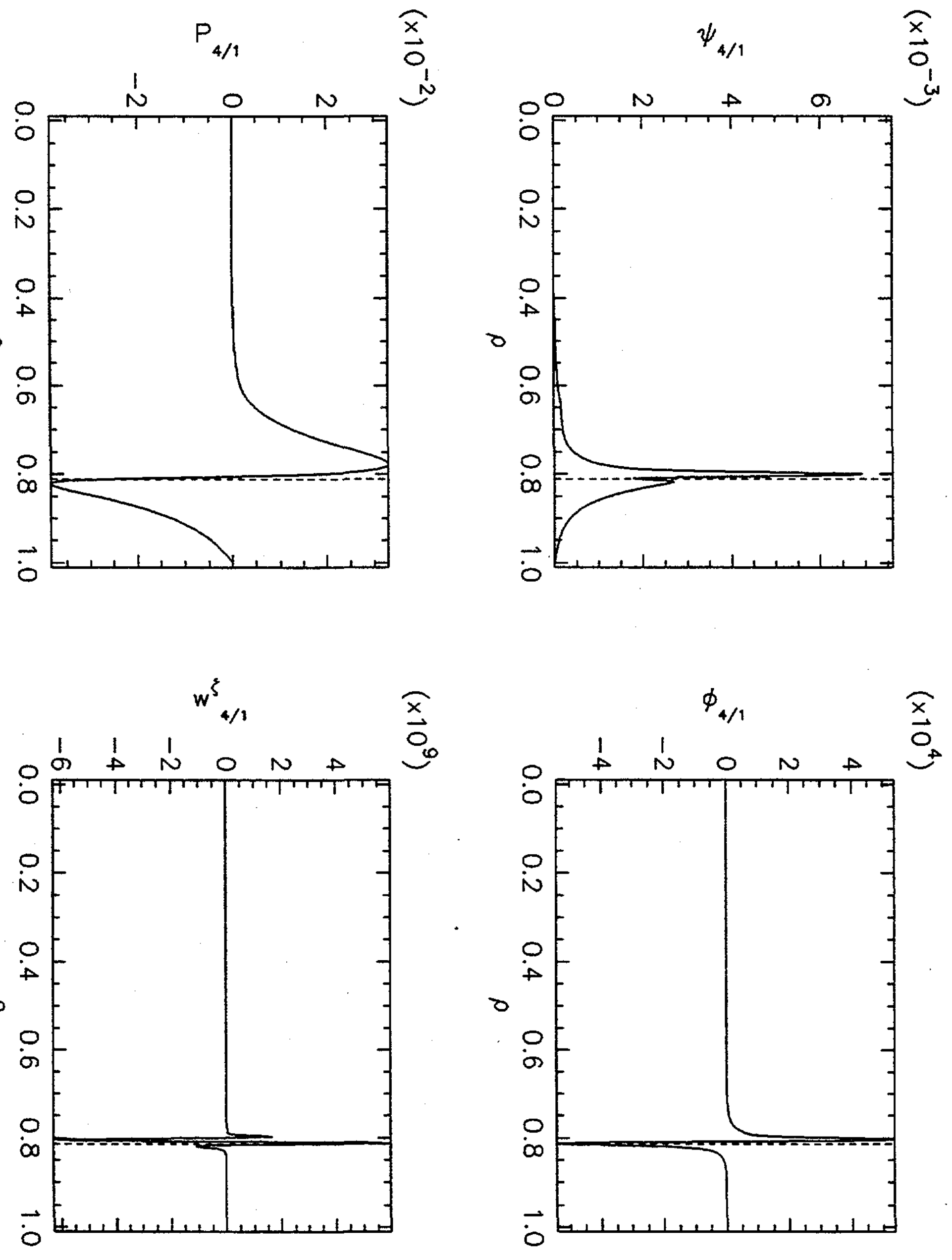

Figure 3.36: Eigenfunctions for the 4/1 mode for equilibrium A.1 and $\beta_0 = 0.068$ illustrate an instability at the $q = 4/1$ surface.

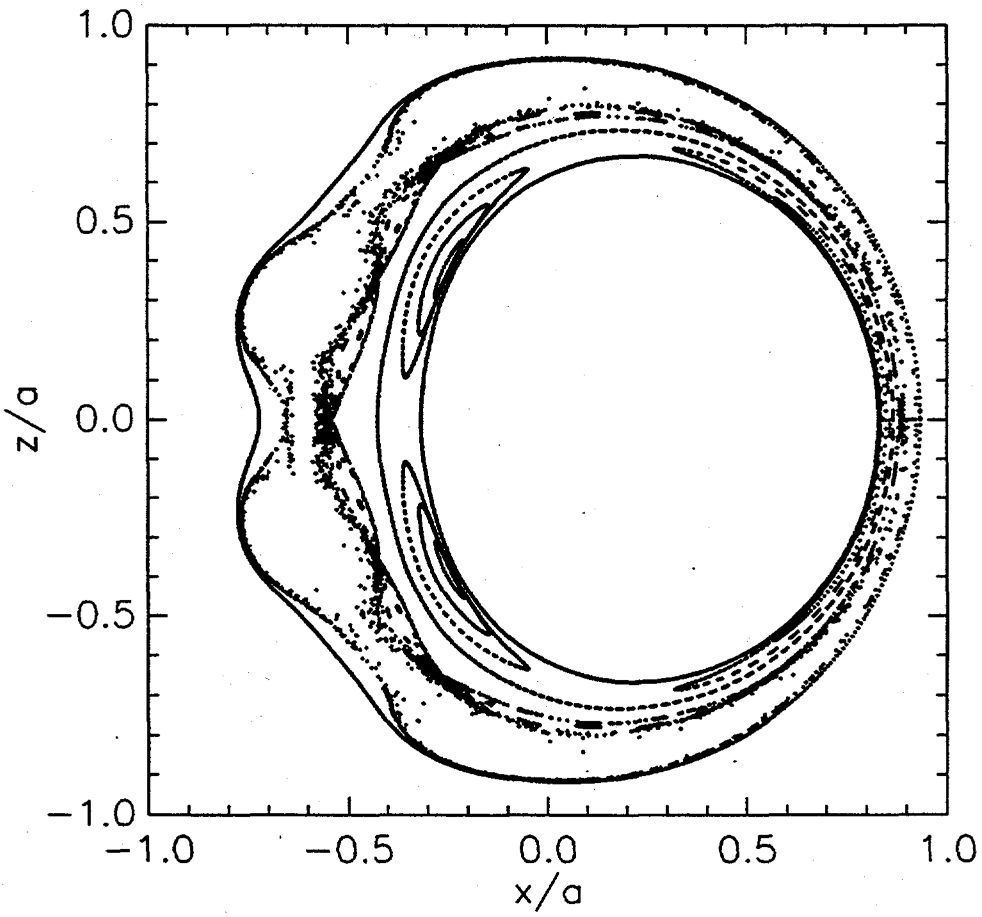

Figure 3.37: Magnetic puncture plot for a coupled 2/1, 3/1 and 4/1 mode based on equilibrium A.1 and $\beta_0 = 0.068$ illustrates that the 2/1 and the 3/1 modes are magnetic islands. Note also the existence of secondary magnetic islands and KAM surfaces which separate the magnetic islands of different helicities.

3.2.3 Pressure evolution dynamics

In the model used in this thesis, an anisotropic pressure diffusivity which accounts for differences in perpendicular ($\chi_\perp$) and parallel ($\chi_{||}$) heat transport has been assumed. In a real plasma these coefficients, along with the plasma resistivity, would depend on various plasma parameters (temperature, density, turbulence levels, etc.). However, the assumption has been made that in the vicinity of any particular island the effect of topological changes associated with the island are likely to be dominant over these spatial variations. Consequently, $\chi_\perp$and $\chi_{||}$ will be assumed to be constants across the entire extent of the plasma. In principle, FARGO, the code used in these numerical simulations, could be run in a fully nonlinear turbulent mode with dynamic versions of $\chi_\perp$ and $\chi_{||}$ which could address such effects, but at the expense of more complicated nonlinear terms and much longer compute times.

The particular choice of values for $\chi_\perp$ and $\chi_{||}$ will reflect three time scales: the parallel equilibration time, the energy confinement time, and the resistive time. The ratio of the first two time scales is based on the observation that free streaming of electrons along the magnetic field lines produces rapid equilibration of pressure along a field line, while the pressure transport across the magnetic field lines is constrained. This implies that $\chi_{||}/\chi_\perp \gg 1$. This choice of $\chi_{||}$ also plays a significant role in the determination of a short enough time step to avoid numerical instability associated with the explicit time advance of the nonlinear portion of the parallel heat flux, yet long enough to simulate the island growth over a fraction of the resistive time scale. The ratio of the last two time scales is based on the experimental observation that the energy confinement time ($\sim$ 100 ms in TFTR) is faster than the resistive timescale ($\sim$ 10 s in TFTR), which implies a dimensionless $\chi_\perp \sim 100$. This choice of $\chi_\perp$ is central to insuring that the pressure equilibrates while the island evolves, rather than that the pressure gradients external to the magnetic island steepen during island growth or significantly lag the evolution of the magnetics. The eigenfunctions throughout subsection 3.2.2 elucidate the pressure lagging of the magnetic field when $\chi_\perp = 10$.

In the low β ($\beta_0 = 0.006$) case of subsection 3.2.1, $\chi_\perp = 100$ and $\chi_{||} = 10^7$, and the pressure played a minimal role in the dynamics of the magnetic island evolution. In this low β limiting case, the pressure dynamics can be described based on rapid parallel transport which effectively "short-circuits" the perpendicular pressure gradient across the island region. This flattening of the pressure profile across the island appears as the pressure decrease in the 0/0 component of the pressure between the magnetic axis and the island, as illustrated in Figure 3.22. A simple estimate of this pressure drop on axis based on the "belt" model of Chang and Callen [38] is $p_{0/0} = -W dp_0/d\rho|_{\rho_0}$, where W is the island width and $dp_0/d\rho$ is the equilibrium pressure gradient evaluated at the rational surface. This figure also illustrates that the effect of the pressure relaxation has not completely propagated to the magnetic axis but requires a finite time of order the energy confinement time to equilibrate throughout the plasma. By the time the island reaches the Rutherford phase as illustrated in Figure 3.26, the pressure has fully relaxed with respect to the island size, which is at least partly due to a reduction in the growth rate. The general criterion required to avoid pressure steepening is $R = \chi_\perp^{-1} W dW/dt \ll 1$ [39]. At the end of the linear phase for Equilibrium A.1 at $\beta_0 = 0.006$ the island width is on the order of $W \simeq 0.001$ and the linear growth rate for this island at $S = 10^7$ is $\gamma\tau_R = 5620$. The parameter $R = 0.56$ is no longer small, which explains most of the finite time lag in the pressure at the axis. In the simulations presented in subsection 3.2.1, $\chi_\perp = 100$ and the pressure does not quickly equilibrate only during the early phases of the island growth and this is principally at the major axis ($\rho = 0$).

For the magnetic island evolution illustrated in the prior subsections, the islands saturate at a small amplitude and appear to generate Fourier harmonics consistent with theory. However, the small island size precludes an accurate assessment of the helical structure of the pressure contours and an exact assessment of the pressure equilibration on the magnetic flux surfaces—a feature which is necessary for the threshold destabilization of the neoclassical tearing mode. To explore these issues and complications, a single large "static" magnetic island is considered but in the absence of a pressure convection term. Figure 3.38 illustrates the pressure contours superimposed on a puncture plot of the magnetic field lines for a finite value of $\chi_\parallel/\chi_\perp = 10^5$ (in a real experiment this ratio could be much larger; perhaps as large as 10^{10} in TFTR plasmas). In an ideal situation, where $\chi_\parallel/\chi_\perp \to \infty$ or where the magnetic fluctuations are zero, the pressure contours and field lines would exactly coincide, as is observed far from the magnetic island. However, in the vicinity of the island X-point even though the perpendicular transport is slow, the transit time across the X-point for a small distance δ_x is quite short: $\tau_\perp = k_\perp^2 \chi_\perp \simeq \chi_\perp/(\delta_x)^2$. On the other hand, the singular nature of the separatrix requires heat to travel an infinite distance in the parallel direction to cross the X-point: $\tau_\parallel = k_\parallel^2 \chi_\parallel$. If a Taylor expansion of a mode is made about the rational surface, then $k_\parallel = \delta_x (m/q)(dq/d\rho)$. A balance between these two time scales generates a scale length at which the transport changes form being parallel to perpendicular dominated. The scale length is

$$\delta_x \simeq \left(\frac{\chi_\perp}{\chi_\parallel}\right)^{0.25} \left(\frac{m}{q}\frac{dq}{d\rho}\right)^{-0.5}\Bigg|_{\rho=\rho_0}, \tag{3.12}$$

which for realistic plasmas is very small ($\sim 10^{-3}$). This combination of scale lengths and timescales allows the island to support a weak pressure gradient across the X-point rather than producing a distinct X-point in the pressure contours. This feature proves to be pivotal for the amplitude threshold for generation of the neoclassical MHD instabilities of the next section.

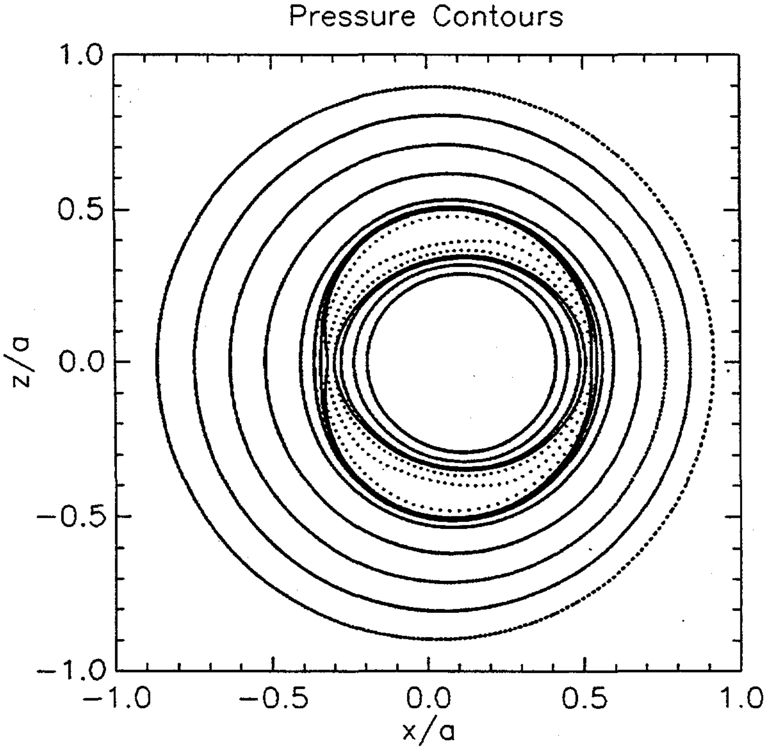

Figure 3.38: Superposition of the pressure contours on the magnetic field line puncture plot illustrate that the deviation of pressure equilibration on flux surfaces is localized to the vicinity of the magnetic island. A static magnetic perturbation of $\psi_1(\rho = \rho_0) = 10^{-4}$ at the rational surface has been assumed. On the contours outside the magnetic island, the pressure contours coincide with the magnetic flux surfaces to the accuracy that can be illustrated graphically.

While Figure 3.38 qualitatively illustrates that the pressure does not completely equilibrate along the flux surfaces, the degree to which the pressure has equilibrated along a flux surface can be quantified by computing the pressure variance (σ^2) along a field line. In Figure 3.39 this pressure variation is presented as a function of $\chi_{\|}/\chi_{\perp}$ beginning at select points across an island X-point. As expected, the pressure variation is largest near the resonant rational magnetic surface, and for $\chi_{\|}/\chi_{\perp} = 10^6$ has a magnitude of $\sim 1 - 2\%$. The variance is largest near the mode rational surface, because the field line passes through the vicinity of the island X-point where transport is dominated by perpendicular diffusion to regions near the separatrix across the island O-point where transport is dominated by parallel diffusion. This trend is further clarified in Figure 3.40 which illustrates that the peak pressure variance decreases as a function of $\chi_{\|}/\chi_{\perp}$.

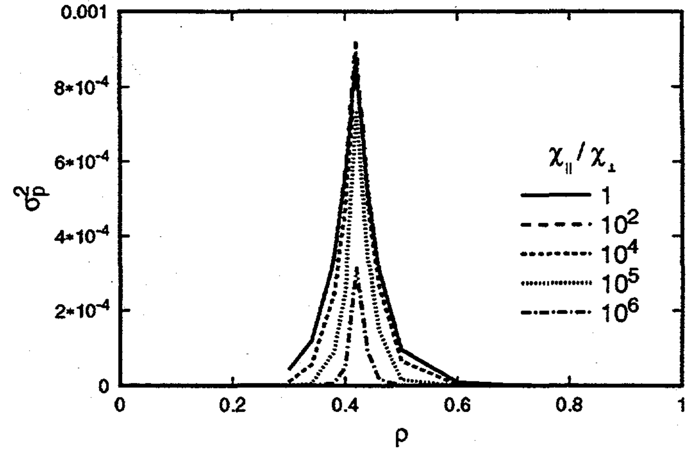

Figure 3.39: An increase in $\chi_{\|}\chi_{\perp}$ increases the degree to which the plasma pressure equilibrates on the flux surface. The pressure variance is computed by following individual field lines approximately 3200 times around the torus (200000 iterates at a $\Delta\zeta = 0.1$ step size) and computing the pressure along the field line. This pressure is used to compute the mean pressure on a field line and also the pressure variance. Initial starting points cross through an island X-point.

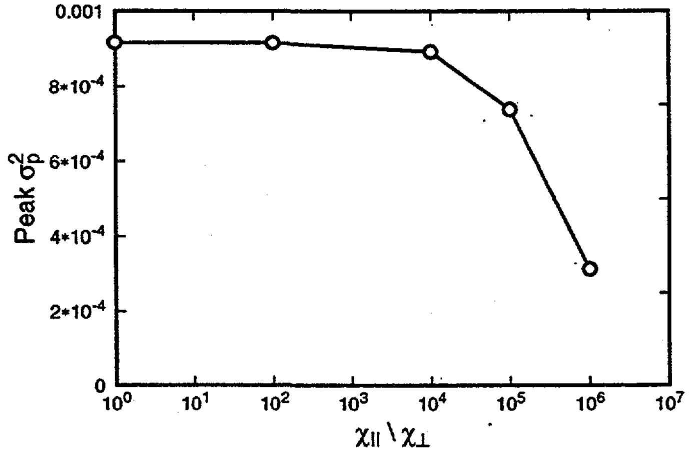

Figure 3.40: An increase in $\chi_{||}\chi_{\perp}$ decreases the peak pressure variance. The peak is located at or near the mode rational surface.

The final issue which the pressure evolution affects is the numerical stability of the time advance scheme, especially in the nonlinear phase. In a computer with infinite precision, a timestep could always be chosen which would insure stability of the algorithm. However, the necessity of time advancing the equations for a significant fraction of the resistive time requires an unreasonable expenditure in compute time, even before numerical rounding errors become a problem. A reasonable choice to insure stability for a value of $\chi_{||} = 10^7$ is to use a timestep of $10^{-9}\tau_R$ when $\psi_1 \sim 10^{-4}$. As ψ_1 increases in value the timestep must be further reduced. With this timestep, and taking advantage of larger timesteps in the early linear phase, a typical run of 15 modes requires roughly 2 weeks in real time on an IBM/RISC6000 model 370 (25 Mflops, SPEC92Int=70.3, SPEC92FP=121.1) [46]. While this solution does not generate the best pressure equilibration, it will be sufficient to elucidate the threshold destabilization of the neoclassical MHD tearing mode. One possible recourse is to adapt an additional iterative loop for the pressure dynamics which could operate on a faster time scale than the evolution of the magnetics.

3.3 Neoclassical Tearing Modes

In the previous section, considerable time was spent reviewing the standard Δ' tearing mode as a confirmation of the operational aspects of the simulations and also to understand the numerical requirements for stability, convergence and resolution of a tearing mode. In this section, the analysis of the tearing mode is extended to a class of unstable modes which are not dependent on Δ' for stability, but instead are driven by neoclassical effects.

Neoclassical effects arise from the viscous damping of the poloidal electron flow. The portion of the flow produced from the poloidal projection of the diamagnetic current when balanced against electron-ion friction yields a parallel current proportional to the cross-field pressure gradient, the bootstrap current. When $(dp_0/d\rho)/(dq/d\rho) < 0$, this perturbation reinforces the magnetic perturbation of the island and an instability may grow in time. [The neoclassical modes are predicted to be stable in reversed shear tokamak discharges where $(dp_0/d\rho)/(dq/d\rho) > 0$.]

The perturbed bootstrap current as superimposed on the island separatrix in Figure 3.41 has a structure which corresponds to the island separatrix. (The separatrix is computed in a manner analogous to the island width calculation.) However, the contours of the bootstrap current are not easily interpreted in terms of stabilizing and destabilizing regions. Consequently, a different but related quantity will be computed by multiplying the Ohm's law by ψ_1. The result is

$$\frac{\partial}{\partial t}\frac{\psi_1^2}{2} = -\psi_1 \vec{B} \cdot \nabla \phi + \psi_1 R^2 J_1^\zeta - \psi_1 \vec{B} \cdot \nabla \cdot \vec{\vec{\pi}}, \tag{3.13}$$

where the nonlinear terms have been neglected. From a plot of the magnitude contours for each of the above terms, the stabilizing (negative valued) and destabilizing (positive valued) contributions can be identified. In Figure 3.42, the perturbed bootstrap current times ψ_1 has been plotted. A large destabilizing bootstrap current contribution exists inside the island separatrix and a small stabilizing bit exists in the vicinity of the island X-point. The fact that a perturbed bootstrap current exists inside the island separatrix may seem contradictory to the earlier statements about pressure flattening eliminating the bootstrap current within the island. However, the two viewpoints can be reconciled by noting that the quantities presented here are perturbative quantities, so that the perturbed bootstrap current of Figure 3.42 is the current required to flatten the equilibrium bootstrap current.

The picture is incomplete without consideration of the remaining terms in Eq. 3.13. In Figure 3.43, the contours for the dominant term of $\psi_1 R^2 \vec{J}_1^\zeta$ [i.e., the $\hat{g}^{\rho\rho}$ portion of J_1^{ζ} defined in Eq. (2.62)] indicate that the resistivity plays a stabilizing role inside the island separatrix, but is smaller than the bootstrap current contribution. Also, a small destabilizing region exists about the island X-point. The stabilizing effect is probably a reflection that the equilibrium is Δ' stable. The remaining term is $-\psi_1 \vec{B} \cdot \nabla\phi$, which is plotted in Figure 3.44. A comparison of this figure with both the resistivity and the bootstrap current indicate that this term plays a negligible role in the mode destabilization. Furthermore, this term cannot produce reconnection.

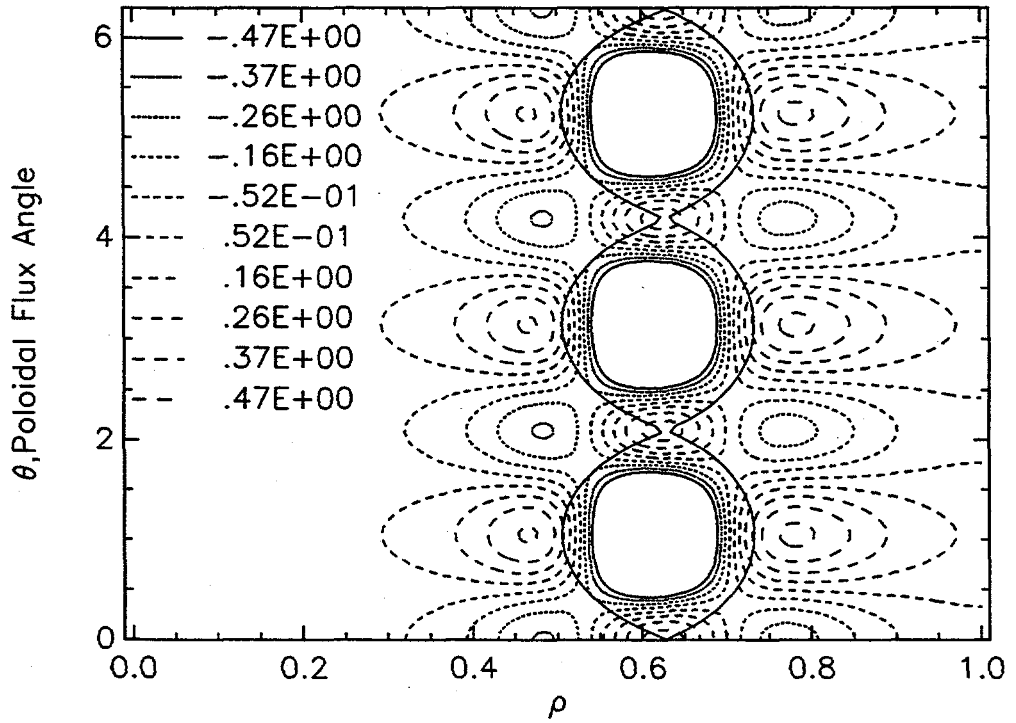

Figure 3.41: The contours of the perturbed bootstrap current [Term 1 of Eq. (2.86)] indicate that a large negative current (solid lines) exists inside the island separatrix (the thick solid line) and large positive currents (dashed lines) exist about the island X-point. The negative current adds to the the equilibrium bootstrap current to produce no net bootstrap current inside the separatrix.

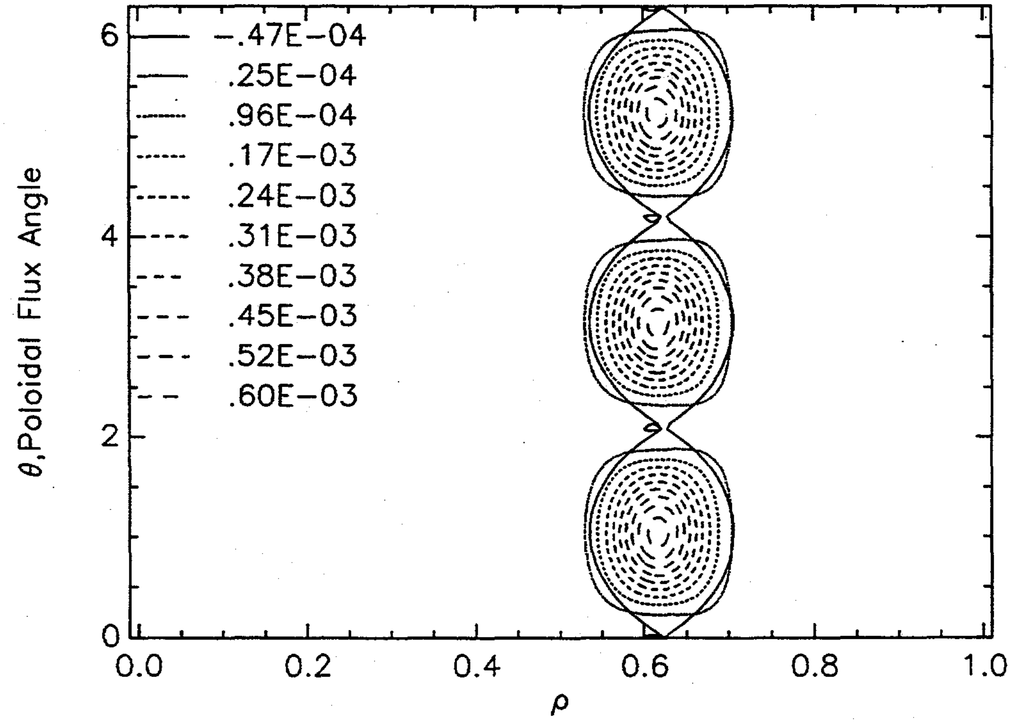

Figure 3.42: The contours of the product of the perturbed bootstrap current with ψ [Term 1 of Eq. (2.86) times $\psi_{3/1}$] indicate the bootstrap current is destabilizing (positive valued) within the island separatrix and stabilizing (negative valued) in a small zone about the island X-point.

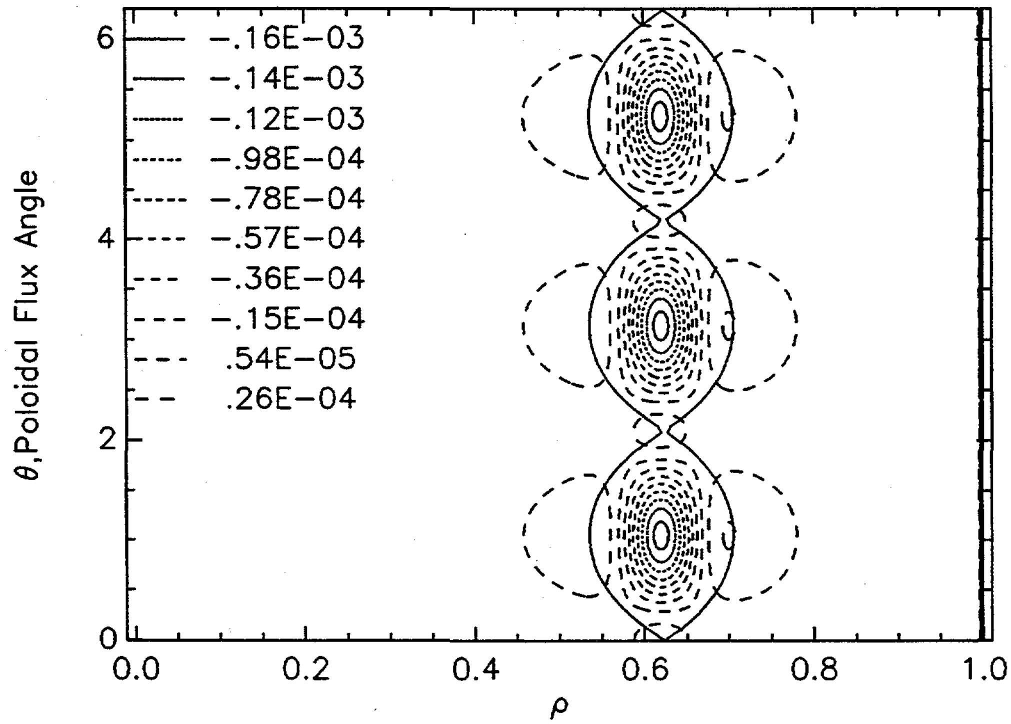

Figure 3.43: The contours of the dominant portion of $\psi_1 R^2 \vec{J}_1^\zeta$ is stabilizing (< 0) inside the island separatrix, which is indicated by the thick solid line. The dominant piece is the $\hat{g}^{\rho\rho}$ portion of J_1^ζ.

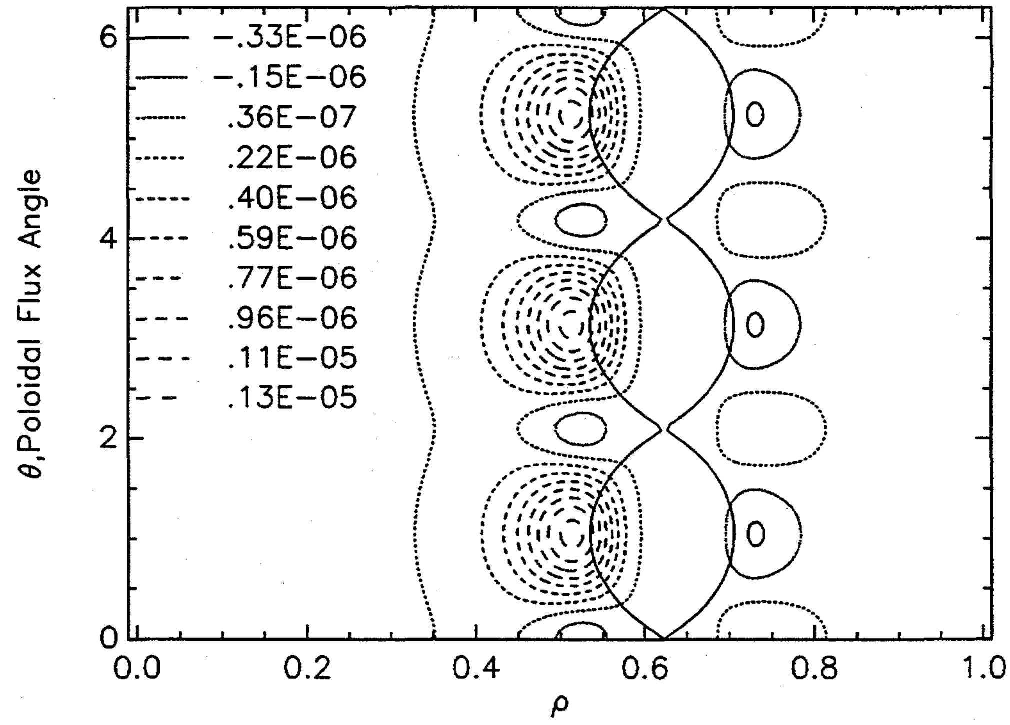

Figure 3.44: The contours of $-\psi_1 \vec{B} \cdot \nabla\phi$ indicate that this term is slightly destabilizing (> 0) between the island separatrix and the magnetic axis ($\rho = 0$) and stabilizing between the separatrix and the plasma edge ($\rho = 1$). Note that the magnitude of this term is much smaller than the other terms of Ohm's law, and hence negligible.

In an ideal simulation the island growth rate is slow relative to the pressure evolution and $\chi_{||}/\chi_{\perp} \to \infty$, so that even at small mode amplitudes, the mode is unstable because the pressure exactly equilibrates on the magnetic flux surfaces $(\vec{B} \cdot \nabla p = 0)$. However, the introduction of finite values of $\chi_{||}$ and $\chi_{\perp}$ at small island amplitude produce an insufficient perturbation of the pressure profile to destabilize the neoclassical magnetic island—a threshold in magnetic island width, $W_{threshold}$. As was introduced in Section 1, when the island width is smaller than this width, $(W < W_{threshold})$ the island decays; however when the island is larger than this width, $(W > W_{threshold})$ the island grows. This dependence on the initial perturbation magnitude [see Eq. (2.6)] is illustrated for the $\beta_0 = 0.068$ equilibrium of A.1 in Figure 3.45.

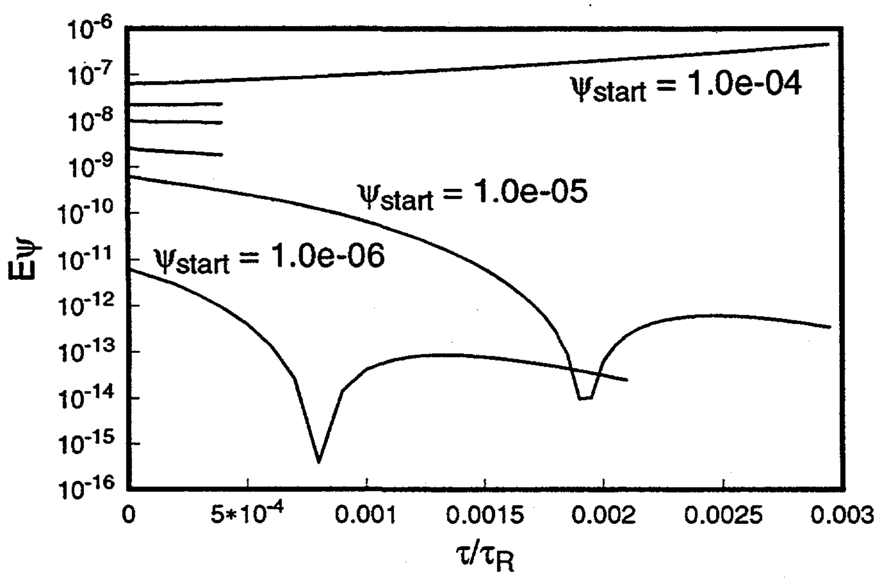

Figure 3.45: Destabilization of the neoclassical tearing mode requires a finite perturbation to initiate the mode. Here, Ψ_{start} is the magnitude of the initial perturbation evaluated at the mode rational surface. The initial profile shape decays toward zero value at both boundaries. The oscillatory behavior of the decaying solutions is a linear effect driven by $\vec{B} \cdot \nabla\phi$ causing ψ_1 to oscillate as it decays.

The neoclassical MHD threshold is also strongly dependent on the plasma pressure (β_0) since the bootstrap current depends directly on the gradient of the plasma pressure. (Theory indicates a scaling not with β_0 but with β_p, the poloidal β.) Subsequently, as the pressure is increased (e.g., when the neutral beams are turned on in TFTR), a given initial magnetic perturbation may cross the threshold and be destabilized, as is illustrated in Figure 3.46. Much

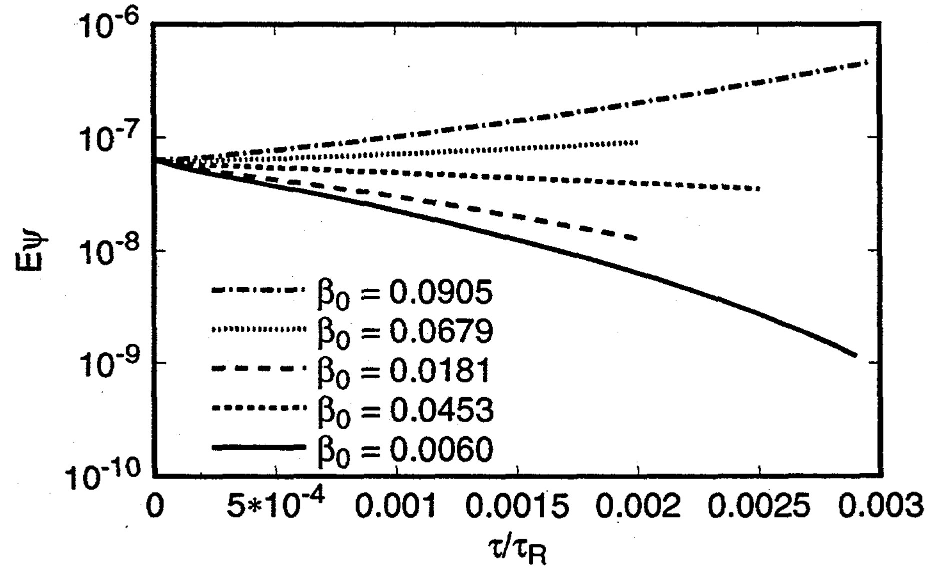

Figure 3.46: For a given initial magnetic perturbation, an increase in plasma pressure causes destabilization of the neoclassical MHD tearing mode.

of this analysis can be combined into a threshold curve for a given $\chi_{||}/\chi_{\perp}$ by performing a parameter scan over β_0 and Ψ_{start}. Figures 3.47, 3.48, and 3.49 provide such a threshold curve for the 2/1, 3/1, and 3/2 modes, respectively, and compare the numerically computed threshold with the predictions of the Fitzpatrick threshold [see Eq. (1.10)].

The predictions between theory and the simulations in general show good but not perfect agreement. The difference is likely due to several related features. These simulations are conducted in a toroidal geometry, with no inherent approximations built into the form of the operators. On the other hand, the theory exploits various expansions about the mode rational surface to define operators. Differences between these operators produce changes in the bootstrap current profile about the island which would affect the stability threshold. One possible difference between the model and the simulations is that inherent differences exist between the pressure profiles, especially about the X-point. These differences would lead to differences in the critical length scale of Eq. (3.12) for the two models. In the case of the 2/1 mode, the critical scale length for the simulation is smaller than implied by the theory. In contrast for the case of the

3/1, the critical scale length for the simulation is longer than implied by the theory and the 3/2 scalelength is smaller than the theory. Since, no systematic data trend is apparent, this rules out this possibility. A more likely cause for the differences is that in computing the Fitzpatrick threshold the approximation $\Delta' = -2m/\rho_0$ has been made, because the simulations do not compute the value of Δ'. The difference between the actual value and the approximated value may be solely responsible for the difference.

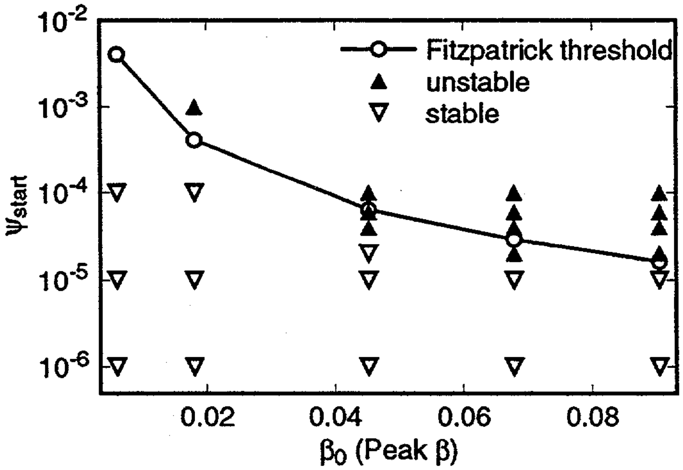

Figure 3.47: Neoclassical MHD tearing threshold for the 2/1 mode based on numerical simulations are in rough agreement with the predictions of neoclassical MHD theory.

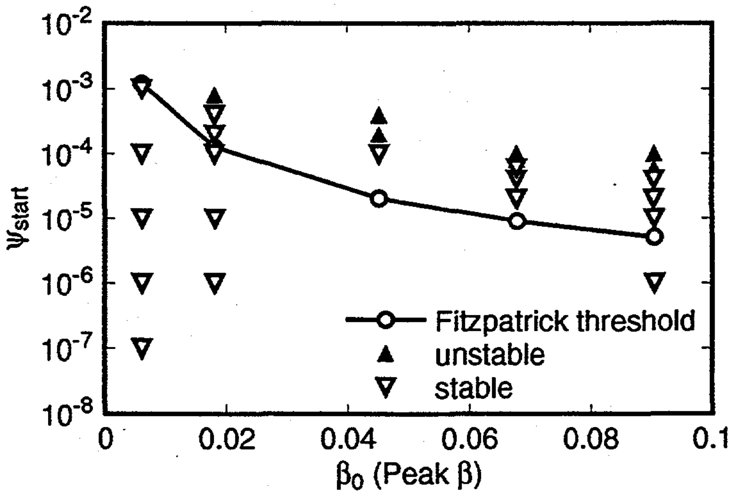

Figure 3.48: Neoclassical MHD tearing threshold for the 3/1 mode based on numerical simulations are approximately a factor of 10 larger than the predictions of neoclassical MHD theory.

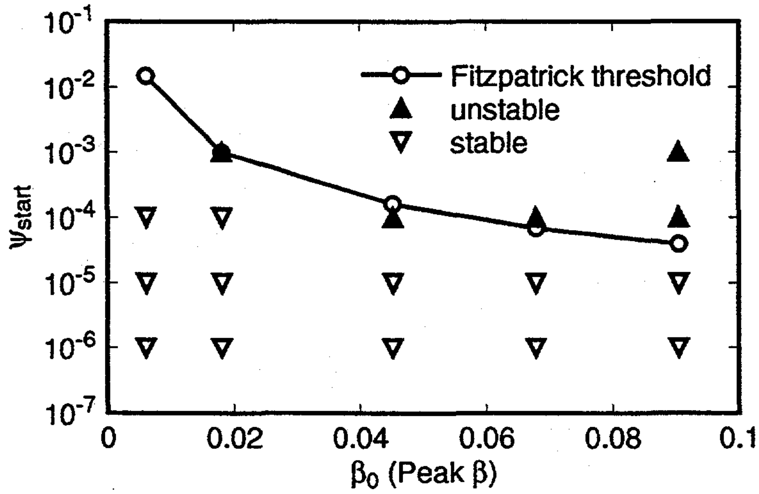

Figure 3.49: Neoclassical MHD tearing threshold for the 3/2 mode based on numerical simulations are approximately the same as the predictions of neoclassical MHD theory.

An inspection of the pressure contours superimposed on a puncture plot of the magnetic field lines, Figures 3.50 and 3.51, conveniently demonstrates that a pressure gradient, albeit weak, is maintained in the vicinity of the island X-point. The extension of these contours into the island O-point is also a reflection of a flattened pressure profile across the O-point and to some extent the island X-point.

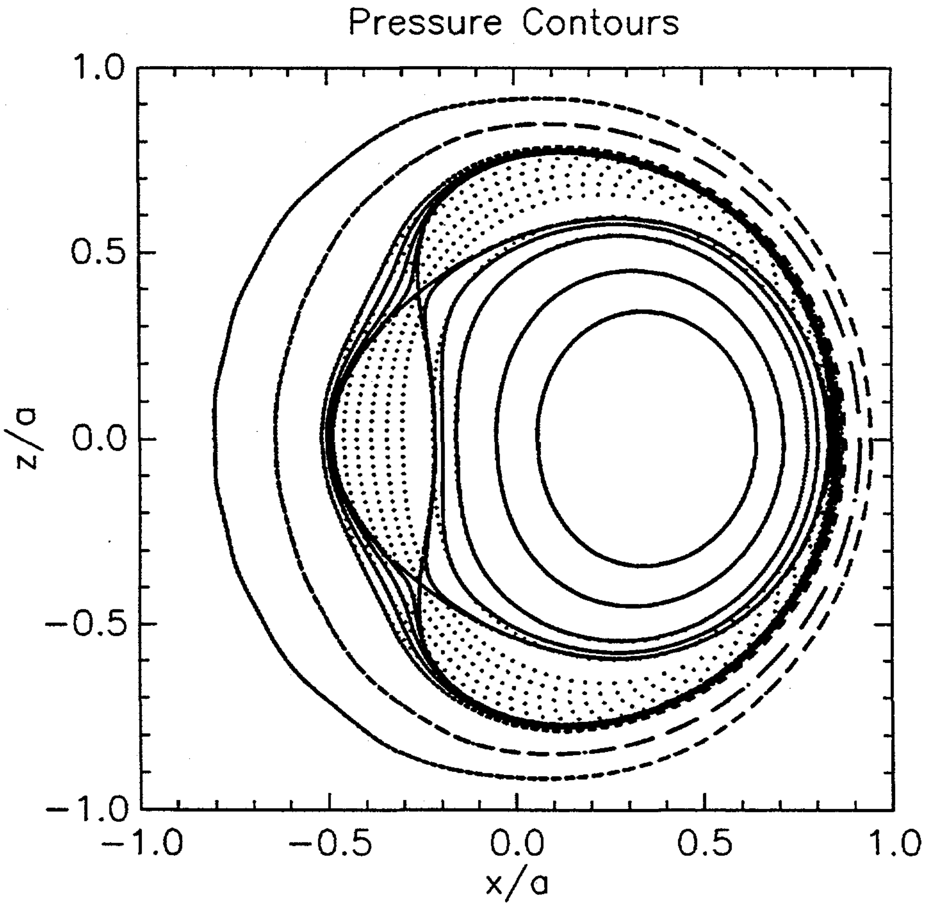

Figure 3.50: Pressure contours for a neoclassical MHD tearing mode based on Equilibrium A.1 for $\beta_0 = 0.067$ superimposed on the puncture plot illustrate a flattened pressure profile across both island X-point and O-point. This is at a toroidal angle of $\zeta = 0$.

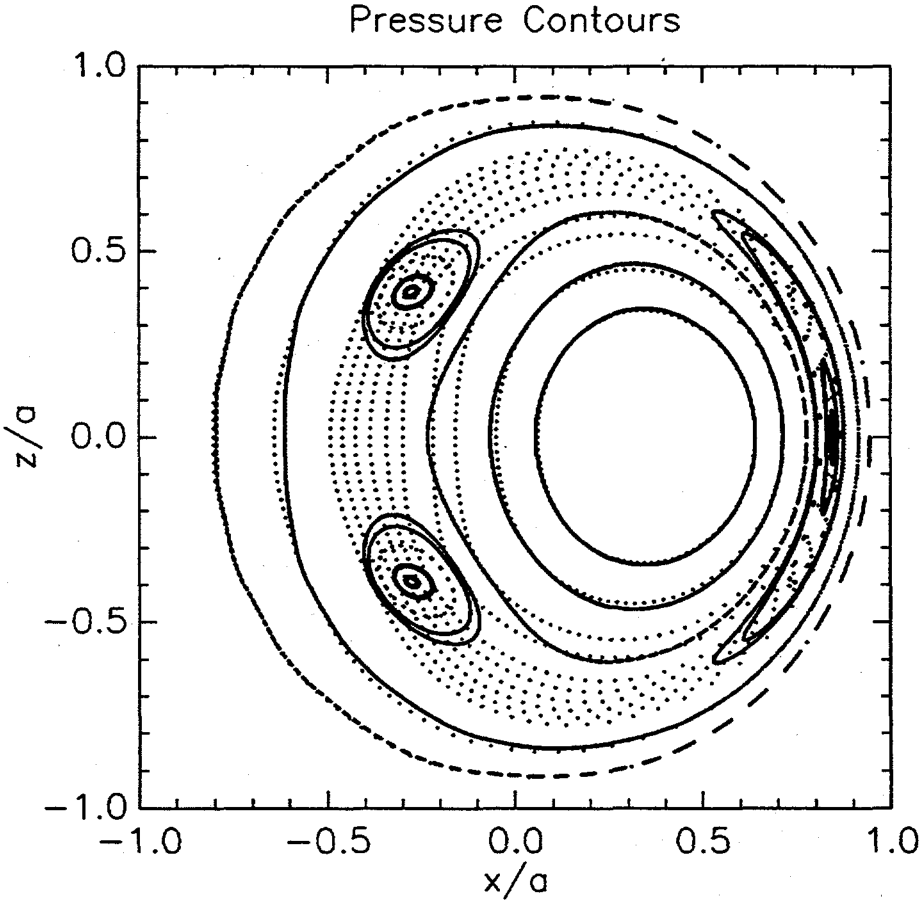

Figure 3.51: Pressure contours for a neoclassical MHD tearing mode based on Equilibrium A.1 for $\beta_0 = 0.067$ superimposed on the puncture plot illustrating a flattened pressure profile across both island X-point and O-point. This is at a toroidal angle of $\zeta = \pi$.

The most important feature which can lower the neoclassical tearing mode threshold is an increase in the ratio of $\chi_{\|}/\chi_{\perp}$. Unfortunately, numerical difficulties preclude increasing this ratio to a TFTR relevant value of $\chi_{\|}/\chi_{\perp} \sim 10^{10}$. However, decreasing this ratio as is illustrated in Figure 3.52 demonstrates the strong stabilizing/destabilizing role this ratio plays, since previously unstable initial conditions have now been stabilized.

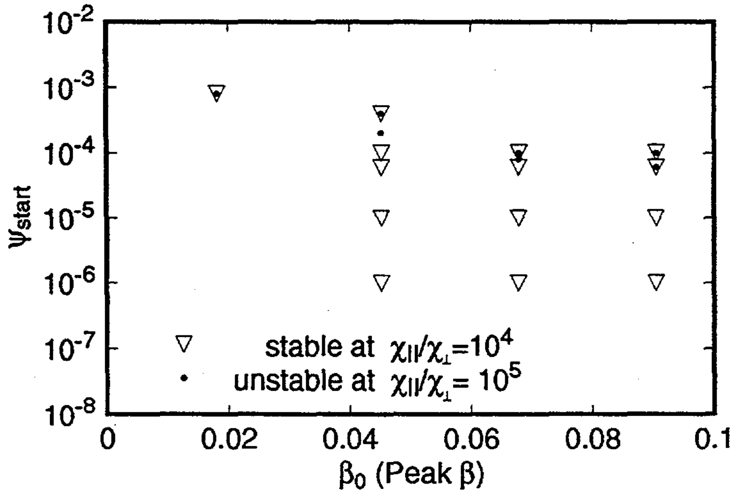

Figure 3.52: Reduction of $\chi_{\|}/\chi_{\perp}$ to 10^4 increases the neoclassical threshold. Initial conditions which were unstable at $\chi_{\|}/\chi_{\perp} = 10^5$ are now stable.

Once the island is over the neoclassical threshold and the initial transients have decayed away, the island width growth rate is proportional to the island width as illustrated in Figure 3.53. In this particular case, the island width has reached over 20% of the plasma minor radius. However, the calculation has been terminated at this point because in order to maintain the stability of the pressure evolution the time step must be reduced below $0.01\tau_A$, which would then imply much longer compute times. Also, the predicted saturation level for the mode is beyond the size of the tokamak, so saturation is not likely to be obtained. Neither the large thresholds nor the large saturation levels presented in the prior simulations should be construed as a generic part of neoclassical MHD. In order to get the physics which has been described, rather extreme parameter ranges have been required which are in general not realizable in actual machines. However, this was required since the simulations are limited by $\chi_{\perp}/\chi_{\|}$.

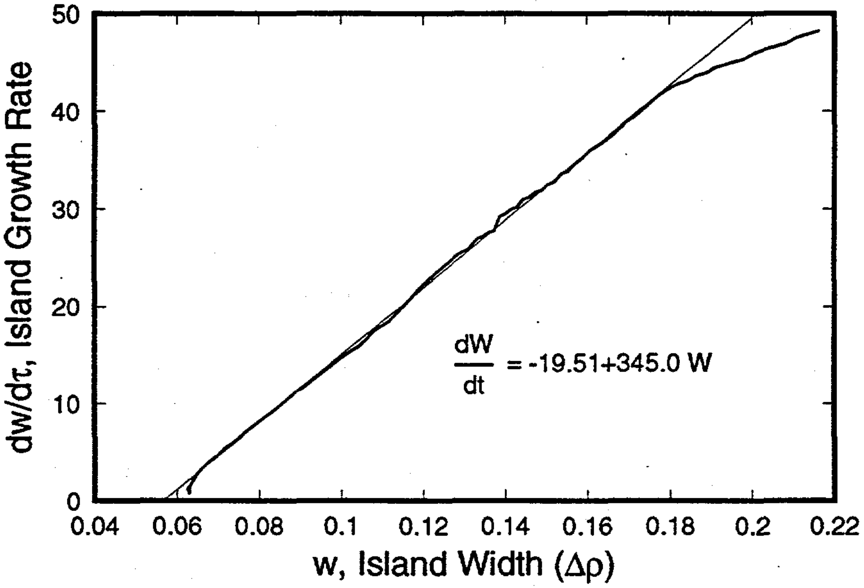

Figure 3.53: After the neoclassical threshold, the island width grow rate is proportional to the island width, until nonlinear effects begin to slow the island growth. The simulation was terminated at an island width of 20% of the minor radius due to numerical problems.

Chapter 4

Summary and Future Work

The high β reduced magnetohydrodynamics (MHD) paradigm has been extended to include viscous force ($\nabla \cdot \vec{\vec{\pi}}$) effects based on neoclassical closures. This neoclassical reduced MHD model consists of evolution equations for the perturbed flux, toroidal vorticity, and plasma pressure, through quasineutrality, a parallel Ohm's Law, a toroidal vorticity evolution, and a plasma pressure evolution equation. The plasma pressure evolution includes an anisotropic pressure diffusivity to account for rapid parallel energy transport. The viscous stress tensor adds a bootstrap current contribution to the parallel Ohm's law [Eq. (2.86)] and a neoclassical viscosity to the vorticity evolution equation [Eq. (2.99)]. The model is principally valid only in the large aspect ratio limit due to the assumptions of plasma incompressibility and the use of only a single stream function to define the flow velocity (i.e., the velocity is an $\vec{E} \times \vec{B}$ flow), which are necessary to derive reduced MHD. Both magnetic potentials are retained, but the incompressibility assumption relates the poloidal magnetic potential to the plasma pressure ($p_1 = -\vec{B}_1 \cdot \vec{B}_0$), which allows the model to be extended to high β and also eliminates the magnetosonic wave. Even though the model is strictly valid only in a large aspect ratio limit, the equilibrium metric elements, which describe the toroidal geometry, are retained to all orders to allow for poloidal mode coupling.

This neoclassical reduced magnetohydrodynamics model has been numerically implemented based on the ORNL FARGO code. The numerical implementation uses a straight-field-line representation of the equilibrium, Fourier decomposes perturbations in the poloidal ($\nabla\theta$) and toroidal ($\nabla\zeta$) directions, and central finite differences in the radial/flux ($\nabla\rho$) direction. Linear terms are implemented with an implicit time advance and nonlinear terms are implemented with an explicit time advance. The code can be operated in either a turbulent mode of operation where many thousands of harmonics are retained in the calculation, or, as has been done in this case, a nonlinear mode where only a few key harmonics plus the equilibrium harmonics are time advanced.

Three nonlinear series of simulations have been completed with this neoclassical reduced MHD solver: 1) The single helicity Δ' tearing mode; 2) The toroidal tearing mode; and 3) The single helicity neoclassical tearing mode. The first two series have been used to qualitatively benchmark the code against existing theory and also to identify current gradient driven instabilities which may confuse the investigation of the neoclassical tearing mode. In the first series of runs (Section 3.2), basic features of a standard $m/n = 2/1$, Δ' unstable tearing mode have been identified, which include a scaling of $\gamma\tau_R \sim S^{2/5}$ in the exponential phase, the existence of a Rutherford growth phase, quasilinear saturation of the island growth by flattening of the equilibrium current gradient, and pressure curvature stabilization as per the Glasser effect [31]. This simulation also reflects a significant advancement in computer simulation over the last decade which has extended the validity and accuracy of these simulations to experimentally relevant regimes with magnetic Reynold's numbers as large as $S = 10^8$, and beyond.

In the second series of runs (Section 3.3), multiple helicity magnetic islands with equilibrium pressure and q profiles reminiscent of TFTR are considered. In this case, each of the single helicity modes are stable. However, the introduction of multiple helicities generates an unstable $m/n = 2/1$ tearing mode at the q=2 rational surface which has similar features to a standard unstable Δ' tearing mode. Presumably, poloidal mode coupling, consistent with E-matrix theory estimates with an unstable ballooning twisting-like structure at the q=3 and q=4 surfaces, drives this tearing mode. However, this numerical implementation extends beyond the E-matrix theory since coupling between all modes can be retained with no explicit ordering assumptions. Also, as β is increased, the coupled modes switch from evolving to a saturated state to unbounded growth, i.e., a disruption (see Figure 3.32). The results of these simulations could provide a new type of model for disruptions in tokamaks.

In the final series of simulations, single helicity, neoclassical MHD driven tearing modes are demonstrated to exist. The neoclassical tearing mode is driven by the elimination of the bootstrap current within the island separatrix due to the rapid relaxation of pressure gradients via fast parallel electron heat transport along the closed helical magnetic field lines within the island. However, since the parallel pressure diffusivity is finite, the pressure does not completely equilibrate across the island separatrix. A minimum magnetic perturbation at the mode rational surface is then required to provide a sufficient flattening of the pressure profile about the island to destabilize the island. The threshold is demonstrated to depend on the magnitude of the magnetic perturbation as well as the plasma pressure β at modest levels of $\chi_{\|}/\chi_{\perp} = 10^5$, the ratio of the parallel and perpendicular heat diffusivities. However, numerical stability constraints on the magnitude of the timestep from the nonlinear parallel heat transport preclude raising this ratio to realistic values, or of following the mode to its nonlinear saturation

The next stage of exploration of the neoclassical MHD tearing mode is to consider the role poloidal mode coupling and toroidicity have in exciting modes beyond the neoclassical MHD threshold. The $m = 1/n = 1$ sawtooth oscillation may be particularly important for the destabilization of the mode. Simulations including both sawteeth oscillations and neoclassical tearing modes could provide additional insight into the observations of neoclassical tearing modes on TFTR and the discrepancy between the lack of a 2/1 neoclassical mode, but the presence of 4/3 or 3/2 neoclassical tearing modes—yet never more than one neoclassical mode simultaneosuly. Also, an enhancement to the numerical technique needs to be introduced which would allow for large values of $\chi_{\|}/\chi_{\perp}$, so that the nonlinear saturation of the mode can be identified. In conjunction with the destabilization threshold, the addition of a rotating field error should also be introduced to test the observed dependence of a critical β versus field error observations of DIII-D [18]. The present simulations are suggestive that such a threshold could be described by the neoclassical MHD model. Finally, the observation should be made that such a neoclassical MHD threshold could place strong limitations on the allowed field errors on ITER, which is designed for high β and hence large bootstrap currents in a high temperature plasma with a very large $\chi_{\|}/\chi_{\perp}$ ($> 10^{10}$).

Appendix A

Equilibria

This appendix is devoted to detailing the equilibria used in the numerical simulations. The numerical results are based on the ORNL (Oak Ridge National Lab) equilibria solver RSTEQ. Input to the solver includes plasma major (245 cm) and minor radius (80 cm), plasma β on axis, toroidal magnetic field strength (5 T), and pressure and q profiles as a function of the flux variable ψ_{eq}. The variable ψ_{eq} is related to the initial value code's coordinate ρ by

$$\frac{d\psi_{eq}}{d\rho} = -\frac{\rho I}{q}. \tag{A.1}$$

The first three subsections of this Appendix assume different equilibrium q profiles based on the parameter λ as detailed in Section 3.1, but share similar pressure profiles. The q value on axis is 1.01 and at the plasma edge is 5.0. The final subsection is an equilibrium designed to generate a large current gradient at the $q = 2$ surface.

A.1 Equilibrium A1

Parameters: $\lambda = 2.0$, $q_0 = 1.01$, $q_a = 5.0$, $p_r'' = -1.0$.

Solver Script	β	ϵ	Current (A)
run_eq8001.a	6.034E-04	3.281E-01	1.248E+06
run_eq8000.a	6.034E-03	3.283E-01	1.280E+06
run_eq8002.a	1.810E-02	3.287E-01	1.374E+06
run_eq8005.a	4.526E-02	3.291E-01	1.607E+06
run_eq8006.a	6.789E-02	3.293E-01	1.791E+06
run_eq8003.a	9.052E-02	3.294E-01	1.961E+06
run_eq8004.a	1.086E-01	3.296E-01	2.070E+06

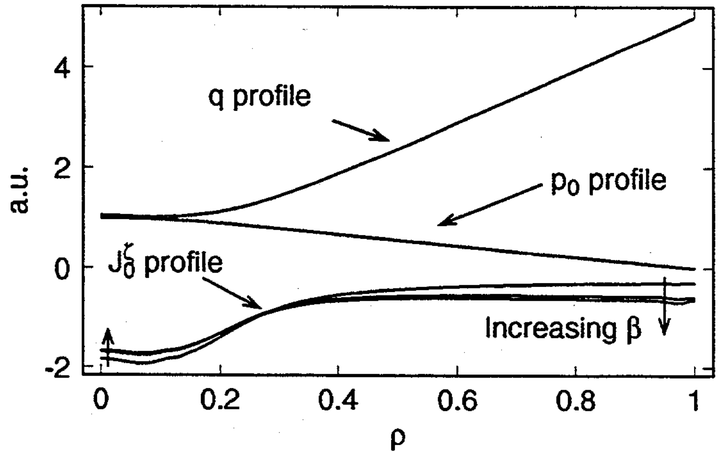

Figure A.1: Normalized pressure, q, and $J^{\zeta}_{m=0/n=0}$ profiles.

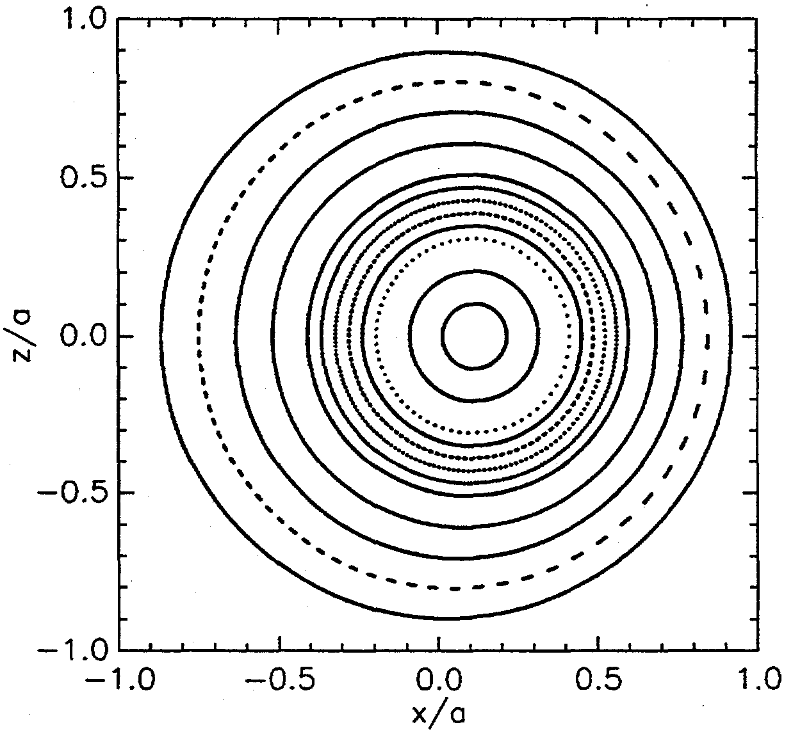

Figure A.2: Poincare plot for equilibrium run_eq8000.a

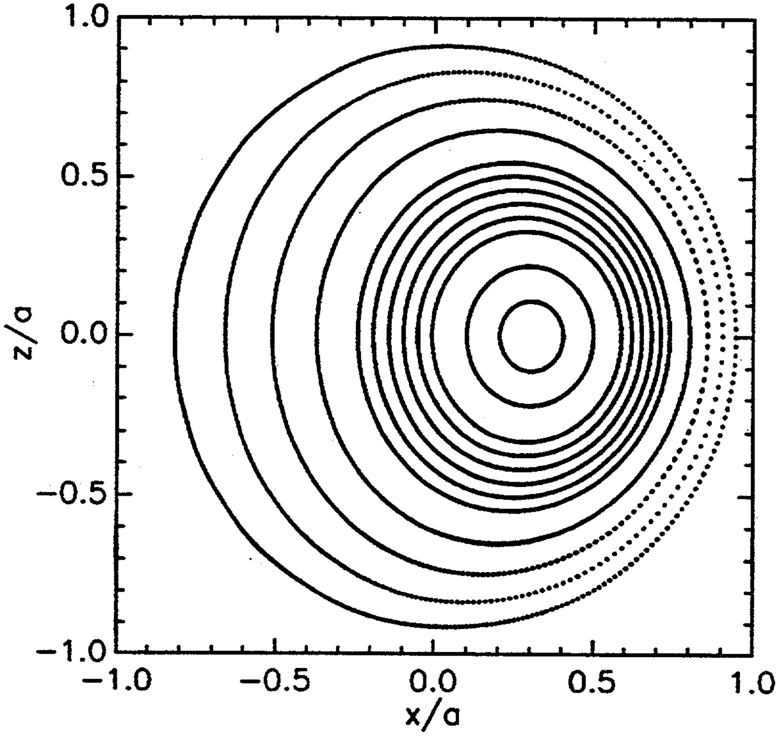

Figure A.3: Poincare plot for equilibrium run_eq8005.a

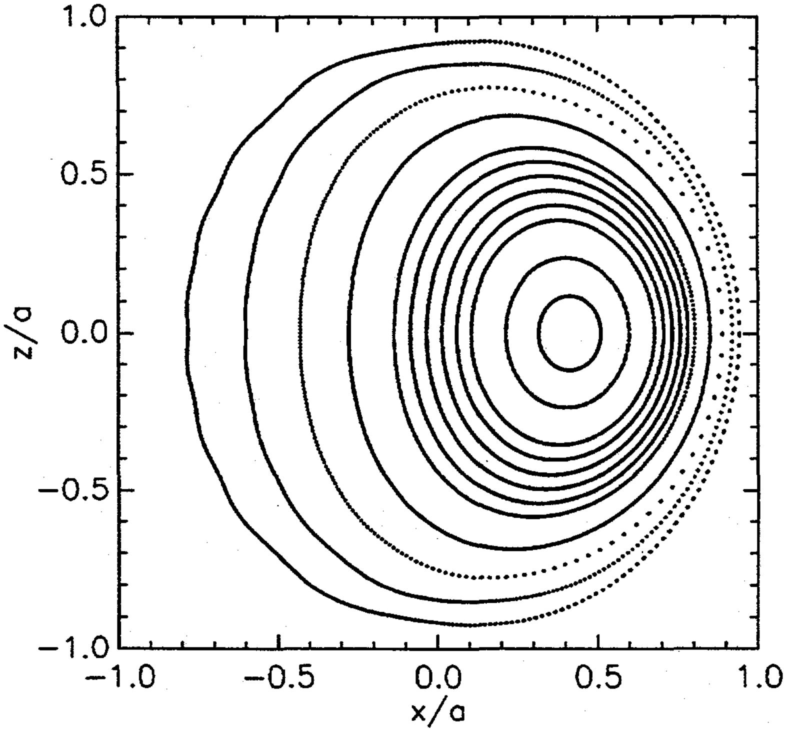

Figure A.4: Poincare plot for equilibrium run_eq8003.a

A.2 Equilibrium A2

Parameters: $\lambda = 1.0$, $q_0 = 1.01$, $q_a = 5$, $p_r'' = -1.0$.

Solver Script	β	ϵ	Current (A)
run_eq8101.a	6.034E-04	3.281E-01	1.243E+06
run_eq8100.a	6.034E-03	3.283E-01	1.276E+06
run_eq8102.a	1.810E-02	3.287E-01	1.376E+06
run_eq8103.a	9.052E-02	3.295E-01	1.994E+06
run_eq8104.a	1.086E-01	3.300E-01	2.037E+06

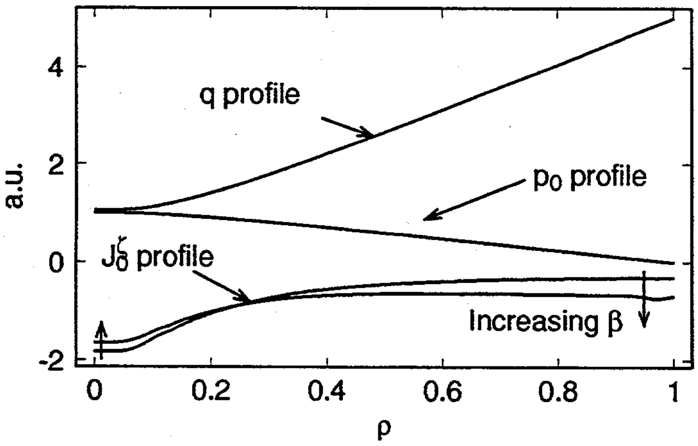

Figure A.5: Normalized pressure, q, and $J^{\zeta}_{m=0/n=0}$ profiles.

A.3 Equilibrium A3

Parameters: $\lambda = 3.0$, $q_0 = 1.01$, $q_a = 5$, $p_r'' = -1.0$.

Solver Script	β	ϵ	Current (A)
run_eq8301.a	6.034E-04	3.281E-01	1.249E+06
run_eq8300.a	6.034E-03	3.283E-01	1.280E+06
run_eq8302.a	1.810E-02	3.287E-01	1.373E+06
run_eq8303.a	9.052E-02	3.294E-01	1.949E+06
run_eq8304.a	1.086E-01	3.296E-01	2.057E+06

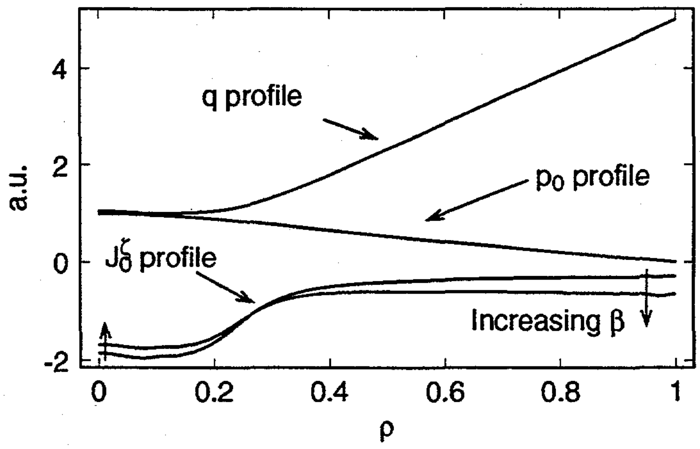

Figure A.6: Normalized pressure, q, and $J^{\zeta}_{m=0/n=0}$ profiles.

A.4 Equilibrium A4

Parameters: $a = 80cm$, $R_0 = 320cm$ $q_0 = 1.86$, $q_a = 5$, $p_r'' = -1.0$.

Solver Script	β	ϵ	Current (A)
run_req9506.b	1.029E-04	2.497E-01	8.790E+05
run_req9501.b	1.029E-03	2.497E-01	8.813E+05
run_req9505.b	4.118E-03	2.498E-01	8.906E+05
run_req9504.b	6.177E-03	2.499E-01	8.980E+05
run_req9502.b	8.235E-03	2.499E-01	9.061E+05
run_req9500.b	1.029E-02	2.500E-01	9.149E+05
run_req9503.b	2.059E-02	2.501E-01	9.639E+05

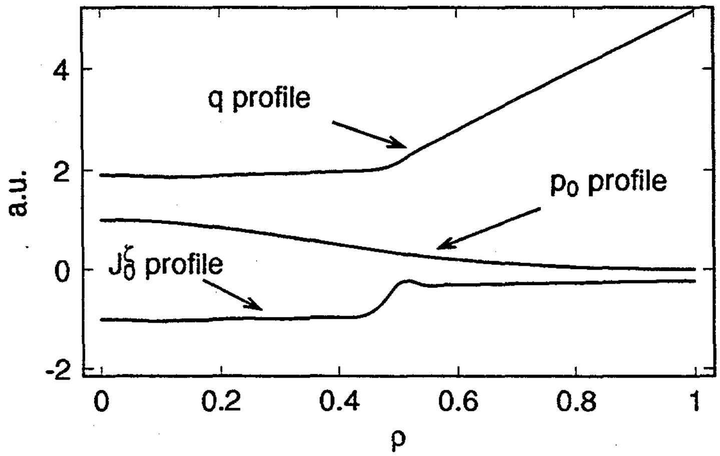

Figure A.7: Normalized pressure, q, and $J^{\zeta}_{m=0/n=0}$ profiles.

Bibliography

[1] Z. Chang et al., Nuclear Fusion **34** (1994) 1309.

[2] Z. Chang et al., Phys. Rev. Letters **74** (1995) 4663.

[3] E. Fredrickson, et al., "TAE Modes and MHD Activity in TFTR DT Plasmas" *in* Plasma Phys. & Cntl Nucl Fus Rsch 1994, (IAEA,Vienna,1994).

[4] B.A. Carreras, B.V. Waddell, H.R. Hicks, S.J. Lynch, Phys. Rev. A **18** (1978) 2732.

[5] Z. Chang, E.D. Fredrickson, J.D. Callen et al., PPPL-2941 (1993) 45.

[6] H.P. Furth, J. Killeen, M.N. Rosenbluth, Phys. of Fluids **6**, (1963) 459.

[7] J. Wesson, Tokamaks (Clarendon Press, Oxford, 1987).

[8] R. Fitzpatrick, Phys. Plasmas **2** (1995) 825.

[9] A.I. Smolyakov, A. Hirose, E. Lazzaro, G.B. Re, J.D. Callen, Phys. Plasmas **2** (1995) 1581.

[10] J.W. Connor, S.C. Cowley, R.J. Hastie, T.J. Martin, "The Influence of Toroidicity, Pressure, and Local Profile Changes on Tearing Mode Stability," *in* 1992 Int. Conf. on Plasma Phys. (ICOPP, Innsbruck,1992), Vol. 16C, p. II-1393.

[11] J.W. Connor, R.J. Hastie, J.B. Taylor, Phys. Fluids B **3** (1991) 1532.

[12] J.P. Friedberg, Ideal Magnetohydrodynamics (Plenum Press, New York, 1987), Sec. 9.6.

[13] A.H. Glasser, *submitted to* Phys. Plasmas (Feb 1995) .

[14] P. H. Rutherford, Phys. Fluids **16** (1973) 1903.

[15] R.B. White et al., Phys. Fluids **20** (1977) 800.

[16] W.X. Qu and J.D. Callen, "Nonlinear Growth of a Single Neoclassical MHD Tearing mode in a Tokamak", U.W. Plasma Report (1985) 85-5.

[17] R. Carrera, R.D. Hazeltine, M. Kotschenreuther, Phys. Fluids **29** (1986) 899.

[18] R.J. La Haye, A.W. Hyatt, J.T. Scoville, Nuclear Fusion **32** (1992) 2119.

[19] J.A. Holmes, J. Comput. Phys. **36**, (1980) 35.

[20] V.E. Lynch, B.A. Carreras, H.R. Hicks, J.A. Holmes, L. Garcia, Computer Physics Communications **24** (1981) 465.

[21] J.A. Holmes, B.A. Carreras, H.R. Hicks, V.E. Lynch, K.E. Rothe, Phys. Fluids **25**, (1982) 800.

[22] L.A. Charlton, J.A. Holmes, H.R. Hicks, V.E. Lynch, B.A. Carreras, J. of Comp. Physcis **63** (1986) 107.

[23] W.D. D'haeseller, W.N.G. Hitchon, J.D. Callen, J.L. Shohet, Flux Coordinates and Magnetic Field Structure, (Springer-Verlag, New York, 1991).

[24] H.R. Strauss, Nuclear Fusion **23** (1983) 649.

[25] R.D. Hazeltine and J.D. Meiss, Phys. Reports **121**, (1985) 1.

[26] J.D. Callen, W.X. Qu, K.D. Siebert, B.A. Carreras, K.C. Shaing, D.A. Spong, *in* Plasma Phys. & Cntl Nucl Fus Rsch 1986 (IAEA, Vienna,1987), Vol. I, p. 157.

[27] J.P. Wang, J.D. Callen, Phys. Plasmas 5 (1993) 3207.

[28] F.L. Hinton, R.D. Hazeltine, Rev. Mod. Phys. **48** (1976) 239.

[29] A.I. Smolyakov, A. Hirose, E. Lazzaro, G.B. Re, J.D. Callen, Phys. Plasmas **2** (1995) 1581.

[30] D.A. Spong, K.C. Shaing, B.A. Carreras, J.D. Callen, L. Garcia, "Transition from Resistive Ballooning to Neoclassical Magnetohydrodynamic Pressure-Gradient-Driven Instability," ORNL/TM-10947 (1988).

[31] A.H. Glasser, J.M. Greene, J.L. Johnson, Phys. Fluids **18** (1975) 875.

[32] M. Kotschenreuther, R.D. Hazeltine, P.J. Morrison, Phys. Fluids **28** (1985) 294.

[33] B.A. Carreras, L.A. Charlton et al., "Plasma Turbulence Calculations on Supercomputers," ORNL/P-90/0675 (1990).

[34] A.C. Hindmarsh, "Solution of block-tridiagonal systems of linear algebraic equations," UCID-30150, (1977) 1.

[35] G. Bateman, MHD Instabilities (MIT Press, Cambridge, MA, 1978), p. 190.

[36] B.A. Carreras et al., Nuclear Fusion **19**, (1979) 1423.

[37] J.W. Connor, R.J. Hastie, J.B. Taylor, Phys. Fluids B **3** (1991) 1532.

[38] Z. Chang, J.D. Callen, Nuclear Fusion **30** (1990) 219.

[39] C.C. Hegna, J.D. Callen, Phys. Fluids **4** (1992) 4072.

[40] S.E. Kruger personal communication on DCON runs (1995).

[41] C.C. Hegna, J.D. Callen, Phys. Plasmas **1**, (1994) 2308.

[42] H.P. Furth, P.H. Rutherford, H. Selberg, Phys. Fluids, **16** (1973) 1054.

[43] R.B. White, Handbook of Plasma Physics (North-Holland, Amsterdam, 1983), Sec. 3.5.

[44] J.W. Connor, R.J. Hastie, J.B. Taylor, Phys. Rev. **40** (1978) 396.

[45] R. Fitzpatrick, Nuclear Fusion **33** (1993) 1049.

[46] http://infopad.eecs.berkeley.edu/CIC/summary/
ftp://ftp.cdf.toronto.edu/pub/spectable.